# FIRST PRINCIPLES STUDY OF ENERGETICS OF ATOMIC DEFECTS AND STABILITY OF B1-TYPE OXIDES IN BCC FERROMAGNETIC IRON

By

**E. AKSHAYA DEVI**

(Enrolment No. PHYS 02 2015 04 019)

**Indira Gandhi Centre for Atomic Research, Kalpakkam, India**

*A thesis submitted to the*

*Board of Studies in Physical Sciences*

*In partial fulfillment of requirements*

*for the Degree of*

**DOCTOR OF PHILOSOPHY**

*of*

**HOMI BHABHA NATIONAL INSTITUTE**

**January, 2021**

# Homi Bhabha National Institute

## Recommendations of the Viva Voce Board

As members of the Viva Voce Board, we certify that we have read the dissertation prepared by E. AKSHAYA DEVI entitled:

" FIRST PRINCIPLES STUDY OF ENERGETICS OF ATOMIC DEFECTS AND STABILITY OF B1-TYPE OXIDES IN BCC FERROMAGNETIC IRON"

and recommend that it may be accepted as fulfilling the dissertation requirement for the Degree of Doctor of Philosophy.

Binaya Panigrahi

Date: 30/07/2021

**Chairman :** Dr. B. K. Panigrahi

CRavi

Date: 30/07/2021

**Guide/Convener :** Dr. C. Ravi

Subhradip Ghosh

Date: 30/07/2021

**External Examiner :** Dr. Subhradip Ghosh

T R Ravindran

Date: 30/7/2021

**Member 1 :** Dr. T. R. Ravindran

Date: 30/07/2021

**Member 2:** Dr. Arup Dasgupta

Final approval and acceptance of this dissertation is contingent upon the candidate's submission of the final copies of the dissertation to HBNI.

# Certificate

I hereby certify that I have read this dissertation prepared under my direction and recommend that it may be accepted as fulfilling the dissertation requirement.

Cravi

Date : 30 . 7 . 2021

Guide: Dr. C. Ravi

Place: Kalpakkam

# Statement by author

This dissertation has been submitted in partial fulfillment of requirements for an advanced degree at Homi Bhabha National Institute (HBNI) and is deposited in the Library to be made available to borrowers under rules of the HBNI.

Brief quotations from this dissertation are allowable without special permission, provided that accurate acknowledgement of source is made. Requests for permission for extended quotation from or reproduction of this manuscript in whole or in part may be granted by the competent authority of HBNI when in her judgement the proposed use of the material is in the interests of scholarship. In all other instances, however, permission must be obtained from the author.

Date: 30.7.2021

Place: Kalpakkam

Akshaya Devi.E

**E. Akshaya Devi**

# Declaration

I, hereby declare that the investigation presented in the thesis has been carried out by me. The work is original and has not been submitted earlier as a whole or in part for a degree/diploma at this or any other Institution/University.

E. Akshaya Devi

# List of publications

## Journals

1. Stability of B1-type oxides in BCC iron studied using density functional theory calculations, **E. Akshaya Devi**, C. Ravi, **Materials Today Communications 25 (2020) 101266.**
2. First-principles study of interaction energies of atomic defects in bcc ferromagnetic iron, **E. Akshaya Devi**, C. Ravi, and C. S. Sundar, **Phys. Rev. B 98 (2018) 144104.**

## Conferences/Symposiums/Articles

1. DFT study of the dissolution energy of embedded oxides and the bulk modulus of oxide embedded bcc iron, **E. Akshaya Devi**, C. Ravi, European Materials Research Society(EMRS), Fall-2019, Warsaw University of Technology, Warsaw, Poland.
2. First principles study of solute formation energies in bcc ferromagnetic iron, **E. Akshaya Devi,** C. Ravi, C.S. Sundar, Research Scholar Meet on Material Science and Engineering of Nuclear Materials (RSMMSENM)-2018, HBNI, IGCAR, Kalpakkam, India.

E. Akshaya Devi

*Dedicated to my beloved parents and all my teachers*

# Acknowledgments

First of all I would like to express my sincere gratitude for the support, inspiration and guidance from my doctoral advisor, Dr. C. Ravi. I would also like to thank my doctoral committee Dr. B. K. Panigrahi, Dr. T. R. Ravindran, Dr. Arup Dasgupta, for their support and guidance along the way.

I thank Dr. R. Rajaraman for helpful discussion during my research work. I would also like to thank Dr. C. S. Sundar for his valuable suggestions in the project on atomic defect's energetics in iron. I want to express my gratitude to Dr. A. K. Bhaduri and Dr. S.A.V. Satya Murty, present and past Director, IGCAR, for permitting me to pursue Ph.D. at IGCAR. I am highly thankful to Dr. Shaju K. Albert and Dr. G. Amarendra, present and past Group Director, MSG, Dr. M. Kamruddin, Associate Director, ANG, Dr. R. Govindaraj, Division Head, MPD, for providing a pleasant atmosphere for my smooth research. I acknowledge the Computing Systems Section of IGCAR for providing HPC cluster facility to carry out my research work. I thank Dr. Vidya Sundarajan, Dr. T. S. Lakshmi Narasimhan and Dr. M. Saibaba, present and past Dean SA, for the wonderful hospitality during my stay at JRF Enclave. I would like to thank Dr. R. Rajaraman, Dr. N. V. Chandra Shekar and Dr. B. V. R. Tata, present and past Dean physical sciences, HBNI, IGCAR for their support and being friendly during all the procedure throughout the tenure. I also thank Dr. S. Mathi Jaya as well as all MSG members.

I greatly acknowledge the financial assistance provided by Department of Atomic Energy, Govt. of India during my Ph.D. tenure. I would also like to acknowledge CSIR, Govt. of India and HBNI for providing me travel grant to attended an international conference.

I thank all my seniors, especially Dr. Kamali, Dr. Srinivasan, Dr. Nilakantha and Dr.

Vairavel. I also thank all my friends and 2015 batch mates, Rajitha R, Jakatha, Bala, Alok, Gopi, Dhilipan, Pragyna, Binay, Dilip, Rajitha K, Velraj, Darpan, Reshmi, Veena, Shirley, Shubhra, Shradha, Ijee, Surojith, Bijay, Twisha, Viji, Lavanya, Ramaswamy and Vikas. And also I thank all my juniors, Kashinath, Parvathy, Sruti (Jena & P.K.), Subashree, Kesavan, Deepitha, Abirami, Mohasin and Mrinalini.

I owe many thanks to my brother Dr. E. Dinesh Kumar, to whom I can always turn for advice, for all the wisdom he imparted upon me, and all the inspirations he provided.

Last but not least, I thank my parents Mr. S. Eswaran and Mrs. Meenakshi for their loving support, tireless encouragement and unfailing optimism.

**E. Akshaya Devi**

# Abstract

Body centred cubic (bcc) iron is the base material of Oxide Dispersion Strengthened (ODS) ferritic steels. ODS steels are considered as the primary candidate for structural application in future nuclear fission and fusion reactor. These modern steels are multicomponent alloys (with about 20 components: Fe, C, Mn, P, Si, Ni, Cr, Mo, V, Ti, Co, Cu, Al, B, W, Zr, N, O, Y) made up of Fe-Cr ferritic matrix in which a homogeneous dense distribution of small precipitate particles is created by ball milling and subsequent consolidation process involving either hot extrusion or hot isostatic pressing. These ODS steels have superior creep resistance and stability under irradiation attributed to the finest oxide particles densely dispersed in the ferritic matrix with high dislocation density.

Formation of precipitates is governed by diffusion kinetics of solute atoms in the solvent matrix. Formation and binding energies of atomic defects are important parameters controlling the diffusion of solute atoms hence nucleation, growth, and coarsening of precipitates. Due to this, several researchers have studied the interactions of solute elements with point defects in bcc iron employing first-principles computational methods based on the electronic Density Functional Theory (DFT). But these prior studies lack consistency among themselves in terms of specifications of the computational method, models of Fe with atomic defects, and the degree of structural relaxation included in the study.

In this thesis, a comprehensive and systematic calculation of the solute formation energies, solute-solute and vacancy-solute binding energies in bcc iron is reported for an extended set of 53 different solute elements, with atomic numbers 1 to 54, in bcc ferromagnetic iron using DFT total energy calculations. From the analysis of our calculated energetics of atomic defects, the following results have been obtained. (1) Formation energies of solutes from fourth and fifth periods vary with their atomic numbers such that they reach maxima near the ends of the periods and a minimum in between, with a local increase near Cu and Ag (like a quasiparabolic valley). Solutes from second and third periods show similar trend like the elements near the ends of the fourth and fifth periods. (2) The size factors of the solutes also show similar variation with their atomic numbers like their formation energies. These trends corroborate the relatively smaller formation energies and size factors of the common alloying additions to Fe (such as 3*d*, 4*d*, and *sp* elements) as compared to solutes that lack solubility (such as Li, Na, K, Rb, He, Ne, Ar, Kr, Xe, F, Cl, Br, I, Mg, Ca, Sr, Ag, Cd, In, Y). (3) The solubilities estimated from our formation energies are found to be in reasonable agreement with those from the phase diagram database. (4) Solute-solute and vacancy-solute binding energies are found to vary with the atomic number of the solutes in a manner inverse to solute formation energies and solute size factors, reaching strong binding energies near the ends of the periods which generally include the insoluble elements. (5) Another trend revealed by our work is that the size factors of isoelectronic sets of solutes increase down the groups with associated increase of formation energies, and strength of solute-solute and vacancy-solute binding energies. (6) A significant correlation is found between our vacancy-solute binding energies of 3d and 4d elements and the corresponding diffusion coefficients from literature whereby solutes with strong binding energies have higher diffusion coefficients and vice versa.

In addition to atomic defects, the stability of oxide particles embedded in the iron matrix have been studied. For the oxide nanoparticles in ODS steels, various compositions and structures have been discussed in the literature. These studies indicate that the B1-type TiO is also a potential dispersion for ODS steels. Despite this, no study has directly investigated the stability of B1-type oxides in bcc iron. In order to improve our understanding on the structure and stability of the B1-type oxides as dispersions, we carried out calculations of formation energies of 31 different oxides in bcc iron matrix using DFT total energy calculations. The stability of various NaCl B1-type oxides in bcc ferromagnetic iron were investigated in terms of their relaxed structure and formation energy. Several of the oxides, including MgO, AlO, ZrO and YO are found to remain structurally intact in the iron matrix as the initial $M_4O_4$ units. AuO and HeO are unstable. SiO tends to relax to respective Si-O pairs. Relaxed bond lengths show that the Fe matrix is expanded around the embedded oxide clusters. Formation energies of the oxides show a correlation with the equilibrium volumes of the oxide embedded iron. Bulk moduli of the oxide embedded iron show an inverse correlation with their equilibrium volumes. Further, formation energies of the oxides show an inverse correlation with the bulk moduli of the oxide embedded iron systems. This work predicts that the oxides, namely SnO, MgO, ScO, ZrO, AlO, MnO, TaO, ZnO, YO and CdO are stable in the iron matrix without degrading its bulk modulus significantly. Iron matrix with such oxides are expected to resist dislocation motion and thermal expansion. Most of the MO oxides derive their mechanism for the endothermic or exothermic formation energies from the degree of overlap between *d* density of states of M and Fe atoms. That is, the M's with exothermic formation energy for MO, such as NiO and RhO, exhibit strong overlap of their *d* density of states with the Fe *d* density of states while the M's with endothermic formation energy for MO, such as YO and ZrO, exhibit weak overlap with the Fe density of states.

# Contents

# List of figures

# List of tables

# 1

# Introduction

Solids are known for their resistance to external stress compared to liquid and gaseous phases. This high resistance to deformation is due to the uniform atomic structure and the strong interaction between the atoms in the solids. However, each solid type has its definite threshold of resistance; any small increase beyond threshold can lead either to their destruction or change of phase, i.e., to liquid or gas. For instance, when a piece of iron is subjected to mechanical load, it may break apart or crushed into segments; but when exposed to very high temperatures, it starts to melt. Thus, the knowledge of the temperature threshold of materials enables to identify their use in the day-to-day life. The critical question here is why some materials can withstand very high temperature while others cannot. The answer lies in their composition, structure and bonding strength. Material science research aims to discover new materials with desired properties through a thorough understanding of the interrelations among their composition, structure and chemical bonding.

Globally, coal and natural gas are the primary sources of electrical energy. These non-renewable energy sources emit carbon dioxide to the atmosphere, which results in climate change. However, renewable energy sources such as solar and wind are not commercially feasible due to the restrictions on land availability and other environmental conditions. To meet the energy demand without causing damage to environment, nuclear power reactors are the promising alternative. The search for high-temperature materials is of paramount importance to construct safe and efficient nuclear reactors.

## 1.1 Structural materials characteristics in high-temperature environments

Typical high temperature materials are stainless steel, refractory metals, superalloys and ceramics. At high temperature, materials lose their strength and also undergo oxidation and corrosion. High temperature applications requires these materials to be strong and resist oxidation and corrosion. In addition to these features, in the nuclear environment, the materials should possess strong mechanical properties against irradiation. The maximum operating temperature of high temperature materials used in the nuclear industry and its effective neutron cross section are listed in Table 1.1.

**Table 1.1:** *Structural materials with operating temperature and effective neutron cross section[1].*

| Material | Operating temperature (°C) | Effective neutron absorption cross section with respective to Zr alloys |
|---|---|---|
| Zirconium alloy | 400 | 1 |
| FM stainless steels | 500 | 15 |
| Austenitic stainless steels | 600 | 15 |
| ODS alloys | 700 | 15 |
| Nb-1Zr alloy | 800 | 20 |
| ZrC | 900 | 0.20 |
| SiC | 900 | 0.10 |

- **Zirconium alloy**

  Zirconium and its alloys are being used as fuel cladding in the nuclear reactor for its high melting point, low absorption cross-section for thermal neutrons, excellent corrosion resistance in water, and good mechanical characteristics at operating temperatures of nuclear reactors. But its mechanical properties and the corrosion resistance are not satisfactory at very high temperatures[1,2]. These alloys react with cooling water and forms zirconium dioxide ($ZrO_2$) along with the release of hydrogen gas. This reaction gets out of control during nuclear accidents with explosive hydrogen gas release[3]. Thus, it is needed to develop new Zr alloys with improved corrosion resistance at an operating temperature above the conventional Zr alloy, i.e., 400 °C, along with high creep and radiation resistance[2,4,5].

- **Stainless steel**

  Austenitic stainless steels exhibit good creep and corrosion/oxidation resistance; thus, it is being used as cladding materials. But the operating temperature of austenitic stainless steel is up to 600 °C[1]. Though it shows good creep resistance, its resistance towards void swelling is poor. In addition to void swelling, other radiation damages such as creep on irradiation, He embrittlement and microstructural instability also occurs even at a moderate neutron irradiation dose in austenitic steel[1,6–8]. Researchers have taken steps to prevent void swelling by means of the introduction of precipitation of dispersed phases, cold deformation, and alloying with trace elements. But the challenges remain unfulfilled[8–12]. In contrast to the features of austenitic steel, the characteristics of ferritic steel are low thermal expansion and high thermal conductivity, better void swelling and helium embrittlement resistance. This excellent feature of ferritic steels is due to its BCC/BCT crystal structure and its tempered martensitic microstructure, along with the presence of high density of irradiation-defect sink[1, 8]. However, the microstructure instability of ferritic steel occurs at high temperature and irradiation affect both the mechanical and corrosion properties. Therefore, both types of steel do not suit the fast reactors. One approach to develop new ferritic steel is the introduction of the highly stable oxide particles into the matrix, called Oxide Dispersion Strengthened (ODS) steel[1, 13].

- **Oxide Dispersion Strengthened steel**

  Oxide Dispersion Strengthened (ODS) steels are multicomponent alloys with 20 different components such as Fe, C, Mn, P, Si, Ni, Cr, Mo, V, Ti, Co, Cu, Al, B, W, Zr, N, O, and Y. This steel is made of Fe-Cr ferrite matrix with uniform distribution of highly stable dense oxide nanoparticles[ONP] of titania ($Ti_2O_3$) and yttria ($Y_2O_3$). In ODS materials, rare earth oxide such as yttria ($Y_2O_3$) was introduced because of its high melting point and its low solubility in steels. As the oxygen solubility in ferrite is very low, various types of oxides can form in the presence of other solute elements. In steels, the oxides can be composed of aluminium, yttrium, titanium, lanthanum, cerium, chromium and so on. Thus, the microstructure becomes complex with various oxides of different composition and size. These ONPs obstruct the dislocation motion and sliding of the grain boundary. Thus, it leads to the stability of microstructure at high temperatures[9, 14–21]. ONP acts as sinks to radiation induced defects, provides good radiation damage resistance[8, 9, 22, 23]. ODS steels shows good mechanical properties up to the temperature of 800 °C. The development of ODS steel is carried out by a mechanical alloying, which is accomplished by ball milling followed by consolidation processes such as hot extrusion or hot isostatic pressing. Figure 1.1 depicts various process involved in the production of ODS steel. In Sodium cooled Fast Reactor (SFR), it is known that there is no effect on the corrosion and mechanical properties by liquid Na up to 700 °C. Thus, ODS steel is best to suit for SFR[1, 24].

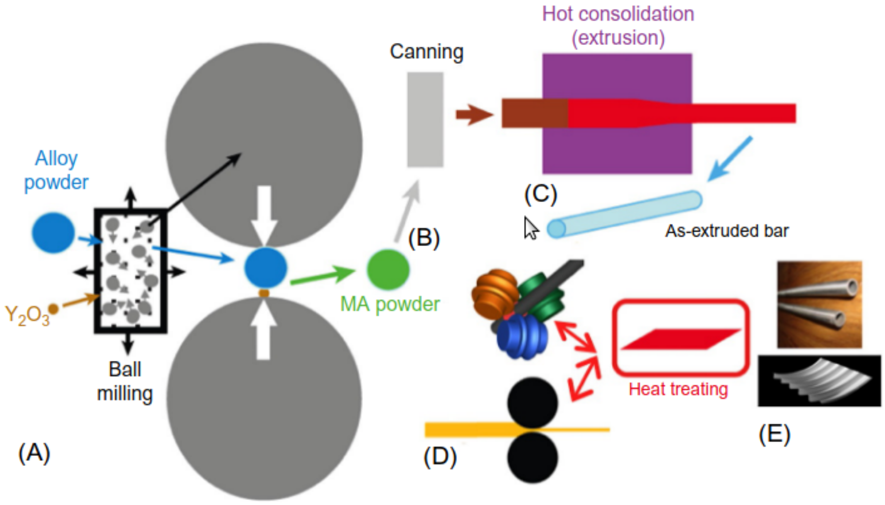

**Figure 1.1:** *Production of ODS steel: (A) ball milling; (B) Mechanical Alloying and canning powders; (C) consolidation (hot extrusion); (D) hot rolling; and (E) fabricate to tube and plate form[13].*

- **Refractory alloys**

  The melting point of these alloys is above 1850 °C, but the neutron absorption cross section of most of them are very high. So they can not be used as fuel cladding. Although refractory metals possess good creep and oxidation resistance, they show average radiation resistance, high cost and fabrication problems. Niobium alloy shows the advantage of fabrication, high ductility and melting temperature and low ductile to brittle transformation temperature and neutron absorption cross-section. But their strength is very low and its oxidation resistance is poor. So it requires special care during its fabrication[1].

- **Ceramic materials**

  After the Fukushima-Daiichi nuclear reactor accident, ceramics are investigated as an alternative to Zr alloy. These materials can withstand an accident that occurred during a natural disaster in the reactor. SiC is considered as a potential cladding material for Lead cooled Fast Reactor (LFR), has good high-temperature corrosion resistance, good high-temperature strength and low effective neutron cross-section[1]. The issues with SiC are brittle behaviour, undergoes oxidation and stress corrosion cracking.

## 1.2 Point defects in materials

No metal exist in perfect order and purity; some foreign atoms are always present in it. The elements which ruin the metal's property are termed as impurities while the elements added intentionally to enhance the properties are known as alloying elements. These foreign atoms, existing in the metal matrix as either interstitial or substitutional elements, results in the formation of a solid solution[25]. The addition of foreign atoms to metals will improve its mechanical strength and corrosion resistance. It also plays an essential role in the nucleation, evolution, and kinetics of larger defects, which controls the deformations and failure in the metals[26]. Generally, it increases the strength of metals and decreases the ductility by hindering the dislocation motion. In addition to this, an understanding of atomic defects is vital to characterize/suppress radiation damage. The effect of the addition of alloying elements in iron, which is the base of structural steels, on its mechanical properties is listed in Table 1.2.

**Table 1.2:** *Effect of addition of alloying elements in iron*

| Element | Effect |
|---|---|
| Aluminum | Deoxidizes and restrict grain growth[27] |
| Boron | Increases hardenability[27–29] |
| Carbon | Increases hardenability[29] and strength[27] |
| Chromium | Increases corrosion resistance, hardenability and wear resistance[27] |
| Lead | Increases machinability[30] |
| Manganese | Increases hardenability[31] and counteracts brittleness from sulfur |
| Molybdenum | Deepens hardening[27,29], raises creep strength[32] and hot-hardness, enhances corrosion resistance[27] and increases wear resistance[33] |
| Nickel | Increases strength and toughness[27] |
| Phosphorous | Increases strength, machinability, and corrosion resistance[27] |
| Silicon | Deoxidizes[27], helps electrical and magnetic properties, improves hardness and oxidation resistance |
| Sulfur | Increases machinability[27], but damages hot forming characteristics |
| Titanium | Forms carbides[27], reduces hardness in stainless steel |
| Tungsten | Increases wear resistance[34] and hot strength and hot-hardness[27] |
| Vanadium | Increases hardenability[27] |

The formation of atomic defects in metals is generally an endothermic process. These atomic defects are produced by growth and synthesis, thermal and thermochemical treatments, plastic deformation, ion implantation and irradiation. Electron paramagnetic resonance provides information about impurity concentrations, lattice environment of impurity, and chemical identity. But this technique requires best practitioners. Other techniques such as photoluminescence and Hall measurements, gives information on how the optical and electric properties affected by the atomic defect, but it fails to provide the nature of defects. For these reasons, the first principles calculations serve as the best option to determine the atomic and electronic structure of point defects with more accuracy.

## 1.3 Modelling of point defects

Vacancies are important defects in the metal. In 1953, Pochapsky measured a vacancy formation energy of 1.17 eV in Aluminum using heat capacity and residual resistivity technique while, in 1975, Triftshäuser found 0.66 eV using positron annihilation experiment[35, 36]. The difference between these values leads to a difference in the equilibrium vacancy concentration by a factor of 1000. Thus, the calculation of this value employing theoretical methods is an essential alternative. The theoretical methods used for the calculation of point defect property are as follows:

- Elastic methods[37–39]
- Calculation using empirical interatomic potential[40–42]
- Density Functional Theory (DFT)[43–45]

Among these methods, DFT gives more accurate data. Using the DFT technique, the formation energy of vacancy in the transition elements have been calculated[46, 47]. Figure 1.2 shows the vacancy formation energies of 5d (lower panel), 4d (central panel), 3d (upper panel) transition metals as a function of atomic number (Z). It is observed that the vacancy formation energy of all the transition elements lies between 1 to 3 eV, and also they follow parabolic trend across each transition element row in the periodic table. Grimvall pointed out the interesting fact that the ratio of melting point to vacancy formation energy is from 8 to 13 for most of the metals[49].

The data of interaction of atomic defects with the solute, which influence the microstructure of materials and its evolution, can also be accurately obtained from first principles calculation[50]. These data are then introduced to higher scale models to predict the diffusion properties. The calculation of solute-vacancy binding energies in Fe, Zr, W, Mg, Al, Ti, Co and Ni had been carried out using density functional theory[50–61].

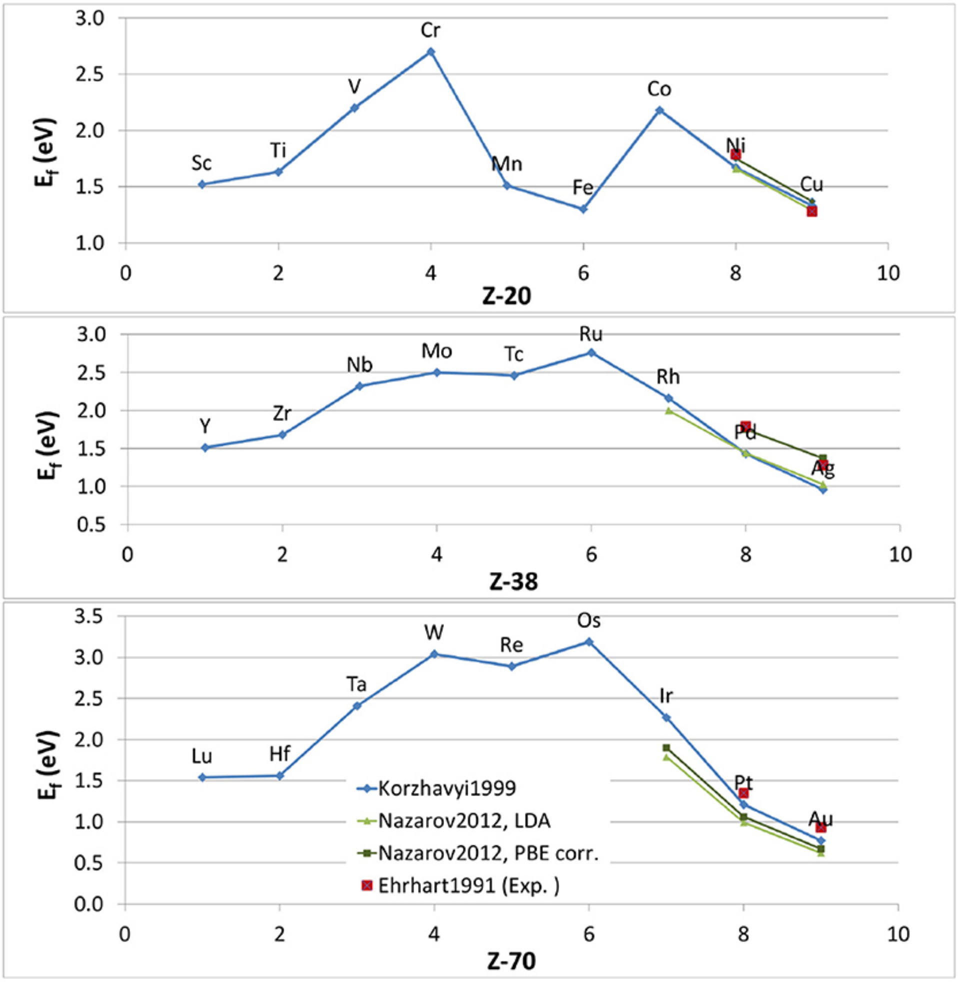

**Figure 1.2:** *Vacancy formation energy as a function of atomic number (Z)[48]*

.

## 1.4 Motivation

The interaction of solute atom with point defect is responsible for the diffusion of solute in the solvent matrix, which in turn responsible for microstructure evolution and modification in the mechanical properties of the material. The experimental data for the point defect - solute interactions are challenging to measure and also scarce. First principles electronic structure calculations help to obtain these data. Body centered cubic (bcc) iron is the base material for all types of ferritic steels, which are widely used in energy industry. But systematic study of energetics of point defects in bcc iron is absent in the literature. One of the motivations for this thesis is therefore to provide a systematic study using first principles calculations. For this, the formation energies, vacancy-solute and solute-solute binding energies in bcc Fe have been computed for an extended set of 54 solute elements with atomic numbers 1 to 54. These results are analyzed to elucidate their trends.

Dispersion strengthening is an effective way to increase the strength of the material at high temperature by introducing fine and uniform distribution of dispersoid particle, which are insoluble in the matrix. Oxide Dispersion Strengthened (ODS) steel is one such alloy prepared through dispersion of stable oxides. But for the choice of the oxide particles, no guidelines have been established through systematic studies. Several oxide candidates, including B1 type TiO, have been observed by the researchers. Our motivation here is to investigate the stability of B1 (NaCl) type oxides with the aim of identifying stable oxides to obtain improved ODS steel. For this, we have investigated the structure and stability of 31 different B1-type oxide dispersion in bcc ferromagnetic iron in terms of their relaxed structure and formation energy obtained from density functional theory calculations.

## 1.5 Thesis outline

The contents of the thesis are organized as follows:

- **Chapter 2** describes the theoretical methods used for the electronic band structure calculations such as Hartree-Fock and Density Functional Theory (DFT). Some important practical issues for the application of DFT, namely, k-point sampling, energy cutoff and pseudopotential approximation are discussed.

- **Chapter 3** presents the results of point defect properties such as the formation energy, concentration of solute at thermal equilibrium and the size factor for an extended set of 53 different solute elements with atomic numbers from 1 to 54 in bcc ferromagnetic iron. The analysis of how the solute formation energies and solute size factors are correlated is also presented.

- **Chapter 4** presents the results of vacancy-solute and solute-solute binding energies as these variables gives information on the mechanism in which the solute moves in the solvent matrix and forms the precipitate. The trends of these variables across the periodic table and the correlation among them are analysed.

- **Chapter 5** focuses on DFT study on the stability of B1-type oxides in bcc ferromagnetic iron. Analysis of stability of oxides was performed based on the equilibrium structure and formation energy of the embedded oxides. The results of bulk modulus of the oxide embedded bcc iron and their correlation with the formation energy, and the mechanism behind the exothermic and endothermic formation energies through the density of states analysis has been discussed.
- **Chapter 6** summarizes the salient results of the present study and the scope for future work.

# 2

# Theoretical background

## 2.1 Introduction

This chapter describes the theory behind the first principles or ab-initio method of electronic structure calculations. The term "first principles" refers to obtaining the electronic properties of the system with the atomic number as the input. We begin with the approximation made to bring down from many electrons-nuclei problems to a many electron problem. And then, we discuss the two different approaches of many electron problem namely Hartree-Fock and Density Functional Theory (DFT). As the Plane Wave (PW) DFT is more suitable for the supercell study of point defects in solids, we discuss some practical issues that needs to be taken care when using PW-DFT.

## 2.2 Quantum mechanics of many body system

### 2.2.1 Many body Schrödinger equation

The Schrödinger equation $H\psi = E\psi$ is the basis for quantum mechanics which is used to study about the electronic structure of a material. Here, H is the Hamiltonian operator, E is the energy eigenvalue, and $\psi$ is the wave function. The Schrödinger equation describes the energy of the electron and nuclei in a material. The Hamiltonian for a system containing M nuclei and N electrons can be written as

$$\widehat{H}_{tot} = -\frac{1}{2}\sum_{i=1}^{N}\nabla_i^2 - \frac{1}{2}\sum_{I=1}^{M}\frac{1}{M_I}\nabla_I^2 - \sum_{i=1}^{N}\sum_{I=1}^{M}\frac{Z_I}{\mathbf{r}_{iI}} + \sum_{i=1}^{N}\sum_{j>i}^{N}\frac{1}{\mathbf{r}_{ij}} + \sum_{I=1}^{M}\sum_{J>I}^{M}\frac{Z_I Z_J}{\mathbf{R}_{IJ}} \quad (in\ a.u) \tag{2.1}$$

where the index I and J runs over the M nuclei while the index i and j runs over the N electrons in the system. The first term corresponds to the kinetic energy of the electrons and the second term corresponds to the kinetic energy of nuclei. The other three terms, in order, represent the attractive electrostatic interaction between the nuclei and the electrons, repulsive potential due to the electron-electron interaction and repulsive potential between nuclei, respectively.

The ground state of a given system is obtained by solving the time independent many body Schrödinger equation,

$$\widehat{H}_{tot}\Psi(\mathbf{R}_I, \mathbf{r}_i) = E\Psi(\mathbf{R}_I, \mathbf{r}_i) \tag{2.2}$$

Here, $\Psi$ is the total wave function of the system which depends on all the coordinates of nucleus, R and electron, r . Solving Eq. 2.2 gives the ground state energy $E_0$ and the ground state wave function $\psi_0$. In practice, it is impossible to solve Eq. 2.2. The analytical solutions are available only for one electron systems, like hydrogen atom and $H_2^+$ molecules while exact numerical solutions are limited to atoms and small molecules. This difficulty arises due to the fact that the wave function is a function of $3(M+N)$ degrees of freedom.

### 2.2.2 Born-Oppenheimer approximation

The many body Schrödinger Eq. 2.2 can be solved by decoupling the electronic and nuclear degrees of freedom. This separation of electronic and nuclear coordinates is called Born-Oppenheimer (BO) approximation. The BO approximation is based on the fact that the nuclei are much heavier than the electrons and that one can assume that electrons instantaneously change its position with respect to change in nuclei's position. Thus, the electronic Hamiltonian is given by

$$\widehat{H}_{elec} = -\frac{1}{2}\sum_{i=1}^{N}\nabla_i^2 - \sum_{i=1}^{N}\sum_{I=1}^{M}\frac{Z_I}{\mathbf{r}_{iI}} + \sum_{i=1}^{N}\sum_{j>i}^{N}\frac{1}{\mathbf{r}_{ij}} \quad (in\ a.u) \tag{2.3}$$

The solution of the Schrödinger equation with $\widehat{H}_{elec}$ is the electronic wave function $\psi_{elec}$ with the electronic energy $E_{elec}$. The total energy $E_{tot}$ is the sum of $E_{elec}$ and the constant nuclear repulsion term $E_{nuc}$.

$$\widehat{H}_{elec}\psi_{elec} = E_{elec}\psi_{elec} \tag{2.4}$$

To solve this equation using the discretisation technique, it requires a vast number of grid points. As the grid points increase, the computation time and memory requirement will also increase. But the variational method helps to solve the Schrödinger equation in a very effective way[62]. The variational technique is used in all quantum mechanical approaches including Hartree-Fock and Density Functional Theory for solving the Schrödinger equation to get the one-electron wave function[63].

### 2.2.3 Variational method

The expectation value of the energy for stationary state $\psi$ is given by

$$E[\psi] = \frac{\left\langle \psi|\widehat{H}|\psi \right\rangle}{\langle \psi|\psi \rangle} \tag{2.5}$$

where

$$\left\langle \psi|\widehat{H}|\psi \right\rangle = \int \psi^* \, \widehat{H} \, \psi \, d\mathbf{x}$$

The variational principle states that the energy computed from a guessed $\psi$ is an upper bound to the true ground-state energy $E_0$, i.e.,

$$E_\psi \geq E_0 \tag{2.6}$$

Full minimization of the functional $E[\psi]$ with respect to all allowed N-electrons wave function will give the true ground state $\psi_0$ and energy $E[\psi_0] = E_0$; that is

$$E_0 = min_{\psi \to N} E[\psi] = min_{\psi \to N} \left\langle \psi|\widehat{T} + \widehat{V}_{Ne} + \widehat{V}_{ee}|\psi \right\rangle \tag{2.7}$$

For a system with N electrons and given nuclear potential $V_{ext}$, the variational principle defines a procedure to determine the ground state wave function $\psi_0$, the ground-state energy $E_0[N, V_{ext}]$, and other properties of interest.

In the following sections we will discuss the two different approaches to the many electron problem: The Hartree-Fock theory and Density Functional Theory. These two theories are the modified and simplified versions of the full problem of many electrons moving in a potential field.

## 2.3 Hartree-Fock theory

In the Hartree-Fock (HF) theory, the interaction of each electron with all the others is approximated as the interaction with the mean electronic field due to all other electrons. Therefore, this theory is termed as mean field theory. This approximation can be obtained by assuming the many electron wave function in a Slater determinant form of orbital function $\psi$,

$$\Psi(\mathbf{r}_1, \mathbf{r}_2, ..., \mathbf{r}_n) = \frac{1}{\sqrt{N!}} \begin{vmatrix} \psi_1(\mathbf{r}_1) & \psi_2(\mathbf{r}_1) & \cdots & \psi_N(\mathbf{r}_1) \\ \psi_1(\mathbf{r}_2) & \psi_2(\mathbf{r}_2) & \cdots & \psi_N(\mathbf{r}_2) \\ \vdots & \vdots & & \vdots \\ \psi_1(\mathbf{r}_N) & \psi_2(\mathbf{r}_N) & \cdots & \psi_N(\mathbf{r}_N) \end{vmatrix} \tag{2.8}$$

The Slater determinant form ensures that the electron wave function is antisymmetric. On substituting Eq. 2.8 and Eq. 2.3 into Eq. 2.4, we will obtain the following HF eigenvalue equation for each orbital $\psi_i$:

$$\left[-\frac{\nabla^2}{2} + \sum_{I=1}^{M} \frac{Z_I}{r_{iI}} + \frac{1}{2}\sum_{j}^{N} \int d\mathbf{r}' \frac{|\psi_i(\mathbf{r}')|^2}{|\mathbf{r}-\mathbf{r}'|}\right] \psi_i(\mathbf{r}) - \frac{1}{2}\sum_{j}^{N} \int d\mathbf{r}' \frac{\psi_j(\mathbf{r})\psi_j^*(\mathbf{r}')\psi_i(\mathbf{r}')}{|\mathbf{r}-\mathbf{r}'|} = \epsilon_i \psi_i(\mathbf{r}) \tag{2.9}$$

Applying the variational principle and setting the constraint to the set of eigenvalue equation, $\Psi$ can be solved through self consistent approach. That is, we will start with initial guess for the set of orbitals $\psi_i$ and solve HF equation, then construct the wave function $\Psi$ from the new set $\psi_{i_{new}}$ and solve HF equation again to get $\Psi$. Finally, determine the $\delta E$ which is the energy difference between the new and previous value.

If the $\delta E$ is more than the prescribed value, then the process will continue. Each cycle through this process is called self consistent field loop.

This method include the exchange interaction term of the potential via antisymmetric wave function, thus, it lowers total binding energy of atom due to the separation of the parallel spin electrons. However, it neglects the correlations in the motion between two electrons with anti-parallel spins.

## 2.4 Density Functional Theory

### 2.4.1 Thomas-Fermi-Dirac approximation

In 1927, Thomas[64] and Fermi[65] proposed the model for the electronic structure calculation. In this model, electron density $n(\mathbf{r})$ is used as the basic variable instead of the wave function and it gives the idea of how the density functional theory works. The kinetic energy of the system of electrons is approximated as a functional of electron density and exchange and correlation terms are ignored. The total energy of the system in an external potential is written as a functional of the electron density n(r) as:

$$E_{TF}[n(\mathbf{r})] = A_1 \int n(\mathbf{r})^{5/3} d\mathbf{r} + \int n(\mathbf{r}) V_{ext}(\mathbf{r}) d\mathbf{r} + \frac{1}{2} \iint \frac{n(\mathbf{r}) n(\mathbf{r}^{'})}{|\mathbf{r} - \mathbf{r}'|} d\mathbf{r} d\mathbf{r}' \tag{2.10}$$

The first term is the kinetic energy of the non-interacting electrons in a homogeneous electron gas which is obtained by adding all the free electron energy state $\epsilon = k^2/2$ up to the Fermi vector $k_F$ with $A_1 = \frac{3}{10}(3\pi^2)^{(2/3)}$ and it is given as:

$$t_0[n(\mathbf{r})] = \frac{2}{(2\pi)^3} \int_0^{k_F} \frac{k^2}{2} 4\pi k^2 dk \tag{2.11}$$

The second term corresponds to classical electrostatic energy of the nucleus-electron Coulomb interaction and the third term is the classical repulsive energy between the electrons. In 1930, Thomas-Fermi model was extended by including exchange term, thus it becomes Thomas-Fermi-Dirac (TFD) model. Now, the $E_{TF}$ is written as:

$$E_{TFD}[n(\mathbf{r})] = A_1 \int n(\mathbf{r})^{5/3} dr + \int n(\mathbf{r}) V_{ext}(\mathbf{r}) d\mathbf{r} + \frac{1}{2} \iint \frac{n(\mathbf{r}) n(\mathbf{r}')}{|\mathbf{r}-\mathbf{r}'|} d\mathbf{r} d\mathbf{r}' + A_2 \int n(\mathbf{r})^{(4/3)} d\mathbf{r} \tag{2.12}$$

where the value of $A_2$ is $-\frac{3}{4}(3/\pi)^{(1/3)}$. The ground state density and energy can be obtained by minimizing $E_{TFD}[n(\mathbf{r})]$ for all electron density $n(\mathbf{r})$ which is subject to the constraint on the total number of electrons

$$\int d^3\mathbf{r}\, n(\mathbf{r}) = N \tag{2.13}$$

By using the Lagrange multiplier's method, the solution can be found in the stationary condition:

$$\delta\{E_{TFD}[n(\mathbf{r})] - \mu(\int n(\mathbf{r}) d\mathbf{r} - N)\} = 0 \tag{2.14}$$

where the Lagrange parameter, $\mu$ is the chemical potential. After the minimization, we obtain the Thomas-Fermi-Dirac equation as:

$$\frac{5}{3} A_1 n(\mathbf{r})^{(2/3)} + V_{ext}(\mathbf{r}) + \int \frac{n(\mathbf{r}')}{|\mathbf{r}-\mathbf{r}'|} d\mathbf{r}' + \frac{4}{3} A_2 n(\mathbf{r})^{(1/3)} - \mu = 0 \tag{2.15}$$

On solving this equation, we will get the ground state density and energy. This TFD model gives many problems as the approximation made for the kinetic energy term is not accurate enough. The major problem is that the theory fails to incorporate the bonding between the atoms, so the formation of molecules and solids are not possible in this theory[66]. This model does not describe the electrons in the system but the idea of using electron density as the fundamental variable demonstrate the manner in which DFT works.

### 2.4.2 Hohenberg-Kohn theorem

Density Functional Theory is based on two theorems first proved by Hohenberg and Kohn[67].

The first theorem is as follows:

- *For any system of interacting particles in an external potential* $V_{\text{ext}}(\boldsymbol{r})$*, the potential* $V_{\text{ext}}(\boldsymbol{r})$ *is determined uniquely, except for a constant, by the ground state charge density* $n(\boldsymbol{r})$*.*

The second theorem is given as:

- *A universal functional for the energy* $F[n(\boldsymbol{r})]$ *in terms of the density* $n(\boldsymbol{r})$ *can be defined, valid for any external potential* $V_{\text{ext}}(\boldsymbol{r})$*. For any particular* $V_{\text{ext}}$*, the exact ground state energy of the system is the global minimum value of this functional, and the density* $n(\boldsymbol{r})$ *that minimizes the functional is the exact ground state density.*

### 2.4.3 Kohn-Sham equation

The Kohn-Sham (KS) equation uses the Hohenberg-Kohn theorems and make the DFT calculation possible. The Kohn-Sham equation maps the many body interacting system to a fictitious non-interacting system with an effective single-particle potential $V_{KS}(\mathbf{r})$. The Hamiltonian for the independent particle system is

$$\widehat{H}_{KS} = -\frac{1}{2}\nabla^2 + V_{KS}(\mathbf{r}) \tag{2.16}$$

For a system of N independent electrons, the ground state is obtained by solving the N-one electron Schrödinger equation

$$\left[-\frac{1}{2}\nabla^2 + V_{KS}(\mathbf{r})\right]\psi_i(\mathbf{r}) = \epsilon_i\psi_i(\mathbf{r}) \tag{2.17}$$

Then, the density of non-interacting system is constructed from the following equation:

$$n(\mathbf{r}) = \sum_{i=1}^{N}|\psi_i(\mathbf{r})|^2 \tag{2.18}$$

which is subjected to the constraint of total number of electrons

$$\int n(\mathbf{r})d\mathbf{r} = N \tag{2.19}$$

The universal functional $F[n(\mathbf{r})]$ is the sum of kinetic energy of the non-interacting independent particle $T_s$, classical electrostatic energy (Hartree) of the electrons $E_H[n(\mathbf{r})]$ and exchange and correlation energy $E_{XC}[n(\mathbf{r})]$, i.e.,

$$F[n(\mathbf{r})] = T_s[n(\mathbf{r})] + E_H[n(\mathbf{r})] + E_{XC}[n(\mathbf{r})] \tag{2.20}$$

Here,

$$\begin{aligned} T_s[n(\mathbf{r})] &= -\frac{1}{2}\sum_{i=1}^{N}\int \psi_i^*(\mathbf{r})\nabla^2\psi_i(\mathbf{r})d\mathbf{r} \\ E_H[n(\mathbf{r})] &= \frac{1}{2}\iint \frac{n(\mathbf{r})n(\mathbf{r}')}{|\mathbf{r}-\mathbf{r}'|}d\mathbf{r}d\mathbf{r}' \\ E_{XC}[n(\mathbf{r})] &= T[n(\mathbf{r})] - T_s[n(\mathbf{r})] + E_{int}[n(\mathbf{r})] - E_H[n(\mathbf{r})] \end{aligned}$$

Where $E_{XC}$ contains the difference between the exact and non-interacting kinetic energy and also the non-classical contribution to the electron-electron interaction, of which the exchange energy is a part. The KS theory is approximate because of unknown $E_{XC}[n(\mathbf{r})]$. It is important to know the accurate $E_{XC}[n(\mathbf{r})]$ in order to describe the realistic condensed matter system. The most widely used approximation for the XC potential are the Local Density Approximation (LDA) and the Generalized Gradient Approximation (GGA). By minimizing the energy functional $E[n(\mathbf{r})] = F[n(\mathbf{r})] + \int n(\mathbf{r})V_{ext}(\mathbf{r})d\mathbf{r}$, which is subject to the conservation condition, we will obtain the ground state energy of many body electron system.

$$\delta\left[F[n(\mathbf{r})] + \int n(\mathbf{r})V_{ext}(\mathbf{r})d\mathbf{r} - \mu(\int n(\mathbf{r})d\mathbf{r} - N)\right] = 0 \tag{2.21}$$

Then, the resulting equation is

$$\begin{aligned} \mu &= \frac{\delta F[n(\mathbf{r})]}{\delta n(\mathbf{r})} + V_{ext}(\mathbf{r}) \\ &= \frac{\delta T_s[n(\mathbf{r})]}{\delta n(\mathbf{r})} + V_{ks}(\mathbf{r}) \end{aligned} \tag{2.22}$$

where

$$\begin{aligned} V_{ks}(\mathbf{r}) &= V_{ext}(\mathbf{r}) + V_{H}(\mathbf{r}) + V_{XC}(\mathbf{r}) \\ &= V_{ext}(\mathbf{r}) + \frac{\delta E_{H}[n(\mathbf{r})]}{\delta n(\mathbf{r})} + \frac{\delta E_{XC}[n(\mathbf{r})]}{\delta n(\mathbf{r})} \end{aligned} \tag{2.23}$$

The KS equation must be solved self consistently because $V_{KS}(\mathbf{r})$ depends on the density. To calculate the density, N number of KS equations have to be solved unlike the one equation in the case of TF method. However, the problem is still less difficult because we just need to solve the increased number of single electron equations.

The KS eigenvalues have no physical meaning. Therefore, the total energy cannot be simply obtained by doing the sum of all the eigenvalues of the occupied states, i.e., $E_{tot} \neq \sum_i^{occ} \epsilon_i$. The eigenvalue is the derivative of the total energy with respect to occupation of state.

$$\begin{aligned} \epsilon_i &= \frac{dE_{total}}{dn_i} \\ &= \int \frac{dE_{total}}{dn_i} \frac{dn(\mathbf{r})}{dn_i} d\mathbf{r} \end{aligned} \tag{2.24}$$

#### 2.4.3.1 Exchange-Correlation functional

There are variety of approximations made to obtain the exchange-correlation energy, $E_{XC}$. Depending upon the functional dependence on one or more quantities such as local density ($n(\mathbf{r})$), gradient of the local density ($\nabla n(\mathbf{r})$), the Laplacian of the density ($\nabla^2 n(\mathbf{r})$) and the kinetic energy density ($\tau = \sum_i (\nabla_i^{ks})^2$), the $E_{XC}$ can be classified as LDA, GGA, meta-GGA and hybrid functionals. Lets see how the various functional depends on the above mentioned quantities.

$$\begin{aligned} E_{XC}^{LDA}(\mathbf{r}) &= E_{XC}^{LDA}[n(\mathbf{r})] \\ E_{XC}^{GGA}(\mathbf{r}) &= E_{XC}^{GGA}[n(\mathbf{r}), \nabla n(\mathbf{r})] \\ E_{XC}^{meta-GGA}(\mathbf{r}) &= E_{XC}^{GGA}[n(\mathbf{r}), \nabla n(\mathbf{r}), \nabla^2 n(\mathbf{r}), \tau] \\ E_{XC}^{hybrid-GGA}(\mathbf{r}) &= a_x E_{HF}^{exact} + E_{XC}^{GGA}[n(\mathbf{r}), \nabla n(\mathbf{r})] \end{aligned} \tag{2.25}$$

(where $E_{HF}^{exact}$ is exact Hartree-Fock energy) Although many approximations are made to get accurate results, it fails to describe the chemical systems and their properties accurately. Say, for example, B3LYP, which is a popular hybrid functionals, is suitable for describing molecules but not for solids[68–70]. On the other hand, PBE[71], a GGA funtional, suits to describe the periodic systems like solids and surface but fails to describe the molecular properties[68].

LDA overestimate the bond strength in solids and cohesive energy by 1% while GGA underestimate the bond strength hence bulk moduli, phonon frequencies and magnetic moment. Both GGA and LDA underestimate the energy gap in semiconductor and insulator[70].

GGA predicts the correct ground state for magnetic transition metals whereas LDA fails to do so[72]. LDA incorrectly predicts that the most stable ground state structure of Fe to be non-magnetic hexagonal close-packed structure[73, 74] while GGA correctly predicted it to be ferromagnetic body-centered cubic structure[75]. Another example for the accurate magnetic structure prediction of GGA is body-centered cubic Cr, in this case, LDA wrongly predicts bcc Cr is non-magnetic but GGA correctly predict it to be antiferromagnetic[76].

### 2.4.4 Solving Kohn-Sham equation

With the help of independent-particle method, KS equations helps us to find the exact density and ground state energy of the systems. As the effective single-particle potential, $V_{KS}$ is closely related to electron density $n(\mathbf{r})$, the KS equation has to be solved self consistently. Figure 2.1 shows the flow chart of self consistent iterations carried out numerically. The process begins with the initial guess of electron density, for example, superposition of atomic electron density, after which the effective potential $V_{KS}$ is calculated and then KS equation is solved, followed by a calculation of new electron density from the new KS wave function $\psi_i^{KS}$. Then, the difference of total energy between the new iteration and the old one is found. If this difference is less than assigned small value, then the process terminates and the quantities such as total energy, force, stress, eigenvalues, electronic density of states, electronic band structure, etc.. can be calculated. If the difference is greater than assigned value, then the iteration continue with the new charge density derived by mixing the current charge density with those from the previous iteration.

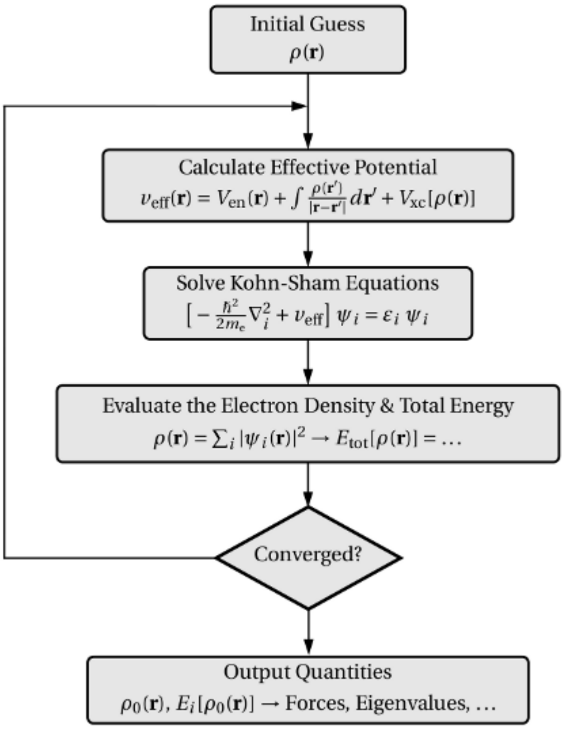

**Figure 2.1:** *Flow chart of self consistent iteration scheme[77].*

### 2.4.5 Basis set

In variational method, the wave functions are represented as a linear combination of basis functions. The accuracy of wave function representation depends on the numbers of basis functions included in the expansion and on the features of the original function. For a given number of terms in the expansion, smoother functions are represented more accurately than discontinuous functions.

Different basis sets are used to represent the wave function but the exact choice depends on the system of interest. For the molecular systems, the wave functions are expressed in terms of molecular orbitals basis functions which in turn expressed in terms of atomic orbitals. This method is called Linear Combination of Atomic Orbitals-Molecular Orbitals. In the case of solids and surface systems, which are periodic in nature, the wave function of electrons are expressed in terms of plane wave basis sets.

#### 2.4.5.1 Localised basis sets

Let us consider hydrogen atom. To represent it's single 1s electron, one Slater-Type Orbital (STO) is adequate whereas two STO's are required to represent the bonding and anti-bonding orbitals of hydrogen molecules. STOs basis sets are difficult as the integrals in the secular determinant are difficult to evaluate. This issue could be resolved if the Gaussian-Type Orbitals (GTO) are adopted as basis sets. Both the STOs and GTOs are popular choice for the atoms and molecules as their orbitals are highly localized around each atom. For a single atom to be represented in this local basis set, it requires 10-20 basis functions. Because of local nature of this basis, accuracy of the results is limited. Since the metals have long-range interactions, it cannot be represented in this local basis set. The basis set superposition error exists in both STO and GTO basis set. Because of this error, the calculated interaction energy of dimer is found to be higher than the correct value while the equilibrium bond length is underestimated.

#### 2.4.5.2 Plane waves

Plane waves (PW) are non-local and span the entire space. The advantages of using a plane waves basis are the evaluation of Hamiltonian is simple due to the orthogonality nature of plane waves and basis set superposition error can be avoided. As it covers the whole space, the number of plane waves required to represent the vacuum region is the same as the atoms. A higher number of plane waves are needed to describe the rapid oscillation of the valence electron orbital near the nucleus in the PW basis set. With the help of the pseudopotential approach, the representation of the rapid oscillation is however circumvented. VASP, Quantum ESPRESSO and ABINIT are some of the popular DFT packages. DFT calculations carried out for our research work have been performed using the Vienna Ab initio Simulation Package (VASP) which implements DFT using plane-waves and pseudopotentials[78–80]. In the following section, we discuss the plane-wave based DFT in detail, and also the parameters need to be taken care of while performing the calculations.

### 2.4.6 Plane wave DFT

#### 2.4.6.1 Bloch theorem

The free electrons in the solid are represented by the plane waves. Since, the electrons in the solids are subjected to a periodic potential, the wave function can be written as the product of the plane wave, $exp(i\mathbf{k.r})$ and the cell-periodic part $u_k(\mathbf{r})$, i.e.,

$$\psi_k(\mathbf{r}) = exp(i\mathbf{k.r})u_k(\mathbf{r}) \tag{2.26}$$

This is called Bloch's theorem. The cell periodic part $u_k(\mathbf{r})$ can be written as the linear combination of the plane waves with the reciprocal lattice vectors G as the wave vector. i.e.,

$$u_k(\mathbf{r}) = \sum_G C_{i,G} exp(i\mathbf{G} \cdot \mathbf{r}) \tag{2.27}$$

Combining the above two equations, the electronic wave function can be written as the sum of plane waves.

$$\psi_k(\mathbf{r}) = \sum_G C_{k+G} exp[i(\mathbf{k} + \mathbf{G}) \cdot \mathbf{r}] \tag{2.28}$$

The Bloch wave function $\psi_k(\mathbf{r})$ help to overcome the two difficulties namely calculation of infinite number of wave function and the requirement of infinite number of basis functions for the expansion of wave function[81].

#### 2.4.6.2 k-point sampling

Due to periodicity nature of crystals, Bloch's theorem transform the problem of calculating the infinite number of electronic wave functions to the finite number of wave functions at infinite number of k-points in Brillouin Zone (BZ). The occupied state at a k-point contribute to the electronic potential. To compute this potential, an infinite number of calculations are required. However, the electronic wave function at k-point that are very close together will be same. Therefore, the electronic wave function over a region of k-space is reduced to finding wave function at a single k-point. Thus, only a finite number of k-points is required to find the electronic potential and hence the total energy of the system[81].

The physical quantities such as total energy and charge density are calculated by integrating the integrand, $g(k)$ in the reciprocal space (k). The property of the system in the plane wave basis can be written as

$$g(\mathbf{r}) = \frac{V_{cell}}{(2\pi)^3} \int g(\mathbf{k})\, d\mathbf{k} \tag{2.29}$$

Computationally, the integrals over all possible values of k in the BZ becomes summation over a chosen set of k-points so as to achieve convergence of the property.

$$g(\mathbf{r}) = \sum_{j=1} P(n_j)\, w_j\, g(\mathbf{k}_j) \tag{2.30}$$

A special set of k-points called the Monkhorst-Pack grid[82] is used in the plane-wave calculation.

#### 2.4.6.3 Energy cutoff

In the PW DFT, infinite number of PWs are used to represent the electronic wave function. As the solution with lower energies are more important than those with large kinetic energy, the PW series can be truncated. Thus, a cutoff is set for the energy of PW, so that the plane waves with energy less than this assigned cutoff can be included to represent the electronic wave function. The cutoff energy $E_{cut}$ is defined as

$$E_{cut} \geq 1/2(\mathbf{k} + \mathbf{G})^2 \tag{2.31}$$

The cutoff energy is system dependent and it is required to perform calculations with different higher cutoff energy until the convergence is achieved. Now, the PW expansion of the electronic wave function becomes

$$\psi_k(r) = \sum_{|\mathbf{k}+\mathbf{G}|cut} C_{\mathbf{k}+\mathbf{G}} exp[i(\mathbf{k} + \mathbf{G}).\mathbf{r}] \tag{2.32}$$

Let us find the relation between the number of plane waves, $N_{PW}$ required to describe the wave function and the energy cutoff, $E_{cut}$. The volume of the sphere containing all PWs is given as

$$V_{sphere} = \frac{4\pi}{3} G_{max}^3 \tag{2.33}$$

And the volume occupied by one PW is

$$V_{PW} = \frac{(2\pi)^3}{V_{cell}} \tag{2.34}$$

Then,

$$\begin{aligned} N_{PW} \times V_{PW} &= V_{sphere} \\ N_{PW} &\approx \frac{1}{2\pi^2} \Omega G_{max}^3 \\ &\propto E_{cut}^{3/2} \end{aligned} \tag{2.35}$$

It is noted here that the number of k-points is reduced by k-point sampling. Similarly, the number of G-vectors is reduced by assigning the energy cutoff[81]. Thus, the PW expansion approach becomes tractable.

#### 2.4.6.4 Pseudopotential

When the atoms are brought together to form a solid, the core electrons in each atoms stick tightly to their nuclei in a deep potential well due to the strong Coulomb potential by nuclei. They are so localized and their participation in bonding is minimal. The valence electrons are the ones which give major contribution to bonding in solids, being ionized, conducting electricity in metals, forming bands, and performing other atomic activities. To ease the calculation, the core electrons are removed from the picture and deal with only valence electrons. This is called frozen core approximation.

When a valence wave function passes by the highly localized core region, it oscillates rapidly with many wiggles to be orthogonal to the core states. The representation of the valence electronic wave function with many nodes is very tedious task. It is not easy to represent in simple function as well as difficult to solve computationally.

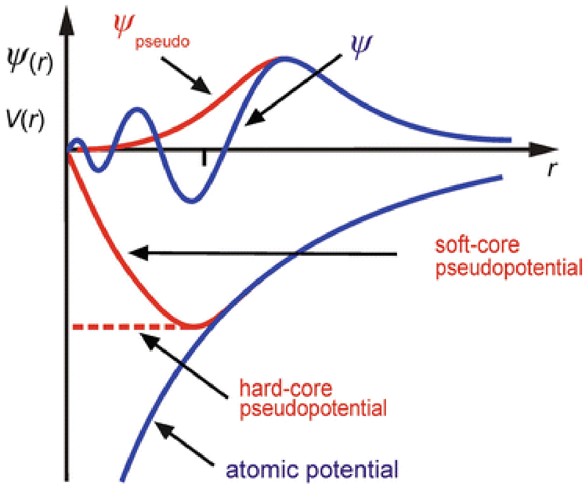

**Figure 2.2:** *The schematic representation of the all-electrons (blue) and pseudo-potentials (red) and corresponding wave functions*[83].

Within the frozen core approximation, the valence electrons becomes low lying states and there is no core electrons underneath with which to be orthogonal. So, the wave function of the valence electrons and their potential with ions can be replaced with smoother wave function and effective potential in the core region defined by cutoff radius $r_c$, where no oscillations are present. This procedure is called *pseudization* which is shown schematically in the Fig. 2.2. The replacement by nodeless wave function reduces the number of basis functions needed and it does not affect the calculation results much as only the core part is replaced. There are various ways of constructing the pseudopotential. In the norm conserving pseudopotenial[84] the pseudo and all electron charge densities within the core are constructed to be equal. Ultrasoft pseudopotentials[85] are not only eliminate the radial node but also shift the peak position of a wave function to a bigger $r_c$ with reduced peak height so it can be easily expanded with a small number of PWs. In 1994, Blochl proposed the Projected Augmented Wave (PAW)[86] method. This method possess both accuracy and efficiency. In this method, the core region is expanded by a set of localized atomic-like basis function and the valence part is expanded by a smooth pseudo wave function. The region where the atomic basis functions should be expanded is defined by the augmentation sphere around each atom. PAW method gives all electron charge density of valence orbitals which cannot be obtained by other pseudopotentials.

#### 2.4.6.5 Smearing

There is a difficulty in calculating the integral in k-space. That is, the function such as charge density which changes discontinuously from 0 to 1 at the Fermi surface in the case of metal, needs a large number of k-points to get converged result. So to overcome this issue, two popular methods namely smearing method and tetrahedron method have been proposed. In the smearing method, the discontinuous function which has to be integrated is replaced with continuous function by smearing out the discontinuity. Both the extreme cases of smearing, i.e., too large/small, does not help to resolve this problem of requirement of more k-points. Small smearing need more k-points thus it slow down the calculation speed while large smearing gives wrong total energy. Thus, the proper balance is necessary[87]. The effect of smoothening the step function is similar to introduction of fictituous electronic temperature to the system as well as the introduction of the partial occupancies which contribute the entropy to the system. The electronic temperature introduced to the system can be taken back to 0 K by extrapolation after the calculations are done with the smearing technique. The smearing function used in this method are Gaussian-type $\delta$ function, Fermi-Dirac distribution function, and the method developed by Methfessel and Paxton[88] which uses much complicated function than the simple Fermi-Dirac function. In the tetrahedron method, the Irreducible Brillouin Zone (IBZ) is divided into tetrahedrons and the function to be integrated is defined in each point of the tetrahedron using interpolation. After the interpolation, the integration of the function has been carried out all over the space instead of special k-point in IBZ. Blochl interpolation method improves the results of metal than the simple linear interpolation. This tetrahedron method is suitable for transition metals and rare earth where Fermi surfaces requires a higher resolution.

# 3

# Point defect formation energy and solubility in bcc ferromagnetic iron

## 3.1 Introduction

Stainless steels are the predominant structural material in nuclear power plants. Ferritic and ferritic martensitic steels are known for better dimensional stability than austenitic steels under neutron irradiation. These steels are however limited to operate below 600 °C[**15**, **89**]. Oxide Dispersion Strengthened (ODS) steels have been developed to achieve higher operating temperatures. These modern steels are multicomponent alloys (with about 20 components[**15**] Fe, C, Mn, P, Si, Ni, Cr, Mo, V, Ti, Co, Cu, Al, B, W, Zr, N, O, Y) made up of Fe-Cr ferritic matrix in which a homogeneous dense distribution of small precipitate particles is created by ball milling and subsequent consolidation process involving either hot extrusion or hot isostatic pressing. These ODS steels have superior creep resistance and stability under irradiation attributed to the finest oxide particles densely dispersed in the ferritic matrix with high dislocation density. These nanoprecipitates have been the subject of many characterization studies. They are found to be very stable even at high temperatures close to the solidus of the ferritic matrix. Stability of the microstructure of these steels under irradiation also is important for their long-term service in nuclear power plants. Some experimental studies suggest that the nanoparticles are stable under irradiation but other studies report their dissolution. Thus the evolution of size and population of these dispersed nanoparticles is not well understood[**90**].

But formation of precipitates is governed by diffusion kinetics of solute elements in the solvent matrix. Vacancy and solute formation energies and solute-solute and vacancy-solute binding energies are important parameters governing the diffusion of solute elements hence nucleation, growth, and coarsening of precipitates[91–95]. First-principles electronic structure calculations offer the most accurate means to develop an atomic level understanding of the interactions of solutes and point defects in solids[91, 96]. Fu *et al.* have shown that the unusual high solubility of oxygen atoms and nucleation of stable oxygen enriched nanoparticles in defect containing Fe is determined by the formation and binding energies of vacancies, oxygen, and other solutes present in iron[97]. Modelling studies of clustering of atomic defects and swelling also suggests that accurate characterization of the interactions of solutes with point defects is important[96, 98–103].

Given these connections between formation and binding energies of atomic defects and diffusion kinetics and hence evolution of microstructure and mechanical properties of steels, several researchers have studied the interactions of solute elements with point defects in bcc iron employing first-principles computational methods[53, 54, 104] based on the electronic Density Functional Theory (DFT). These studies have however considered mainly $sp$ and transition elements. Further, the specifications of the DFT calculations are not consistent among themselves. Olsson *et al.* and You *et al.* have carried out their DFT total energy calculations under constant volume conditions[53, 104]. Gorbatov *et al.* have done the DFT calculations by Green function method with atomic sphere approximation which precludes relaxation of ionic coordinates. They themselves have indicated that the vacancy-solute binding energies of certain solutes (Sc, Ti, Mo) are extremely sensitive to the extent of structural relaxation included in the calculations[54]. Partly relaxed or unrelaxed calculations can thus give different results[50, 105–108].

Here, using DFT total energy calculations with complete relaxation of structural degrees of freedom (ionic coordinates, shape and size of the unit cell) and uniform specifications of k-mesh, plane wave basis set cut off energy and size of the simulation cell, I go beyond the set of solute elements considered in the previous works and make a large database of predictions of solute formation energies, solute-solute, and vacancy-solute binding energies for an extended set of 53 different solute elements, with atomic numbers 1 to 54, in bcc ferromagnetic iron. I then analyze the results of these calculations to identify physical trends in the formation and binding energies of the solutes. I note here that the results of formation energies and volumes of point defects and their analysis are presented in this chapter. Binding energies of vacancy-solute and solute-solute pairs and their correlations with solute size factors and formation energies are presented in the next chapter.

I also would like to note here that though the alkali metals and noble gas atoms do not generally alloy with iron, knowledge of their energetics in iron matrix will be useful to see trends in the solution behaviour of atoms in iron. Further, fission products (including those from molten salt reactors) include elements from alkaline earth, alkali, halogen and noble gas elements. For modelling the interactions of these fission products with steel cladding as well as for modelling nuclide distribution between steelmaking phases upon melting of sealed radioactive sources hidden in scrap, knowledge of their formation energies are useful[**109**, **110**]. Furthermore, oxygen and yttrium atoms are practically immiscible in Fe but ODS steels are produced through mechanical alloying. Similarly, ion beam mixing is used to mix immiscible Ag, In and Na in Fe[**111**, **112**]. Ion implantation is also used for similar purposes[**113**, **114**]. For modelling of such alloying approaches, energetics of these solutes will be useful.

I note further that interactions of self-interstitial atom defects with vacancies and solute elements are also important for a robust understanding of atomic transport in steels. I do not however consider self-interstitial atom defects in this work.

## 3.2 Computational method

We have considered all elements with Z=1 to 54 as solute atoms in bcc Fe. H, C, N, and O were considered as interstitial solute atoms and other atoms as substitutional solutes. Among the interstitial solute atoms, H has been considered as a tetrahedral interstitial solute while the other atoms as octahedral interstitial solutes in accordance with their site preference[115–120]. In order to create point defects in bcc iron we have used supercell method. Point defects were introduced into the supercell by adding and/or removing appropriate atoms. An isolated vacancy was created by removing a Fe atom at a given lattice site. Substitutional atom defects were created by replacing a single Fe atom with a solute atom. This is illustrated in Fig. 3.1. In this figure, we also define point defect pair configurations which are studied in the next chapter.

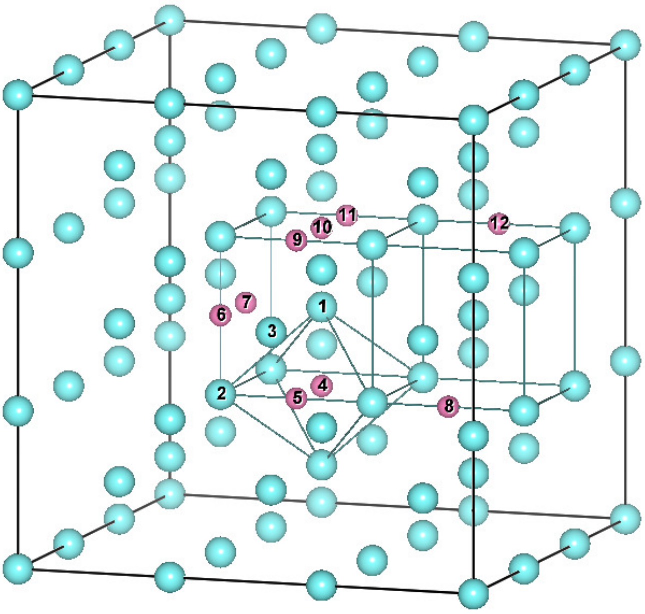

**Figure 3.1:** *BCC* $3 \times 3 \times 3$ *supercell with labeled atoms to define atomic defect configurations. Labels 1, 2 and 3 represent substitutional sites. Labels 4 to 12 represent octahedral interstitial sites. Solute-solute nearest neighbor pair configuration was obtained by substituting the Fe atoms at sites 1 and 2 with the given solute atoms. Vacancy-solute first and second nearest neighbor pairs were formed by placing the given solute atom at site 2 or 3, respectively, while site 1 is made vacant. A single interstitial atom defect was formed by placing the atom at site 4. Configurations of pairs of interstitial atoms were created by placing them at pairs of sites 5-6, 5-7, 5-8, 5-9, 5-10, 5-11, and 5-12, respectively, in accordance with Domain et al.[117]. Vacancy-interstitial pairs were formed by removing the atom at site 1 and placing an interstitial atom at site 4 or 5, respectively, for 1nn and 2nn configurations[117]. Tetrahedral interstitial sites are not indicated.*

The formation energy of a defect is a measure of the amount of energy needed to form the defect. The vacancy and solute formation energies were computed from the following expressions[53, 121]. The formation energy for a vacancy, $E_f^{\square}$, (where $\square$

denotes a vacancy) in bcc iron is calculated from[53]

$$E_f^{\square} = E(Fe_{N-1}\square_1) - \frac{N-1}{N}E(Fe_N) \tag{3.1}$$

where $E(Fe_{N-1}\square_1)$ is the total energy of an iron supercell with N lattice sites containing a single vacancy and (N-1) Fe atoms. $E(Fe_N)$ is the total energy of bcc iron supercell with N lattice sites without vacancy defect.

The expression for the formation energy of a substitutional solute, $E_f^X$, (where a solute atom is denoted by X) is given by[121]

$$E_f^X = E(Fe_{N-1}X_1) - \frac{\left[N - \left(1 + \frac{m}{n}\right)\right]}{N}E(Fe_N) - \frac{1}{n}E(Fe_mX_n) \tag{3.2}$$

where $E(Fe_{N-1}X_1)$ is the total energy of the iron supercell with N lattice sites containing a solute X and (N-1) Fe atoms. $Fe_mX_n$ is the reference phase in our calculation of solute formation energy. It is the second phase with which the solid solution phase is in equilibrium (with a common boundary in the phase diagram). It can be a compound phase, elemental crystal, molecules or atoms. Information regarding the second phases in the Fe-X binary systems were obtained from ASM Alloy Phase Diagrams Database[122–124]. $E(Fe_mX_n)$ is the total energy of $Fe_mX_n$. For an interstitial solute (denoted again by X), the expression for $E_f^X$ is the same except that (N-1) and $(1 + \frac{m}{n})$ are replaced by N and $(\frac{m}{n})$ respectively.

In addition to chemical interactions, the size of the solute atoms also influences the interaction energies of the atomic defects. Therefore, the size factor of solute, SF(X), in bcc iron has been computed using the definition from Hepburn *et al.*[96]:

$$SF(X) = \frac{\Delta V}{V_{ave}} = \frac{V_X - V_{ave}}{V_{ave}}. \tag{3.3}$$

where $V_{ave} = \frac{V(Fe_{N-1}X_1)}{N}$ and $V_X = V(Fe_{N-1}X_1) - \frac{N-1}{N}V(Fe_N)$. $V(Fe_{N-1}X_1)$ and $V(Fe_N)$ are calculated equilibrium volumes of $Fe_{N-1}X_1$ and $Fe_N$ supercell systems respectively. Size factors of interstitial solutes are defined in a similar manner.

The total energies required in the calculations of formation and binding energies defined above were computed using 3 × 3 × 3 bcc supercells of 54 lattice sites. Previous DFT works on this topic indicates that 3 × 3 × 3 supercell is generally adequate[**53**, **107**, **115**, **120**, **125**, **126**]. The DFT total energy calculations have been performed using the Vienna Ab initio Simulation Package (VASP)[**78**, **80**]. Projector Augmented Wave (PAW) potentials[**79**,**86**] were used for all the elements considered in this work. For exchange-correlation functional, the generalized gradient approximation by Perdew, Burke, and Ernzerhof (PBE)[**71**] was used. All the total energy calculations were fully relaxed with respect to volume as well as all cell-internal and cell-external degrees of freedom, converged to $10^{-8}$ eV. Methfessel-Paxton order 1 smearing[**88**] of the Fermi surface was used with a smearing width of $\sigma$=0.2 eV. It is known that the spin-unpolarized (nonmagnetic) state of bcc Fe is higher in energy than the magnetic state and spin-polarized calculations are necessary to establish its ferromagnetic ground state[**107**]. The energy difference between the spin-unpolarized and spin-polarized state of Fe can influence the formation and binding energies of solute atoms. Therefore, spin-polarized calculations have been performed for all supercells representing pure bcc ferromagnetic iron and bcc iron matrix with vacancy, solute, solute-solute and vacancy-solute defects. A cutoff energy of 500 eV was used for the plane wave expansion of the electron wave functions. Extensive tests of k-point sampling has indicated that an extremely dense grid of k-points is required for converged atomic defect calculations. Therefore, a 8 × 8 × 8 k-point mesh generated using the Monkhorst-Pack scheme was used to sample the Brillouin zone. In addition to the total energy of the system, spin-polarized calculations provide the local magnetic moments of the atoms which can be used to establish the accuracy of our calculations.

With these specifications, the lattice parameter and magnetic moment of bcc Fe were predicted to be 2.84 Å and 2.23 $\mu_B$/atom respectively. These values are in good agreement with the experimental values of 2.86 Å and 2.2 $\mu_B$/atom[**127**]. Further the vacancy formation energy $E_f^{\square}$=2.18 eV obtained from our calculation is in good agreement with the previously published theoretical values of 2.18 eV[**128**] and 2.17 eV[**115**] as well as with the positron annihilation experimental value of 2.0±0.2 eV[**129**].

### 3.2.1 Reference systems

For the calculation of solute formation energies (also known as heat or enthalpy of solution) in bcc Fe, as defined in Eq. 3.2, total energies of the elemental solutes (X) or Fe-X binary compounds, whichever is in equilibrium with the solid solution phase (Fe), known as reference states or systems, are required. For this, we performed a set of high-precision calculations for the ground-state structure of all the pertinent elements and compounds. The crystal structures of the elements and compounds include body centered cubic (bcc), face centered cubic (fcc), hexagonal close packed (hcp), tetragonal, orthorhombic and trigonal symmetries with nonmagnetic, ferromagnetic, or antiferromagnetic orders. The ground state crystallographic parameters were determined through full relaxation of the unit cell and atomic positions. To ensure that the total energies and lattice parameters were determined accurately, we used a plane wave cutoff energy of 500 eV, a high-density Monkhorst-Pack k-points grid to sample the Brillouin zone, and an energy tolerance of $10^{-8}$ eV. We tested convergence with respect to k-points mesh for each system beginning with a coarse mesh, and k-points meshes used for all the systems are listed in Table 3.1. With these settings the lattice parameters of most of the elements and compounds were reproduced within ±2% of experimental lattice parameters which are also listed in Table 3.1.

For H, F, Cl, and Br, the spin polarized electronic energy of their free diatomic molecules have been used as their reference state energy. We have performed these free molecular calculations by placing a single diatomic molecule in a 7 Å cubic cell and optimizing the bond length. Optimized bond lengths (0.75, 1.42, 1.99, 2.32 Å) were found to be in good agreement with their respective experimental bond lengths (0.74, 1.41, 1.99, 2.27 Å).

**Table 3.1:** *Calculation details for the ground state total energy of elemental (X) and binary Fe-X phases considered as reference systems for the formation energy of solutes (X) in bcc Fe. Space group, magnetic order, lattice parameters (a, b, c) (Å), k-mesh and valence electron configurations of the solutes (X) in their respective VASP-PAW potentials are listed. Space groups are given along with space group numbers in parentheses. Labels NM, FM and AFM denote nonmagnetic, ferromagnetic, and antiferromagnetic orders, respectively. Calculated equilibrium lattice parameters are compared with experimental values given in parentheses. Measured crystal structure data of the elements and Fe-X binary compounds were taken from Pearson's Handbook of Crystallographic Data[**123**] and Pauling file[**124**]. The size of the simulation box used for free atom and free molecule systems is also denoted by 'a'.*

| Phase | Space group | Magnetic order | Lattice parameter | k-mesh | Valence shell of X |
|---|---|---|---|---|---|
| H | Free molecule | NM | a=7 | 1 × 1 × 1 | $1s^1$ |
| He | Free atom | NM | a=12 | 1 × 1 × 1 | $1s^2$ |
| Li | Im-3m(229) | NM | a=3.440(3.510) | 17 × 17 × 17 | $2s^1 2p^0$ |
| $FeBe_2$ | P63/mmc(194) | FM | a=4.175(4.212)<br>c=6.794(6.853) | 7 × 7 × 7 | $2s^2 2p^0$ |
| $Fe_2B$ | I4/mcm(140) | FM | a=5.054(5.117)<br>c=4.236(4.252) | 9 × 9 × 9 | $2s^2 2p^1$ |
| $Fe_3C$ | Pnma(62) | FM | a=5.021(5.078)<br>b=6.740(6.733)<br>c=4.480(4.519) | 11 × 11 × 11 | $2s^2 2p^2$ |
| $Fe_4N$ | Pm-3m(221) | FM | a=3.795(3.795) | 7 × 7 × 7 | $2s^2 2p^3$ |
| FeO | Fm-3m(225) | AFM | a=4.312(4.321) | 17 × 17 × 17 | $2s^2 2p^4$ |
| F | Free molecule | NM | a=7 | 1 × 1 × 1 | $2s^2 2p^5$ |
| Ne | Free atom | NM | a=12 | 1 × 1 × 1 | $2s^2 2p^6$ |
| Na | Im-3m(229) | NM | a=4.200(4.290) | 17 × 17 × 17 | $3s^1 3p^0$ |
| Mg | P63/mmc(194) | NM | a=3.200(3.210)<br>c=5.200(5.210) | 17 × 17 × 17 | $3s^2 3p^0$ |
| $Fe_3Al$ | Fm-3m(225) | FM | a=5.744(5.800) | 7 × 7 × 7 | $3s^2 3p^1$ |
| FeSi | P213(198) | FM | a=4.450(4.484) | 9 × 9 × 9 | $3s^2 3p^2$ |
| $Fe_3P$ | I-4(82) | FM | a=9.051(9.107)<br>c=4.382(4.460) | 4 × 4 × 7 | $3s^2 3p^3$ |
| FeS | P63/mmc(194) | AFM | a=3.410(3.448)<br>c=5.710(5.744) | 15 × 15 × 15 | $3s^2 3p^4$ |
| Cl | Free molecule | NM | a=7 | 1 × 1 × 1 | $3s^2 3p^5$ |
| Ar | Free atom | NM | a=12 | 1 × 1 × 1 | $3s^2 3p^6$ |
| K | Im-3m(229) | NM | a=5.30(5.33) | 17 × 17 × 17 | $3p^6 4s^1$ |

Continued on next page

**Table 3.1 – continued from previous page**

| Phase | Space group | Magnetic order | Lattice parameter | k-mesh | Valence shell of X |
|---|---|---|---|---|---|
| Ca | Fm-3m(225) | NM | a=5.53(5.58) | 17 × 17 × 17 | $3s^23p^64s^2$ |
| $Fe_2Sc$ | P63/mmc(194) | FM | a=4.920(4.937)<br>c=8.066(8.038) | 9 × 9 × 7 | $3s^23p^64s^2$<br>$3d^1$ |
| $Fe_2Ti$ | P63/mmc(194) | AFM | a=4.705(4.757)<br>c=7.811(7.829) | 7 × 7 × 5 | $3p^63d^34s^1$ |
| FeV | P42/mnm(136) | FM | a=8.987(8.965)<br>c=4.580(4.633) | 5 × 5 × 9 | $3p^63d^44s^1$ |
| Cr | Im-3m(229) | AFM | a=2.88(2.91) | 17 × 17 × 17 | $3p^63d^54s^1$ |
| Mn | I-43m(217) | NM | a=8.57(8.91) | 6 × 6 × 6 | $3p^64s^23d^5$ |
| Fe | Im-3m(229) | FM | a=2.84(2.86) | 17 × 17 × 17 | $3p^64s^13d^7$ |
| FeCo | Pm-3m(221) | FM | a=2.846(2.856) | 17 × 17 × 17 | $3d^84s^1$ |
| FeNi | P4/mmm(123) | FM | a=2.520(2.533)<br>c=3.581(3.582) | 17 × 17 × 17 | $3d^84s^2$ |
| Cu | Fm-3m(225) | NM | a=3.63(3.61) | 17 × 17 × 17 | $3d^{10}4s^1$ |
| $Fe_3Zn_{10}$ | I-43m(217) | FM | a=8.976(8.978) | 5 × 5 × 5 | $3d^{10}4s^2$ |
| $Fe_3Ga$ | Pm-3m(221) | FM | a=3.658(3.679) | 17 × 17 × 17 | $4s^24p^1$ |
| $Fe_3Ge$ | P63/mmc(194) | FM | a=5.142(5.160)<br>c=4.224(4.210) | 9 × 9 × 9 | $4s^24p^2$ |
| $Fe_2As$ | P4/nmm(129) | AFM | a=3.635(3.634)<br>c=5.920(5.985) | 6 × 6 × 3 | $4s^24p^3$ |
| FeSe | P4/nmm(129) | FM | a=3.600(3.710)<br>c=5.880(6.010) | 13 × 13 × 9 | $4s^24p^4$ |
| Br | Free molecule | NM | a=7 | 1 × 1 × 1 | $4s^24p^5$ |
| Kr | Free atom | NM | a=12 | 1 × 1 × 1 | $4s^24p^6$ |
| Rb | Im-3m(229) | NM | a=5.59(5.67) | 17 × 17 × 17 | $4p^65s^1$ |
| Sr | Fm-3m(225) | NM | a=6.02(6.08) | 17 × 17 × 17 | $4s^24p^65s^2$ |
| $Fe_{17}Y_2$ | P63/mmc(194) | FM | a=8.481(8.462)<br>c=8.257(8.282) | 5 × 5 × 5 | $4s^24p^65s^2$<br>$4d^1$ |
| $Fe_2Zr$ | Fd-3m(227) | FM | a=7.043(7.017) | 9 × 9 × 9 | $5s^24d^15p^1$ |
| $Fe_2Nb$ | P63/mmc(194) | AFM | a=4.774(4.840)<br>c=7.793(7.895) | 9 × 9 × 9 | $4p^65s^14d^4$ |
| $Fe_2Mo$ | P63/mmc(194) | FM | a=4.675(4.745)<br>c=7.797(7.734) | 9 × 9 × 9 | $4p^65s^14d^5$ |

Continued on next page

**Table 3.1 – continued from previous page**

| Phase | Space group | Magnetic order | Lattice parameter | k-mesh | Valence shell of X |
|---|---|---|---|---|---|
| FeTc | P42/mnm(136) | FM | a=9.105(9.130)<br>c=4.885(4.788) | $5 \times 5 \times 9$ | $4p^6 5s^1 4d^6$ |
| Ru | P63/mmc(194) | NM | a=2.73(2.71)<br>c=4.32(4.28) | $17 \times 17 \times 17$ | $4p^6 5s^1 4d^7$ |
| FeRh | Pm-3m(221) | FM | a=3.016(2.989) | $17 \times 17 \times 17$ | $4p^6 5s^1 4d^8$ |
| FePd | P4/mmm(123) | FM | a=2.738(2.722)<br>c=3.751(3.715) | $17 \times 17 \times 17$ | $5s^1 4d^9$ |
| Ag | Fm-3m(225) | NM | a=4.160(4.080) | $17 \times 17 \times 17$ | $5s^1 4d^{10}$ |
| Cd | P63/mmc(194) | NM | a=3.050(2.980)<br>c=5.700(5.620) | $17 \times 17 \times 17$ | $5s^2 4d^{10}$ |
| In | I4/mmm(139) | NM | a=3.33(3.25)<br>c=4.96(4.95) | $17 \times 17 \times 17$ | $5s^2 5p^1$ |
| FeSn | P6/mmm(191) | AFM | a=5.290(5.297)<br>c=4.430(4.481) | $7 \times 7 \times 7$ | $5s^2 5p^2$ |
| FeSb | P63/mmc(194) | AFM | a=3.980(4.060)<br>c=5.028(5.130) | $15 \times 15 \times 15$ | $5s^2 5p^3$ |
| $Fe_{1.12}Te$ | P4/nmm(129) | AFM | a=3.679(3.812)<br>c=6.505(6.251) | $5 \times 5 \times 3$ | $5s^2 5p^4$ |
| $FeI_2$ | P-3m1(164) | AFM | a=4.015(4.040)<br>c=7.108(7.375) | $7 \times 7 \times 5$ | $5s^2 5p^5$ |
| Xe | Free atom | NM | a=12 | $1 \times 1 \times 1$ | $5s^2 5p^6$ |

We would like to note that Grindy *et al.* have discussed diatomic energy correction for improving the DFT calculated formation energies of oxides, nitrides, hydrides, fluorides and chlorides formation with reference to experimental results[130]. We consider this corrections in our work for solutes like H, N, F and Cl but the resultant formation energies for $H_2$ appear to deviate more from experiment than without correction. Therefore, the diatomic correction schemes are not considered in this work.

For noble gas atoms, the spin polarized electronic energy of their free atoms have been used as their reference state energy. These free atom calculations were performed by placing a single atom at the center of a 12 Å cubic cell.

Spin polarized calculations were performed for all the crystalline systems with ferromagnetic or antiferromagnetic order. For FeO, FeS, $Fe_2Ti$, $Fe_2As$, $Fe_2Nb$, FeSn, FeSb, and $Fe_{1.12}Te$, antiferromagnetic calculations have been performed in accordance with their respective literature[**131–138**]. For Cr, commensurate antiferromagnetic spin structure has been assumed[**139**]. Specifying the AFM unit cell of $FeI_2$ in the DFT calculation is not straightforward. Therefore, calculation was performed with the $FeCl_2$-type AFM order[**140**]. For Mn, a nonmagnetic calculation in the bcc structure with 58 atoms ($\alpha$-Mn) was performed. The total energy of Mn was then corrected by 28 meV, the energy by which its antiferromagnetic state is reported to be more stable than the nonmagnetic state[**96**].

Further, the second phases are not always line compounds. $FeBe_2$, FeO, $Fe_3Al$, FeS, $Fe_2Ti$, FeV, FeCo, $Fe_3Zn_{10}$, $Fe_3Ga$, $Fe_3Ge$, $Fe_2Zr$, $Fe_2Nb$, FeTc, FeRh, FePd, FeSb, and $Fe_{1.12}Te$ all exhibit significant homogeneity range. Some of them also have complex magnetic structure and multiple or partial site occupancies. Total energies of these phases were computed for the crystallographic details given in the literature[**123, 124**]. Determining the minimum energy composition of these phases over their respective homogeneity range is beyond the scope of this work.

## 3.3 Results and discussion

### 3.3.1 Solute formation energies

Solute formation energies are useful to understand solid state solubility and alloying behavior. In Table 3.2, we have collected the results of our computations of solute formation energy ($E_f^X$) in bcc iron for solutes with atomic numbers 1 to 54 along with their size factors (SF(X)) and magnetic moments ($\mu_B$). For comparison, Table 3.2 includes also results from literature, within parentheses, wherever available. We first examine the solute formation energies, $E_f^X$.

We would like to emphasize a point here: It is a common practice in DFT calculations of formation energy of solute atoms in iron to choose the perfect crystal of the solute element as the reference system[**53, 96, 104, 126**]. But this choice is pertinent only if the pure solute element is actually the second phase existing in equilibrium with the solid solution phase.

**Table 3.2:** *Formation energies $E_f^X$ of solute atoms (X), solute size factor SF(X), and magnetic moment of solute X $\mu_B$ in bcc iron. The energies are given in eV. For comparison, results from the literature are given within parentheses wherever available.*

| X | $E_f^X$ | SF(X) | $\mu_B$ |
|---|---|---|---|
| H | 0.194(0.21)[115] | -0.65 | -0.023(-0.05)[141] |
| He | 4.350(4.19)[142] | 0.104 | 0.010(0.05)[142] |
| Li | 0.982 | 0.075 | -0.078 |
| Be | 0.395 | -0.144 | -0.138 |
| B | 1.694 | -0.31 | -0.14 |
| C | 0.471 | -0.063 | -0.146(-0.24)[143] |
| N | 0.210 | -0.022 | -0.111(-0.14)[143] |
| O | 1.236(1.24)[104] | 0.176 | 0.044 |
| F | 0.75 | 0.377 | 0.17 |
| Ne | 5.706(5.76)[144] | 0.62 | 0.018 |
| Na | 3.435 | 0.63 | -0.04 |
| Mg | 0.971 | 0.466 | -0.053 |
| Al | -0.100 | 0.205 | -0.077 |
| Si | -0.160 | -0.021 | -0.089 |
| P | 0.460 | -0.095 | -0.054 |
| S | 0.760 | 0.068 | 0.02 |
| Cl | 2.546 | 0.603 | 0.138 |
| Ar | 7.819(8.03)[144] | 1.047 | 0.175 |
| K | 6.963 | 1.427 | 0.059 |
| Ca | 3.251 | 1.008 | -0.116 |
| Sc | 1.122 | 0.591 | -0.407(-0.25)[54] |
| Ti | 0.054 | 0.323(0.32)[53] | -0.797(-0.65)[53] |
| V | -0.286 | 0.223(0.15)[53] | -1.273(-1.21)[53] |
| Cr | -0.162(-0.14)[53] | 0.219(0.15)[53] | -1.803(-0.16)[53] |
| Mn | 0.182(0.21)[53] | 0.234(0.02)[53] | -2.015(-0.40)[53] |
| Co | -0.033 | 0.102(0.03)[53] | 1.699(1.72)[53] |
| Ni | 0.176 | 0.266(0.15)[53] | 0.890(0.88)[53] |
| Cu | 0.722(0.72)[53] | 0.211(0.15)[53] | 0.116(0.11)[53] |
| Zn | 0.353 | 0.319 | -0.085 |
| Ga | 0.138 | 0.331 | -0.182 |
| Ge | -0.086 | 0.301 | -0.121 |

Continued on next page

**Table 3.2 – continued from previous page**

| X | $E_f^X$ | SF(X) | $\mu_B$ |
|---|---|---|---|
| As | -0.271 | 0.286 | -0.070(-0.05)[145] |
| Se | 0.930 | 0.397 | -0.019 |
| Br | 2.738 | 0.719 | 0.064 |
| Kr | 8.158 | 1.165 | 0.194 |
| Rb | 7.928 | 1.623 | 0.05 |
| Sr | 4.884 | 1.473 | -0.075 |
| Y | 2.171 | 1.196 | -0.302(-0.20)[54] |
| Zr | 1.128 | 0.889(1.05)[53] | -0.715(-0.53)[53] |
| Nb | 0.231 | 0.679(0.79)[53] | -0.775(-0.70)[53] |
| Mo | 0.036 | 0.521(0.52)[53] | -0.804(-0.75)[53] |
| Tc | 0.084 | 0.436(0.48)[53] | -0.558(-0.52)[53] |
| Ru | 0.293(0.32)[53] | 0.426(0.40)[53] | 0.326(0.33)[53] |
| Rh | 0.062 | 0.542(0.58)[53] | 0.690(0.70)[53] |
| Pd | 0.483 | 0.732(0.81)[53] | 0.470(0.40)[53] |
| Ag | 1.802(1.93)[53] | 0.906(0.92)[53] | 0.106(0.01)[53] |
| Cd | 1.768(1.88)[96] | 0.921(0.95)[53] | -0.067(-0.06)[96] |
| In | 1.146(1.24)[104] | 0.935 | -0.234 |
| Sn | 0.62 | 0.895 | -0.201(-0.08)[145] |
| Sb | 0.261 | 0.837 | -0.092(-0.07)[145] |
| Te | 0.857 | 0.833 | -0.07 |
| I | 3.002 | 0.933 | -0.029 |
| Xe | 8.267(15.45)[146] | 1.405 | 0.132 |

This is indeed true for systems such as Fe-Li, Fe-Na, Fe-Mg, Fe-K, Fe-Ca, Fe-Mn, Fe-Cu, Fe-Rb, Fe-Sr, Fe-Ru, Fe-Ag, Fe-Cd and Fe-In[122]. But for systems such as, Fe-Be, Fe-B, Fe-C, Fe-N, Fe-O, Fe-Al, Fe-Si, Fe-P, Fe-S, Fe-Sc, Fe-Ti, Fe-V, Fe-Cr, Fe-Co, Fe-Ni, Fe-Zn, Fe-Ga, Fe-Ge, Fe-As, Fe-Se, Fe-Y, Fe-Zr, Fe-Nb, Fe-Mo, Fe-Tc, Fe-Rh, Fe-Pd, Fe-Sn, Fe-Sb, Fe-Te and Fe-I, second phases, other than the solute elements, exist[122]. For these systems, solute formation energies obtained using pure crystals as reference system can give unphysical equilibrium solubility[121]. For instance, the solute formation energies of Ti, V, Zr, Nb, Al, Si, P, Ga, Ge, and As from Olsson *et al.*[53], You *et al.*[104] and Murali *et al.*[126] give unphysically huge equilibrium concentration of these solutes. Regarding the estimation of the equilibrium concentration of solutes, please see Eq. 1 in Ravi *et* *al.*[121] and Eq. 6 in Murali *et al.*[126] and their discussion. Therefore, in our work, we have obtained the formation energies of solute atoms with respect to the second phases wherever they are pertinent.

We have compared our formation energies of solutes with literature where the reference state used is the same as in our work. The literature data are often from computational methods. Experimental data of energetics of atomic defects in iron are generally scarce and a comparison of our results with experiments is made wherever possible. We see from column 2 in Table 3.2 that our solute formation energy of H (0.194 eV) is in good agreement with prior DFT result of 0.21 eV[115] and experimental result of 0.30 eV[147]. For He atoms, the agreement between our work and literature (4.35 eV vs. 4.19 eV[142] and 4.30 eV[148]) is again very good. For solutes O, Ne, Ar, Cr, Mn, Cu, Ru, Ag, Cd, and In also, our formation energies are in good agreement with literature (within 15%). Only for Xe, our formation energy deviates appreciably from literature. The difference is likely due to the approximate Lennard-Jones empirical potential used in the literature. Although formation energies of other solutes are reported in the literature, they generally correspond to elemental crystal reference states rather than the second phases. Therefore, they are not compared with our solution energies.

### 3.3.2 Solubility

In order to see whether our solute formation energies predict reasonable solid state solubility, we have computed the equilibrium percentage of the solute atoms $C_{eq}$ by using their formation energies ($E_f^X$) in the ideal solution expression for solubility $C_{eq} = \exp(-E_f^X/k_B T)$[121,126]. Here $k_B$ is the Boltzmann constant and T is temperature, set to 800 K. The results are listed in Table 3.3. Table 3.3 lists also the solubility read from phase diagrams[122]. It should be noted that accurate solubility can be expected if $E_f^X$ in the above expression is replaced by respective free formation energies(accounting to avoid the double counting of the mean field configurational entropy). Calculating the entropic contributions of electrons, phonons, magnons and configurational degrees of freedom of the solid solution and the second phases to obtain the free formation energy

**Table 3.3:** *Equilibrium percentage of solutes* ($C_{eq}$) *in bcc iron obtained from our formation energies listed in Table 3.2 compared with corresponding concentrations from ASM alloy phase diagrams (PD) database[122]* ($C_{eq}$(PD)).

| X | $C_{eq}$ | $C_{eq}$(PD) | X | $C_{eq}$ | $C_{eq}$(PD) | X | $C_{eq}$ | $C_{eq}$(PD) |
|---|---|---|---|---|---|---|---|---|
| H | 0.060 | 0.05 | K | 0.000 | 0.00 | Sr | 0.000 | |
| He | 0.000 | | Ca | 0.000 | 0.00 | Y | 0.000 | 0.00 |
| Li | 0.000 | 0.00 | Sc | 0.000 | 0.00 | Zr | 0.000 | 0.00 |
| Be | 0.003 | 1.00 | Ti | 0.450 | 0.70 | Nb | 0.040 | 0.00 |
| B | 0.000 | 0.00 | V | 57.600 | 25.00 | Mo | 0.600 | 1.00 |
| C | 0.001 | 0.00 | Cr | 11.000 | 15.00 | Tc | 0.295 | 0.00 |
| N | 0.050 | 0.20 | Mn | 0.080 | 2.50 | Ru | 0.014 | 2.00 |
| O | 0.000 | 0.00 | Co | 1.610 | 30.00 | Rh | 0.410 | 8.00 |
| F | 0.000 | | Ni | 0.080 | 5.80 | Pd | 0.001 | 0.05 |
| Ne | 0.000 | | Cu | 0.000 | 0.00 | Ag | 0.000 | 0.00 |
| Na | 0.000 | 0.00 | Zn | 0.006 | 5.00 | Cd | 0.000 | 0.00 |
| Mg | 0.000 | 0.00 | Ga | 0.140 | 15.00 | In | 0.000 | 0.00 |
| Al | 4.260 | 20.00 | Ge | 3.500 | 20.00 | Sn | 0.000 | 2.00 |
| Si | 10.100 | 28.00 | As | 49.40 | 5.00 | Sb | 0.023 | 2.00 |
| P | 0.001 | 0.05 | Se | 0.000 | 0.00 | Te | 0.000 | 1.50 |
| S | 0.000 | 0.00 | Br | 0.000 | | I | 0.000 | 0.00 |
| Cl | 0.000 | | Kr | 0.000 | | Xe | 0.000 | |
| Ar | 0.000 | | Rb | 0.000 | | | | |

for all the 53 Fe-X binary systems is beyond the scope of this work. In Table 3.3, solubility is left blank for systems for which phase diagrams are not available.

The important result from our calculation of solute formation energies computed with reference to the corresponding second phases, rather than with respect to pure crystals of solute elements, is that the unphysically huge solubility predicted for certain solutes is now avoided/corrected (Ti, V, Zr, Nb, Al, Si, P, Ga, Ge, As). We see further from Table 3.3 that, except for V, As, and Tc, the solubility predicted by our solute formation energies are generally an underestimation compared to those from phase diagrams. This is reasonable because our solubility formula assumes the infinite dilution limit (small solubility limit and negligible interaction between the solute atoms) and ignores entropic contributions to solution free formation energy[**121**, **126**]. Overestimation of solubility of V and Tc can be related to the fact that the corresponding second phases (FeV and FeTc) are the Frank-Kasper $\sigma$ phases which are difficult to model. We have used one of the likely site occupancies reported for the σ-FeCr phase[149] to model FeV and FeTc phases. The reason for overestimation of As solubility is not clear. We have performed total energy of $Fe_2As$ in its antiferromagnetic structure in accordance with literature[134]. Our calculated lattice parameters of $Fe_2As$ match with experimental values.

Figure 3.2 displays the formation energies of solute atoms ($E_f^X$) in bcc Fe. We see that

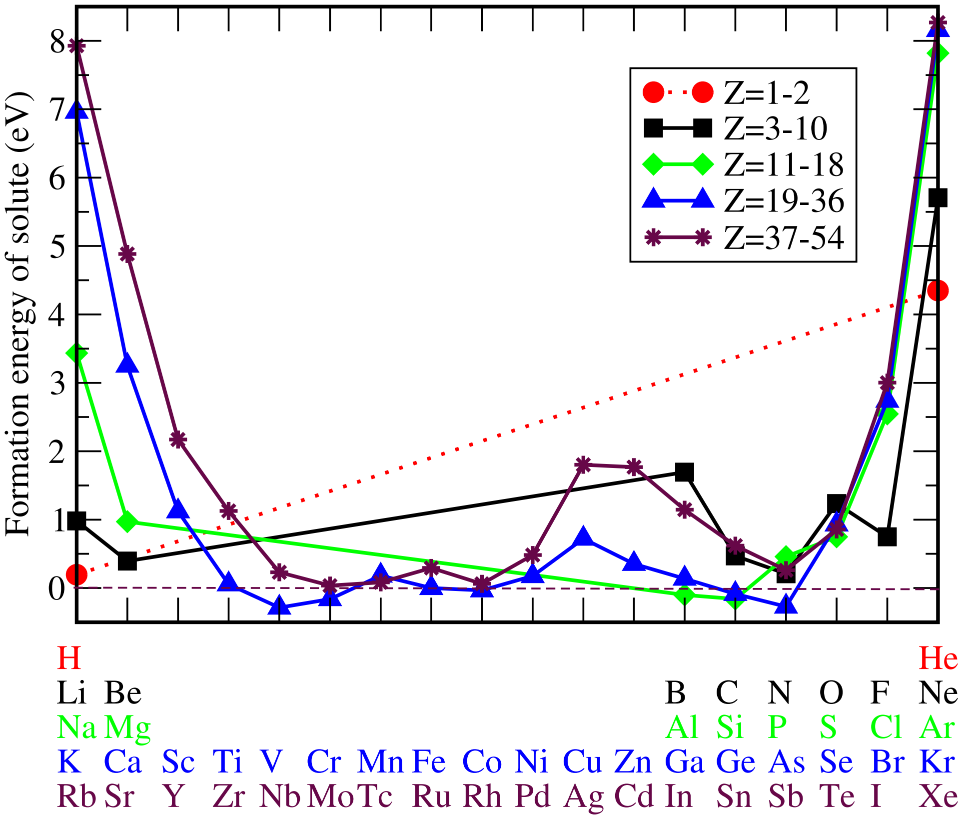

**Figure 3.2:** *Formation energies of solute atoms ($E_f^X$) in bcc Fe. The curves are guides to eye. The dashed horizontal line is a guide to eye delineating negative and positive formation energies.*

the formation energies of solute elements from fourth and fifth periods vary with their atomic numbers such that they reach maxima near the ends of the periods and minima in between, with a local hump near Cu and Ag (like a quasi-parabolic valley). Solutes from second and third periods show similar trend like the elements near the ends of the fourth and fifth periods. Solute formation energies of H and He are lowest in the respective groups. We see further that the substantially positive formation energies of alkali (Li, Na, K, Rb), noble gas (He, Ne, Ar, Kr, Xe), alkaline earth (Mg, Ca, Sr) and halogen (F, Cl, Br, I) atoms are in accord with their immiscibility in bcc iron[150]. Se, Ag and Cd too are immiscible in bcc iron[150]. In agreement with this, our calculation predicts an appreciably large endothermic formation energies for these solutes. For elements Al, Si, V, Cr, Co, Ge, and As, our calculations predict negative solute formation energies. This is in line with their large solid state solubility in Fe[150]. For other elements H, Be, B, C, N, O, P, S, Sc, Ti, Mn, Ni, Cu, Zn, Ga, Y, Zr, Nb, Mo, Tc, Ru, Rh, Pd, In, Sn, Sb and Te, our calculations predict moderately positive solute formation energies. Among these, solutes with appreciable solubility such as H, Be, N, P, Ti, Mn, Ni, Zn, Ga, Mo, Ru, Rh, Pd, Sn, Sb and Te have generally relatively lower formation energies than solutes with negligible solubility such as B, C, O, S, Sc, Cu, Y, Zr, Nb, Tc and In.

### 3.3.3 Size factors of solutes

The interaction among atomic defects in a host matrix can have different components. The solute formation energy, presented above, represents the chemical component which is usually the dominant component. The other component that is considered along with the chemical component is the strain component[50, 53, 96]. The strength of the interaction due to the strain component is to a first approximation proportional to the size factor of the solute atoms in the solvent matrix. Therefore, we computed the size factors of the solute atoms (SF(X)) in bcc Fe using Eq. 3.3, adopted from Hepburn *et al.*[96]. Column 3 of Table 3.2 lists these size factors. Comparison of size factors of 3d and 4d transition metal solute atoms from our work with literature[53] is generally satisfactory. For the other 37 solute atoms, size factors are not available in the computational literature and our work provides them for the first time. Measured size factors of substitutional elements are reported[151]. Qualitative agreement is seen between our calculated and the measured size factors, including the negative size factors for Be, P and Si, despite the significant difference in the solute concentrations involved. Following is the list of measured[151] size factors SF(X)/100: Al(0.128), Be(-0.262), Co(0.015), Cr(0.044), Cu(0.175), Ge(0.165), Mn(0.048), Mo(0.275), Nb(0.176), Ni(0.046), P(-0.132), Pd(0.622), Ru(0.199), Sb(0.364), Si(-0.079), Sn(0.677), Te(0.086), Ti(0.144), V(0.105), Zn(0.211).

Figure 3.3 displays the size factors of the solute atoms. We see that, like formation energies, the size factors of elements from fourth and fifth periods vary with their atomic numbers such that they reach maxima near the ends of the periods and broad minima in between, with a local hump near Ga and In. Size factors of solutes from second and third periods show similar trend like the solutes near the ends of the fourth and fifth periods. Size factors of H and He are lowest in their respective groups. Size factor of B deviates from this trend. We performed additional calculations of the solute formation energy and size factor of B considering it as an octahedral interstitial solute. While the formation energy is found to be almost same (slightly lower) as that of substitutional B, size factor is changed significantly (−0.009 for −0.31). With this size factor, the deviation of B is thus corrected. But this change in size factor is not useful to improve the correlations considered in the later sections. Therefore, we proceed with substitutional B.

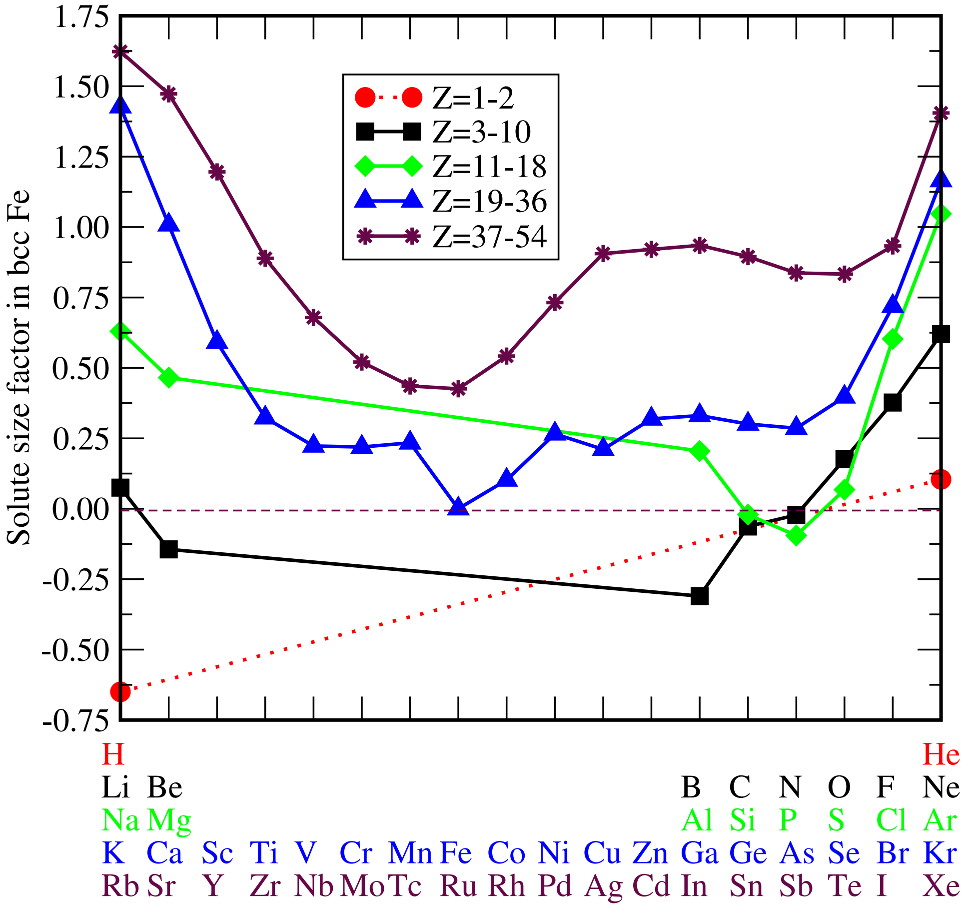

**Figure 3.3:** *Size factors of solute atoms [SF(X)] in bcc Fe. The curves are guides to eye.*

It is further evident that majority of solute atoms have positive size factors. That is, the effective size of these solute atoms in iron matrix is larger than that of iron atoms. This is in agreement with the increase in the lattice parameter of bcc iron with the addition of 3d solute elements[**107**]. Further, the elements that are identified to be immiscible according to their solute formation energies (He, Li, B, C, O, F, Ne, Na, Mg, S, Cl, Ar, K, Ca, Sc, Cu, Se, Br, Kr, Rb, Sr, Y, Zr, Pd, Ag, Cd, In, Sn, Sb, Te, I, Xe) also generally have relatively large size factors. He, Li, C, and S are exceptions. These elements are immiscible in iron despite their relatively small size factors. Al, Ti, V, Cr, Mn, Ni, Zn, Ga, Ge, As, Nb, Mo, Ru and Rh form another set of exceptions. These elements exhibit appreciable solubility though their size factors are relatively large.

### 3.3.4 Magnetic moments of solutes

Knowledge of magnetic moments of solute elements in iron will be useful for selecting alloying additions with desired magnetic properties. Therefore we have collected the local magnetic moments of all solute atoms considered in this work. Our calculated magnetic moments of solutes ($\mu_B$, Bohr magnetron) are listed in column 4 of Table 3.2. For 3d and 4d transition metal elements as well as for H, He, C, N, Sc, As, Y, Sn, and Sb, our calculated local magnetic moments are found to be in good agreement with literature[**53**, **54**, **96**, **141–143**, **145**]. For other solute elements our work provides their magnetic moments for the first time. Figure 3.4 displays the magnetic moments of solutes in bcc iron. We see that the local magnetic moments are not quite significant for solutes from first, second and third periods (Z=1 to 18). Solutes from fourth and fifth periods (Z=19 to 36 and Z=37 to 54) have similar magnetic coupling with host Fe. The 3d and 4d transition metal solutes to the left of Fe in the periodic table show antiferromagnetic coupling while those to the right of Fe show ferromagnetic coupling with host Fe[**152**]. Magnetic moments of 3d solutes are relatively stronger than those of 4d solutes. Further it is found that the impurity moments of Ti, V, Cr, Mn, Co, Ni, and Cu obtained from our calculations are in good agreement with neutron scattering experiments and first principles calculations[**152**]. Rahman *et al.* have given a mechanism for the antiferromagnetic and ferromagnetic coupling of solute moments with the host moment for 3d transition metal atoms[**107**]. Through comparison of the spin-unpolarized and polarized impurity-site-projected local density of states (as well as spin density contour plots), they have shown that all 3d electrons from Sc to Cr impurities occupy local minority spin bands (minority spin $e_g$ states) to achieve charge neutrality and consequently to align antiferromagnetically to the host magnetic moments. Additional 3d electrons (from Co, Ni, Cu, Zn impurities) are forced to enter the $t_{2g}$ majority spin states and couple ferromagnetically to the host Fe atoms[**107**]. While this trend appears to hold for other elements on the left side of the respective periods, it does not hold for solutes on the right side. Rather, solutes from Mg to Ar, Zn to Kr, and Cd to Xe appear to form another group of elements with magnetic coupling similar to 3d or 4d elements with Fe though with weaker moments.

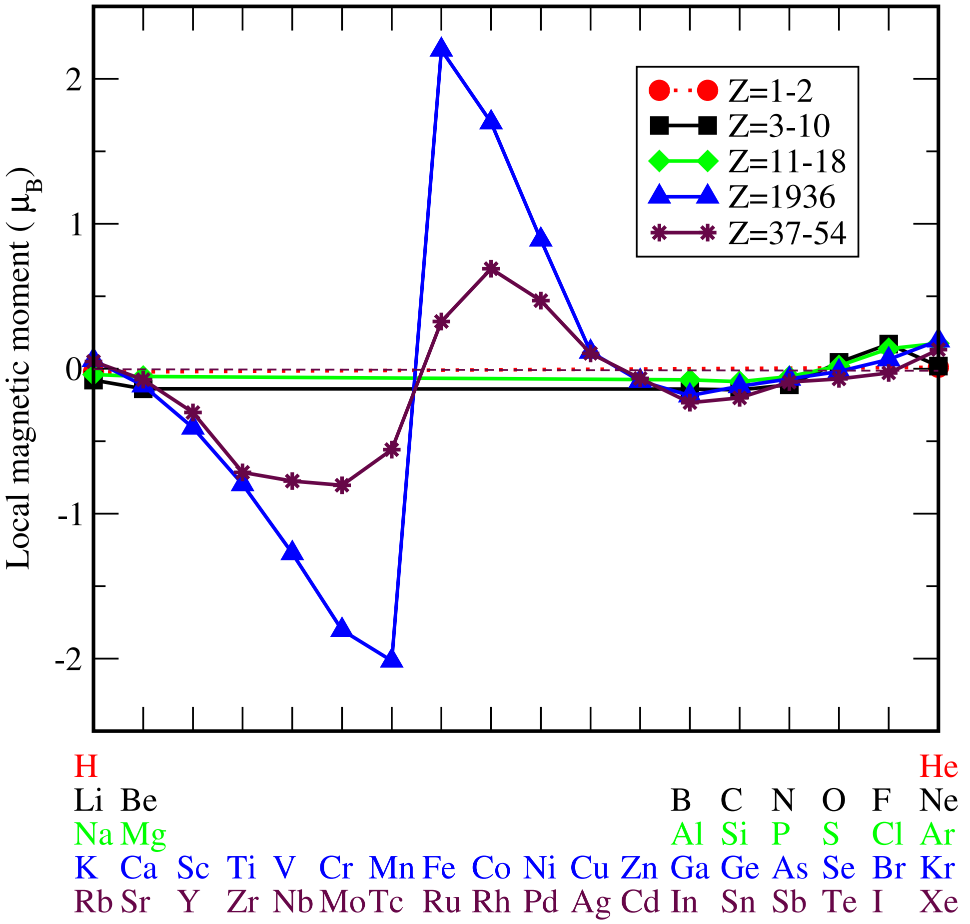

**Figure 3.4:** *Local magnetic moments of solute atoms ($\mu_B$) in bcc Fe. The curves are guides to eye.*

### 3.3.5 Correlation between solute formation energies and size factors

To see whether the size factor of solutes affects its formation energy, we have plotted solute formation energy as a function of their size factor in bcc iron, which is shown in Fig. 3.5. The horizontal dotted line at the solute formation energy of 1 eV is a guide to eye separating data points below and above 1 eV. The vertical dotted line at size factor 1 separates data points below and above 1. The solute atoms that form alloys with iron generally have size factor below 1 and formation energies below 1 eV whereas elements that do not normally alloy with iron (Li, Na, K, Rb, He, Ne, Ar, Kr, Xe, F, Cl, Br, I, Mg, Ca, Sr, Ag, Cd, In, and Y) [**150**] generally have solute formation energies above 1 eV. Many of the later also have size factors above 1. That is, a correlation between solute formation energies and size factors exist for some elements but is absent for other elements. For example, the size factor of solutes He, Li, S, and Co are near 0.1. But their formation energies change from about 4 eV to about −0.003 eV.

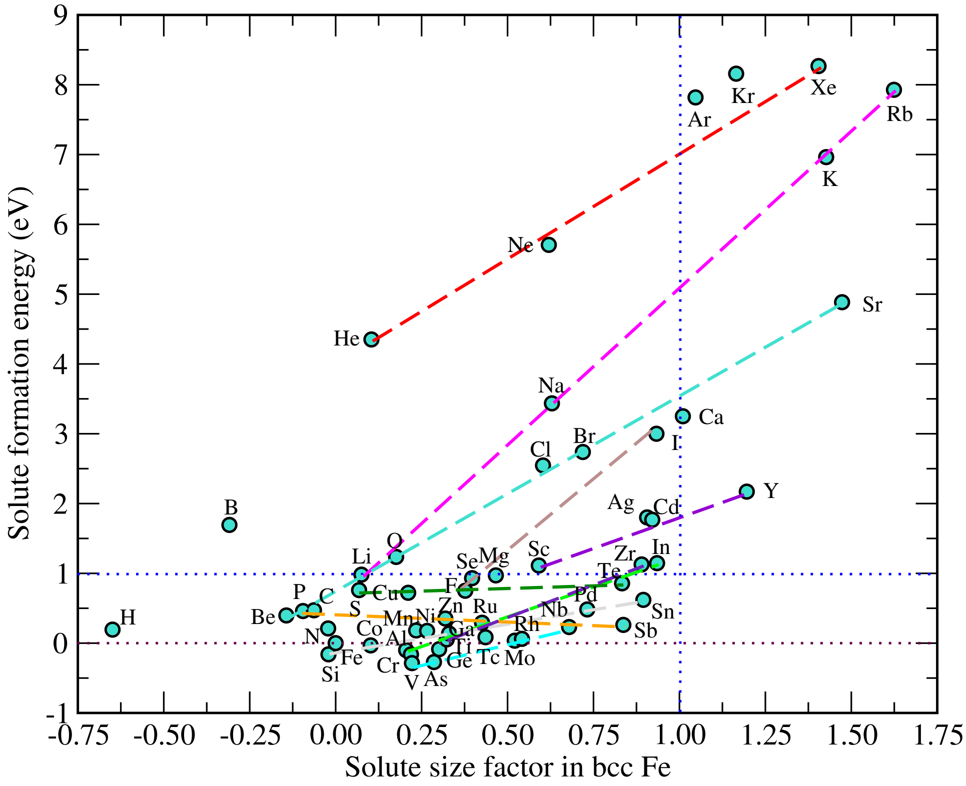

**Figure 3.5:** *Formation energy vs size factor of solute [$E_f^X$ vs SF(X)] atoms in bcc Fe. The dashed lines are guides to eye indicating a correlation between the formation energy and the size factor of solute atoms along columns in the periodic table. Note that we have drawn only a few lines to illustrate this correlation though it exists along other groups as well.*

Other trends also emerge from Fig. 3.5. By comparing isoelectronic sets of solutes (i.e., solutes in the same column or group of the periodic table, H/Li/Na/K/Rb, Be/Mg/Ca/Sr, Sc/Y, Ti/Zr, V/Nb, Cr/Mo, Mn/Tc, Fe/Ru, Co/Rh, Ni/Pd, Cu/Ag, Zn/Cd, B/Al/Ga/In, C/Si/Ge/Sn, N/P/As/Sb, O/S/Se/Te, F/Cl/Br/I, He/Ne/Ar/Kr/Xe), one can see a clear trend that the size factor increases down the group with an associated increase in the solute formation energy, indicated by dashed lines drawn as a guide to the eye. Solutes H, B, C, N, and O are exception to this trend. This graph shows that the solute size factor and its influence on the solute formation energy are quite appreciable along the group rather than across the periods. Another physical trend that may be noticed is that the rate of increase of solute formation energy with the size factor is less along V/Nb, Cr/Mo, Mn/Tc, Co/Rh, and Ni/Pd groups compared to alkali, alkaline earth, halogen, and noble gas atoms. The higher rate of increase of solute formation energies with size factor, for instance, for alkali elements or noble gas atoms, is likely because the strain component (size factor) of the interaction is more dominant than the chemical component. This also indicates, for instance, that the solubility of He in iron will increase appreciably with high pressure compared to the solubility of Nb or Mo.

## 3.4 Conclusions

In order to understand the atomic level properties of steels, we have performed an extensive set of first principles electronic structure calculations of the formation energies of atomic defects in ferromagnetic bcc iron. An extended set of solute elements with atomic numbers from 1 to 54 have been considered. Our calculations reveal several trends in the formation energies of solutes and their size factors. (1) It is found that the formation energies of solutes from fourth and fifth periods vary with their atomic numbers such that they reach maximum near the ends of the periods and minimum in between, with a local hump near Cu and Ag (like a quasi-parabolic valley). Solutes from second and third periods show similar trends like the elements near the ends of the fourth and fifth periods. The common solute additions to Fe (3d, 4d, sp elements) are found to possess moderate formation energies. Large endothermic formation energies are obtained for solutes that lack solubility in Fe (alkali, halogen, noble gas, alkaline earth, Se, Ag, and Cd atoms). (2) Like formation energies, the size factors of the solute elements also vary with their atomic numbers such that they reach maximum near the ends of the periods and minimum in between. The majority of the solute atoms have positive size factors, i.e., their effective sizes in the iron matrix are higher than that of iron atoms. Immiscible solute atoms generally possess relatively large size factors. (3) The size factors of isoelectronic sets of elements increase down the groups with an associated increase of the formation energies. (4) Solubilities estimated from our formation energies are found to be in reasonable agreement with those from phase diagram database.

# 4

# Binding energies of atomic defects in bcc ferromagnetic iron

## 4.1 Introduction

In an alloy, solute atoms can move randomly in all directions. When they encounter one another, the interaction can be attractive or repulsive which would cause either precipitation or segregation. Therefore, it is useful to obtain the binding energies of pairs of solute atoms in iron. As stated in the previous chapter section 3.1, first principles electronic structure calculations offer the most accurate means to develop an atomic level understanding of the interactions of solutes and point defects in solids. In this chapter, we describe our first principles study of the binding energies of solute-solute and vacancy-solute pairs in bcc iron.

## 4.2 Computational method

Creation of different point defects in bcc iron matrix for our modelling study have been described in Fig. 3.1 in the previous chapter. Substitutional solute-solute pair defects were formed by replacing a pair of nearest-neighbor Fe atoms with a pair of solute atoms. Substitutional vacancy-solute pairs were created by removing a Fe atom at a given site and replacing a Fe atom with a solute atom at a nearest-neighbor (1nn) or a next-nearest-neighbor (2nn) site. Interstitial solute-solute pairs were formed by placing them at nearest-neighbor or further neighbor interstitial sites. Vacancy-interstitial atom pairs were formed by removing a Fe atom at a given site and placing the solute at a nearest or next-nearest octahedral interstitial site. A similar procedure is followed for tetrahedral interstitial solute H.

The binding energy of substitutional solute-solute (X-X) pair configuration, $E_b^{x-x}$, is defined as

$$E_b^{x-x} = [E(Fe_{N-2}X_2) + E(Fe_N)] - 2[E(Fe_{N-1}X_1)] \tag{4.1}$$

where $E(Fe_{N-2}X_2)$ is the total energy of the iron supercell with N lattice sites containing a pair of substitutional solutes X and (N-2) Fe atoms. Similarly, the binding energies of pair of interstitial solutes is given by

$$E_b^{x-x} = [E(Fe_N X_2) + E(Fe_N)] - 2[E(Fe_N X_1)] \tag{4.2}$$

where $E(Fe_N X_2)$ is the total energy of the iron supercell with N lattice sites containing a pair of solutes at interstitial sites and N Fe atoms. $E(Fe_N X_1)$ is the total energy of the iron supercell of N lattice sites containing N Fe atoms and a solute X at an interstitial site.

For the vacancy-solute($\square - X$) interaction, the binding energy of a substitutional solute configuration is given by

$$E_b^{\square-x} = [E(Fe_{N-2}X_1\square_1) + E(Fe_N)] - [E(Fe_{N-1}X_1) + E(Fe_{N-1}\square_1)] \tag{4.3}$$

where $E(Fe_{N-2}X_1\square_1)$ is the total energy of the iron supercell of N lattice sites containing a substitutional solute X, a vacancy ($\square$) and (N-2) Fe atoms. For an interstitial solute, the vacancy-solute binding energy is given by

$$E_b^{\square-x} = [E(Fe_{N-1}X_1\square_1) + E(Fe_N)] - [E(Fe_N X_1) + E(Fe_{N-1}\square_1)] \tag{4.4}$$

where $E(Fe_{N-1}X_1\square_1)$ is the total energy of the iron supercell of N lattice sites containing a vacancy at a substitutional site, a solute at an interstitial site and $(N-1)$ Fe atoms. With these definitions, negative values of $E_b$ denote binding configurations. DFT calculations of the total energies have been performed in the same manner as in chapter 3 with the similar specifications.

## 4.3 Results and discussions

### 4.3.1 Solute-solute binding energies

The binding energies are a measure of strength of attractive or repulsive interaction. Generally, 1nn solute-solute interactions are dominant compared to further neighbor interactions for substitutional solutes[**53**, **104**]. Therefore, second and further neighbor solute-solute interaction energies for these solutes have been omitted in our calculations so as to reduce the demanding computational requirements. For interstitial solutes C, N, and O, we have considered their binding energies in seven different configurations. Column 2 of Table 4.1 lists nearest neighbor solute-solute binding energies ($E_b^{X-X}$) for all the solutes along with results from literature. For 15 solutes Li, Be, F, Na, Mg, Cl, K, Ca, Br, Kr, Rb, Sr, Cd, I, and Xe, solute-solute binding energies are not available in the literature and our work provides them for the first time. For the remaining 38 solute atoms, solute-solute binding energies are available in the literature. For 18 of these 38 solutes, our calculated binding energies are in good agreement with literature (within 15%). For the remaining 20 elements (He, B, C, N, O, Ne, Si, Sc, Mn, Ni, Ga, Y, Zr, Nb, Tc, Rh, Pd, Ag, In, Sn), the difference is more than 15%. Out of these 20 solutes, the literature for He-He and Sc-Sc pairs correspond to different configurations compared to our work. Our work considers a pair of substitutional He atoms whereas literature corresponds to a pair of interstitial He atoms[**144**]. Similarly, our Sc-Sc pair corresponds to substitutional Sc atoms in bcc iron matrix modeled with a $3 \times 3 \times 3$ supercell while literature corresponds to a pair of Sc atoms in a fixed free 22-atoms cluster based on bcc structure[**153**] studied using the Korringa-Kohn-Rostoker Green function method.

Next, we analyze the source of the discrepancy for the remaining 18 systems (B, C, N, O, Ne, Si, Mn, Ni, Ga, Y, Zr, Nb, Tc, Rh, Pd, Ag, In, Sn). For these systems, as well as for systems where the comparison is satisfactory, the difference between our work and literature is that we have performed the calculations using a 54-atoms supercell with zero-pressure condition using finer k-mesh ($8 \times 8 \times 8$) and higher plane wave energy cutoff (500 eV) but in the literature the calculations have been generally done using 128-atoms supercell with constant-volume condition using coarse k-mesh ($3 \times 3 \times 3$)

**Table 4.1:** *Binding energies of solute-solute,* $E_b^{x-x}$*, and vacancy(□) -solute,* $E_b^{\square-X}$*, pairs at nearest*(1nn) *and next nearest neighbour* (2nn) *positions in bcc iron. All the energies are in eV/defect pair. For comparison, results from the literature are given within parentheses wherever available.*

| X | $E_b^{X-X}$ | $E_b^{\square-X}$(1nn) | $E_b^{\square-X}$(2nn) |
|---|---|---|---|
| H | -0.026(-0.03)[154] | -0.565(-0.57)[115] | -0.094 |
| He | -1.140(-0.37)[144] | -0.784(-0.80)[148] | -0.573(-0.50)[148] |
| Li | -0.208 | -0.235 | -0.032 |
| Be | -0.085 | -0.134 | -0.158 |
| B | -0.127(-0.05)[118] | -0.236(-0.20)[118] | -0.382(-0.39)[118] |
| C | 0.672(0.94)[117] | -0.521(-0.41)[119] | -0.052(0.16)[119] |
| N | 0.882(1.19)[117] | -0.786(-0.74)[119] | -0.244(-0.17)[119] |
| O | 0.272(0.40)[18] | -1.535(-1.41)[119] | -0.945(-1.02)[119] |
| F | -0.821 | -1.11 | -1.24 |
| Ne | -1.464(-0.75)[144] | -1.118(-5.41)[144] | -0.396 |
| Na | -0.6 | -0.672 | -0.013 |
| Mg | -0.142 | -0.445 | 0.06 |
| Al | 0.087(0.09)[104] | -0.307(-0.31)[104] | 0.017(0.02)[104] |
| Si | 0.290(0.24)[104] | -0.292(-0.29)[104] | -0.118(-0.11)[104] |
| P | 0.209(0.21)[104] | -0.367(-0.37)[104] | -0.256(-0.25)[104] |
| S | -0.490(-0.51)[104] | -0.535(-0.53)[104] | -0.359(-0.34)[104] |
| Cl | -1.124 | -1.184 | -0.6 |
| Ar | -1.287(-1.25)[144] | -1.688(-5.83)[144] | -0.745 |
| K | -1.484 | -1.819 | -0.843 |
| Ca | -0.51 | -1.276 | -0.31 |
| Sc | 0.159(0.35)[153] | -0.641(-0.41)[54] | 0.171(0.10)[54] |
| Ti | 0.237(0.24)[53] | -0.236(-0.23)[53] | 0.188(0.18)[53] |
| V | 0.227(0.23)[53] | -0.052(-0.05)[53] | 0.102(0.09)[53] |
| Cr | 0.256(0.24)[53] | -0.043(-0.06)[53] | 0.001(-0.01)[53] |
| Mn | 0.035(-0.06)[53] | -0.192(-0.19)[53] | -0.096(-0.14)[53] |
| Co | 0.045(0.04)[53] | 0.031(0.03)[53] | -0.101(-0.11)[53] |
| Ni | -0.001(-0.02)[53] | -0.086(-0.12)[53] | -0.204(-0.21)[53] |
| Cu | -0.224(-0.25)[53] | -0.237(-0.27)[53] | -0.181(-0.16)[53] |
| Zn | -0.148(-0.14)[153] | -0.320(-0.33)[52] | -0.091 |
| Ga | 0.065(0.12)[104] | -0.382(-0.39)[104] | -0.080(-0.06)[104] |
| Ge | 0.270(0.28)[104] | -0.435(-0.44)[104] | -0.128(-0.15)[104] |

Continued on next page

**Table 4.1 – continued from previous page**

| X | $E_b^{X-X}$ | $E_b^{\square-X}$(1nn) | $E_b^{\square-X}$(2nn) |
|---|---|---|---|
| As | 0.283(0.29)[104] | -0.510(-0.52)[104] | -0.202(-0.22)[104] |
| Se | -0.121(-0.11)[104] | -0.636(-0.62)[104] | -0.281(-0.30)[104] |
| Br | -0.717 | -0.914 | -0.379 |
| Kr | -1.156 | -1.562 | -0.554 |
| R | -1.305 | -1.947 | -0.818 |
| Sr | -0.743 | -1.839 | -0.772 |
| Y | -0.097(0.20)[18] | -1.325(-0.78)[54] | -0.225(-0.02)[54] |
| Zr | 0.226(0.32)[53] | -0.699(-0.67)[53] | 0.121(0.06)[53] |
| Nb | 0.299(0.38)[53] | -0.331(-0.32)[53] | 0.192(0.13)[53] |
| Mo | 0.256(0.28)[53] | -0.144(-0.13)[53] | 0.153(0.10)[53] |
| Tc | 0.056(0.08)[53] | -0.100(-0.11)[53] | 0.080(0.02)[53] |
| Ru | 0.070(0.08)[53] | -0.077(-0.09)[53] | 0.018(-0.02)[53] |
| Rh | 0.124(0.16)[53] | -0.114(-0.12)[53] | -0.070(-0.07)[53] |
| Pd | -0.015(0.02)[53] | -0.232(-0.25)[53] | -0.160(-0.16)[53] |
| Ag | -0.403(-0.33)[53] | -0.448(-0.47)[53] | -0.201(-0.20)[53] |
| Cd | -0.366 | -0.6 | -0.141 |
| In | -0.110(-0.06)[104] | -0.646(-0.68)[104] | -0.071(-0.10)[104] |
| Sn | 0.285(0.39)[104] | -0.690(-0.71)[104] | -0.051(-0.09)[104] |
| Sb | 0.601(0.64)[104] | -0.675(-0.71)[104] | -0.095(-0.10)[104] |
| Te | 0.577(0.68)[104] | -0.746(-0.76)[104] | -0.138(-0.18)[104] |
| I | 0.181 | -0.865 | -0.234 |
| Xe | -0.611 | -1.24 | -0.433 |

and lower plane wave energy cutoff (300 to 350 eV)[18, 53, 104, 117, 118, 144]. In order to verify whether the discrepancy in the binding energies is due to the size of the supercell, we have performed additional calculations for the oversized alkali and noble gas atoms(Li, Na, K, Rb, He, Ne, Ar, Kr, Xe) as their elastic strain fields are expected to extend beyond the $3 \times 3 \times 3$ supercell. Y, Zr, Pd and B are also included in this calculation of supercell size convergence test. Table 4.2 lists these binding energies.

It is evident that for Li, Na, He, Ne and Ar pairs, the binding energies from 54-atoms supercell are converged to within about $\pm 0.1$ eV with those obtained from 128-, 250- and 343-atoms supercells. But for K, Rb, Kr and Xe pairs, this table indicates that one should use at least 128-atoms supercell to achieve similar convergence. Nevertheless,

**Table 4.2:** *Solute-solute binding energies ($E_b^{X-X}$) of selected solute pairs for four different supercell sizes (54, 128, 250, 343 atoms). Calculations with 128- 250- and 343-atoms supercells were performed with $6 \times 6 \times 6$, $3 \times 3 \times 3$ and $1 \times 1 \times 1$ k-points meshes respectively.*

| X-X | 54 | 128 | 250 | 343 |
|---|---|---|---|---|
| Li-Li | -0.208 | -0.193 | -0.197 | -0.228 |
| Na-Na | -0.681 | -0.650 | -0.628 | -0.678 |
| K-K | -1.486 | -1.333 | -1.280 | -1.220 |
| Rb-Rb | -1.309 | -1.056 | -1.020 | -1.026 |
| He-He | -1.183 | -1.172 | -1.174 | -1.138 |
| Ne-Ne | -1.463 | -1.500 | -1.485 | -1.477 |
| Ar-Ar | -1.285 | -1.216 | -1.161 | -1.158 |
| Kr-Kr | -1.155 | -1.000 | -0.895 | -0.858 |
| Xe-Xe | -0.611 | -0.365 | -0.355 | -0.341 |
| Y-Y | -0.097 | -0.101 | -0.045 | |
| Zr-Zr | 0.226 | 0.240 | 0.261 | |
| Pd-Pd | -0.016 | 0.017 | 0.032 | |
| B-B | -0.125 | -0.109 | -0.106 | |

the difference in the binding energies between 54- and 343-atoms supercell calculations is still less than 0.3 eV. For Y, Zr, Pd, and B pairs also similar convergence is seen. Further, the order of the alkali-alkali and noble gas-noble gas binding energies remain similar between results from 54- and 343-atoms supercells.

Next we consider the binding energies of interstitial solutes C, N and O. Since C, N and O are important interstitials in steel and since previous calculations of C-C and N-N binding energies have been generally performed at constant-volume and lower plane wave cutoff energy[117, 143], we have calculated these binding energies at zero-pressure condition. We have included all the seven configurations considered previously for the pair of interstitials[117] which are illustrated in Fig. 3.1. The results are listed in Table 4.3. We compare our binding energies of C-C, N-N and O-O pairs with the corresponding binding energies from literature. (The C-C and N-N interaction energies from literature are presented here without minus sign so as to be consistent with the convention used in this work.) For C-C pairs, our calculations predict repulsive interaction up to third neighbor separation and attractive interaction beyond this separation, unlike Domain *et al.* where the interaction is repulsive even at 6th neighbor

**Table 4.3:** *Binding energies ($E_b^{X-X}$), in eV, between pairs of C, N and O atoms. The calculations were done using 54-atoms supercell. The distances between the two solute atoms, d(X-X), are in units of the equilibrium lattice parameter (a). Configuration labels such as "5-6" means that the atoms are placed at sites labeled 5 and 6 in Fig. 3.1. For the C-C and N-N pairs, our binding energies are compared with Domain et al.[117], given in parenthesis. For O-O pair, literature value is from Jiang et al.[18].*

| Configuration | C-C | N-N | O-O | d(X-X) |
|---|---|---|---|---|
| 5-6 | 0.672(0.94) | 0.882(1.19) | 0.272(0.4) | $\sqrt{2}/2$ |
| 5-7 | 0.021(0.42) | 0.148(0.55) | -0.292 | $\sqrt{3}/2$ |
| 5-8 | 1.616(2.28) | 1.514(3.03) | 1.277 | 1 |
| 5.-9 | -0.206(0.17) | 0.028(0.27) | -0.402 | 1 |
| 5-10 | -0.120(0.14) | -0.029(0.28) | -0.028 | $\sqrt{5}/2$ |
| 5-11 | -0.226(0.20) | -0.150(0.29) | -0.244 | $\sqrt{2}$ |
| 5-12 | -0.247(0.09) | -0.294(0.12) | -0.301 | $\sqrt{3}$ |

separation. It may be noted that Bhadeshia has studied C-C interactions in iron[155]. One of the conclusions of this study is that the formation of stable clusters of carbon atoms in bcc Fe cannot be ruled out when the distance between pairs of carbon atoms is greater than the near neighbor separation. N-N pairs also show attractive interaction from fourth and farther neighbor separations unlike Domain *et al.* where the interaction is predicted to be repulsive up to 6th neighbor distances. In the case of O-O pair, our binding energy at nearest neighbor distance (0.272 eV) and that from literature (0.4 eV) [18] both suggest repulsive interaction. This interaction becomes attractive from second neighbor distance unlike C-C and N-N pairs where attractive interaction begins at fourth neighbor distance.

Thus, besides the nature of interactions, we see that the magnitude of our interaction energies also shows some difference with respect to literature. Since the interstitials are additional atoms in the iron matrix, they can be expected to have long ranged strain fields. Therefore, we repeated the C-C and N-N binding energy calculations with $4\times4\times4$ supercells for configuration "5-12" (see Fig. 3.1) as it is reported to be stable[117]. These calculations give binding energies of $-0.11$ eV and $-0.12$ eV respectively. The corresponding binding energies from Domain *et al.* obtained using $4 \times 4 \times 4$ supercell are $-0.16$ eV and $0.03$ eV respectively. This shows that the binding energies tend to converge with 4 × 4 × 4 supercell calculations. The remaining difference is likely due to the constant-volume condition and the lower plane wave cutoff energy ($\leq$ 290 eV) employed in their work.

Further, the large difference in binding energy of 5-8 and 5-9 configuration with the same separation, d (1 Å) can be understand as follow: Point defect induces a long-range perturbation of the host lattice, leading to an elastic interaction with other structural defects. Solute-solute interaction energy is obtained from the elastic and chemical interaction. In the literature[**156**], it is shown that beyond the second nearest-neighbor distance, the elastic strain energy alone is able capture the interaction energy properly. At closer distances the elastic strain energy and the total strain energy diverge with the chemical interaction between carbon atoms causing the interaction energy to become large and positive(repulsive interaction) while the elastic interaction alone prefers, at short distances, that the carbon atoms sit on top of one another. In both the 5-8 and 5-9 pairs, the two octahedral sites containing the foreign interstitial atoms are on top of each other at the same distance. But there is a presence of an Fe atom at the centre of 5-8 pair. Due to this Fe atom, the elastic interactions is more in the case of 5-8 pair relative to 5-9 pair[**117**].

Figure 4.1 depicts the solute-solute binding energies listed in column 2 of Table 4.1. We see that the binding energies show a similar but inverse variation with respect to the atomic numbers like the solute formation energies in Fig. 3.2. That is, strong binding energies occur for solute pairs at the ends of the periods and weak binding energies for pairs from the middle of the periods. Further, the relatively strong binding energies ($<-0.2$ eV) obtained for the alkali Li, Na, K, Rb, alkaline earth, Ca and Sr, halogen F, Cl and Br, noble gas elements He, Ne, Ar, Kr, Xe, and Cu, Ag, Cd and S atoms suggests that the driving force for their segregation rather than remaining in solution is quite high, which is in agreement with their immiscibility or limited solubility in bcc iron[**150**]. Molecular dynamics simulation of He clustering and bubble formation in bcc Fe has shown that isolated He atoms are highly mobile and they aggregate into clusters[**157**]. Our $E_b^{He-He}$ indeed suggests clustering of He atoms in Fe.

Our results of solute-solute binding energies further suggests that pairs of 3d and 4d

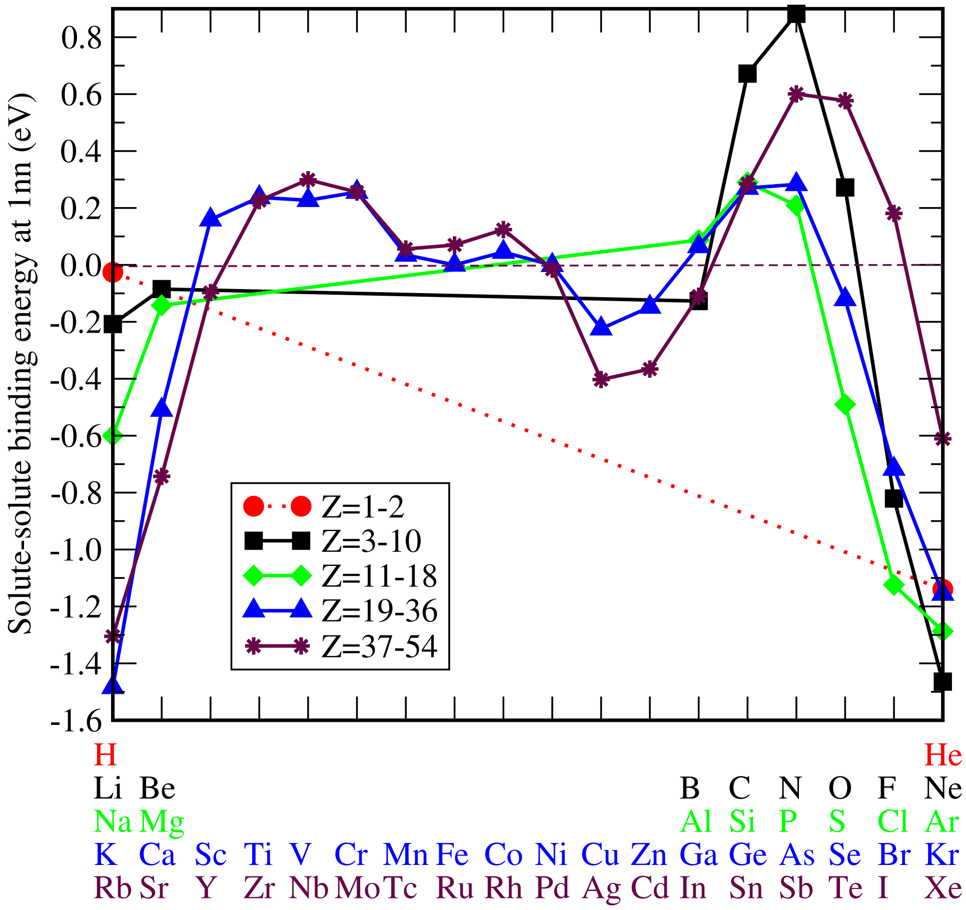

**Figure 4.1:** *Solute-solute binding energies ($E_b^{X-X}$) in bcc Fe at nearest-neighbour position (1nn). The curves are guides to eye.*

atoms from Ti to Ni and Zr to Pd show a tendency to repel each other while Cu, Zn, Ag and Cd have a tendency to cluster, in agreement with previous theoretical studies[**53**, **92**]. Among Al, Si, P, and S, S is less soluble in bcc Fe[**150**]. Accordingly, we obtain an attractive S-S binding energy while repulsive binding energies for Al, Si and P pairs. You *et al.* have predicted that S, Se, and In with attractive $E_b^{X-X}$ tend to phase separate. Al, Si, P, Ga, Ge, As, Sn, Sb, Te, with repulsive $E_b^{X-X}$ tend to be distributed uniformly in the matrix[**104**]. Our $E_b^{X-X}$ values confirm both the predictions. We also observe that $E_b^{X-X}$ are small for H, Be, Al, Mn, Co, Ni, Ga, Y, Tc, Ru and Pd. Several of these solutes (Al, Co, Ni, Ga) are known to form extended solid solution in bcc Fe.

### 4.3.2 Vacancy-solute binding energies

As mentioned earlier, vacancy-solute binding energy is one of the important factors controlling diffusion and solubility of solutes and hence clustering or nucleation of precipitates[50, 97, 158, 159]. In other words, diffusion coefficients of solute atoms depend on their binding energies with vacancies through migration energies[118, 120, 160, 161]. Vacancy-solute binding energies are also useful for modeling and predicting mechanical behavior of steels under irradiation[162]. Therefore we have computed the binding energies of vacancy-solute (□-X) pairs inserted in bcc Fe matrix at 1nn and 2nn positions. These energies are listed respectively in columns 3 and 4 in Table 4.1. There are reports of vacancy-solute interaction energies for 38 of the 53 solute atoms considered in this work[52–54, 104, 115, 118, 119, 144, 148]. For the other 15 solutes, i.e., Li, Na, K, Rb, Be, Mg, Ca, Sr, F, Cl, Br, I, Kr, Xe, and Cd, our work provides their binding energies for the first time. For H, Ne, Ar, and Zn, only 1nn pair $E_b^{\square-X}$ are available from literature. Our work provides both the 1nn and 2nn $E_b^{\square-X}$.

For C, N, and O, our computed $E_b^{\square-X}$ are in good agreement with Barouh *et al.*[119] as well as with experimental binding energy of −0.41 eV for □-C pair[163]. We find further that the binding of these interstitial solutes becomes stronger progressively from C to N to O (−0.521 eV, −0.786 eV, −1.535 eV) which is in agreement with Fu *et al.*[97]. For the other elements also, the comparison of $E_b^{\square-X}$ between our work and literature is quite satisfactory except for Ne, Ar, Sc, Co, Y and Pd.

We would like to note that for Al, Si, Ti, V, Cr, Mn, Co, Ni, Cu, Pd and Sb, $E_b^{\square-X}$ in bcc Fe are available from Muon Spin Rotation experiments (−0.185 to −0.400, −0.230, −0.160, <−0.105, <−0.105, −0.150, −0.140, −0.215, −0.140, −0.210, −0.455 eV respectively[164, 165]. A minus sign is included to these binding energies to make them consistent with the convention in our work). For these solutes, the comparison between our binding energies and experiments is very good except for Cu. Our calculation[52,53] overestimates $E_b^{\square-Cu}$ compared to measurements. We also note that experimental $E_b^{\square-X}$ is largest for Sb among the solutes listed above. Our computed $E_b^{\square-X}$ values reproduce this trend exactly. Among Si, P, Cr, Mn, Ni, and Cu, Messina *et al.* have shown that $E_b^{\square-X}$ is strongest for P and weakest for Cr[158]. Our results (Table 4.1) are in accord with this. Further, between Cr and Mo, the $E_b^{\square-X}$ is predicted to be relatively strong and attractive for Mo in agreement with Olsson *et al.*[53] and Garbatov et al[54]. These results are confirmed by a study of defects in iron-based binary alloys by Mossbauer and positron annihilation spectroscopies[166]. For Co and Ni, $E_b^{\square-X}$ from literature shows that their 2nn interaction is stronger than 1nn interaction[53, 158, 159]. Our binding energies reproduce this trend exactly.

Now consider binding energies of Ne, Ar, Sc, Co, Y, and Pd to vacancy where the comparison is less satisfactory. For Sc and Y, the discrepancy between our binding energy and literature[54] is possibly due to the Green function method with atomic sphere approximation used in their work which precludes relaxation of ionic coordinates. But the trend that $E_b^{\square-X}$ is strong for Y than for Sc is retained. For Ne and Ar, we have verified our binding energies with calculations using a 128-atoms supercell. Binding energies from these calculations ($-1.063$ and $-1.616$ eV respectively) are found to be in agreement with those obtained using a 54-atoms supercell. We think the discrepancy between our work and literature[144] for these solutes is due the lower plane wave cutoff energy (350 eV) and PW91, rather than PBE, exchange-correlation functional, and the constant volume condition used in their calculations.

Figures 4.2 and 4.3 show the binding energies of vacancy-solute pairs at 1nn and 2nn positions in bcc Fe respectively. We see that, like solute-solute binding energy in Fig. 4.1, binding energies of vacancy-solute pairs show an approximately inverse variation with respect to the atomic numbers of the solutes compared to the solute formation energies in Fig. 3.2. It is evident that both 1nn and 2nn $E_b^{\square-X}$ show similar variation with atomic numbers of the solutes. We also note that 1nn binding energies of elements from fifth periods are generally stronger than those of elements from fourth period, whereas the 2nn binding energies of 3d and sp elements from fourth period are generally stronger than those of corresponding elements from fifth period. We further see from Figs. 4.2 and 4.3 that the $E_b^{\square-X}$ at 1nn is attractive (exothermic) for all solutes except Co while the 2nn $E_b^{\square-X}$ have become repulsive (endothermic) for some solutes (Al, Mg, Sc, Ti, V, Cr, Zr, Nb, Mo, Tc, Ru).

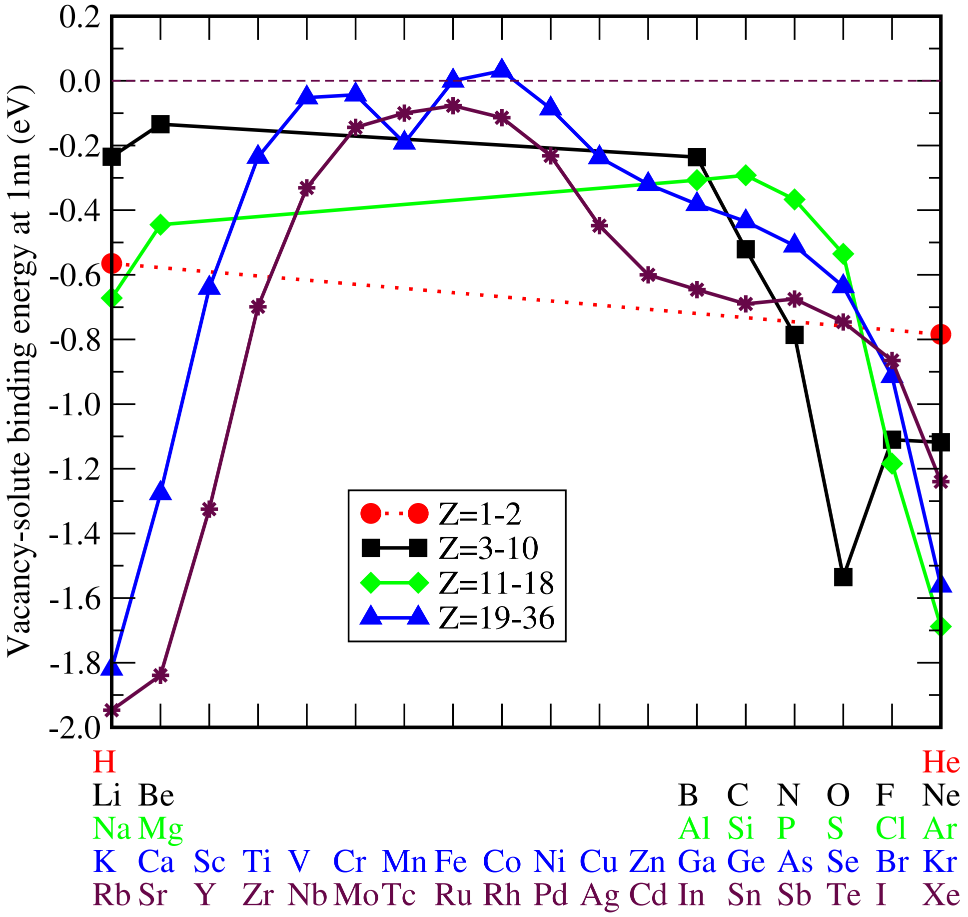

**Figure 4.2:** *Vacancy-solute binding energies ($E_b^{\square-X}$) in bcc Fe at nearest-neighbour positions (1nn).*

Comparison of Fig. 4.2 with 4.1 also shows that $E_b^{\square-X}$ at 1nn is attractive for all solutes unlike $E_b^{X-X}$ which are repulsive for many solute pairs.

Figure 4.3 shows that the 2nn $E_b^{\square-X}$ is repulsive for early transition metal solutes and attractive for late transition metal solutes in agreement with literature[53]. We see that the strongest vacancy-solute binding occurs for solutes K, Rb, Sr, Ar, Kr, Ca, O, Y, and Xe, and weakest binding for solutes V, Cr, Co, Ni, and Ru. This suggests that the solutes K, Rb, Sr, Ar, Kr, Ca, O, Y and Xe, when present in bcc Fe matrix, will trap vacancies strongly. This is known to be true for O and Y[97, 167].

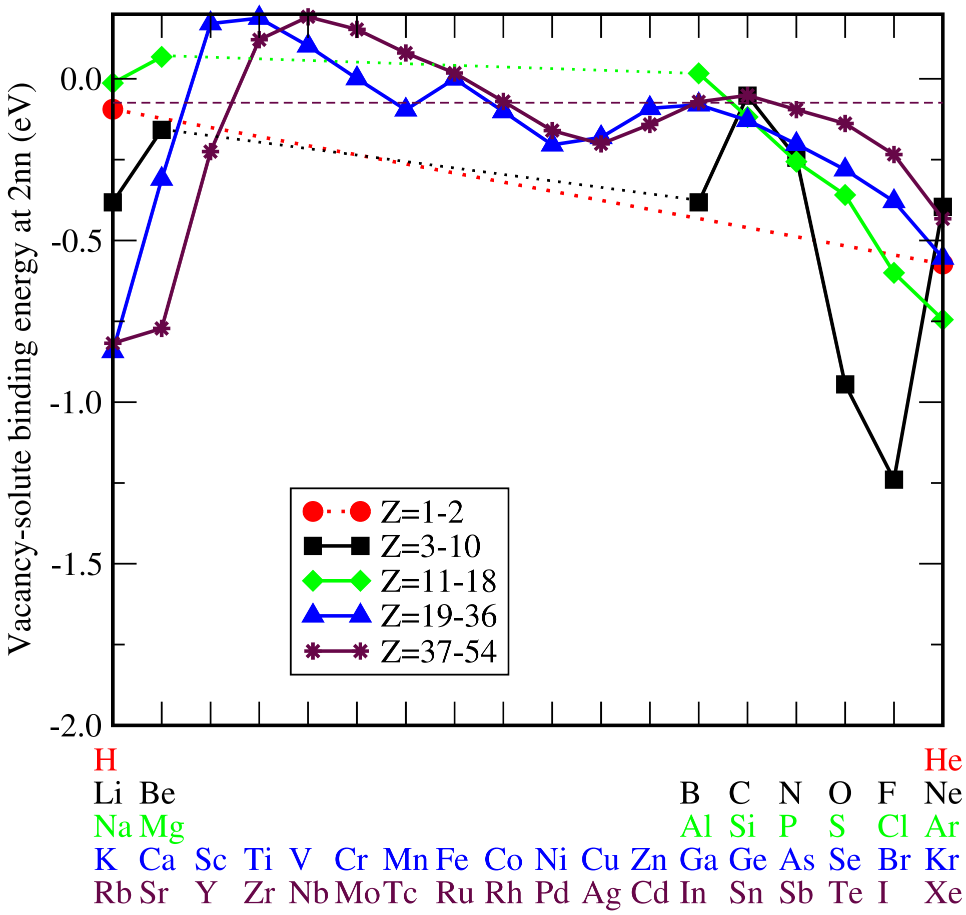

**Figure 4.3:** *Vacancy-solute binding energies ($E_b^{\square-X}$) in bcc Fe at next nearest-neighbour positions (2nn).*

Figure 4.4 is a graph of 1nn $E_b^{\square-X}$ for 3d and 4d transition metal atoms from our work plotted with respect to their corresponding calculated diffusion coefficients by Messina *et al.* [159]. It is interesting to note that our $E_b^{\square-X}$ of 4d solutes show an inverse parabolic variation to their calculated tracer diffusion coefficients at 1100 K[159] (see their Fig.9). For the 3d transition metal solutes also, similar correlation is evident. This observation suggests that $E_b^{\square-X}$ of other solutes predicted in our work would provide a guide to judge their diffusion coefficients.

Gorbatov *et al.* have earlier considered $E_b^{\square-X}$ and diffusion in iron. They have identified that the attractive 1nn $E_b^{\square-X}$ of most of the solutes correlate well with the experimental data on impurity diffusion coefficients, which are systematically higher than Fe self-diffusion coefficient[54]. Our $E_b^{\square-X}$ for an extended set of solute elements show that the attractive 1nn vacancy-solute interactions is generally retained. This appears to corroborate with the observation that in iron even the oversized solute atoms have higher diffusion coefficients than self-diffusion coefficient as well as with the suggested absence of slow diffusers among the common solute additions to bcc Fe[91, 167].

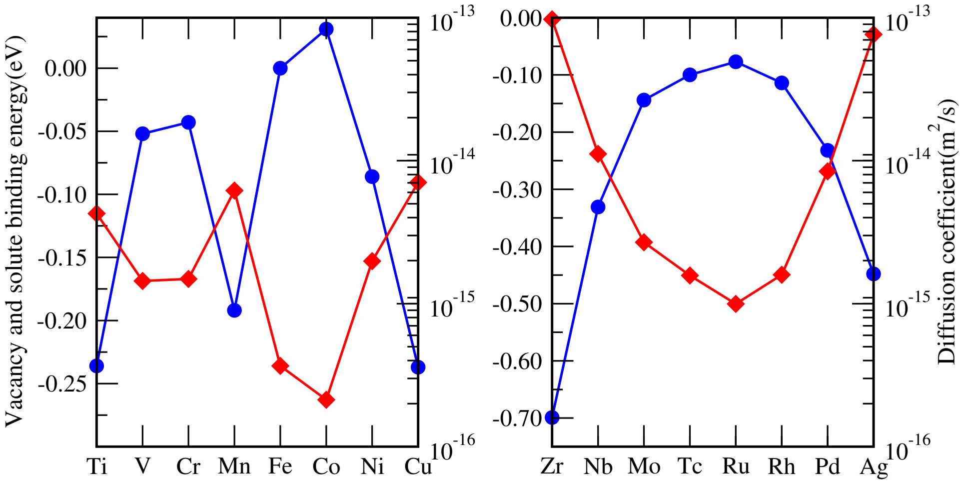

**Figure 4.4:** *Vacancy-solute binding energies of 3d and 4d transition metal atoms in bcc Fe at nearest-neighbour positions from our work plotted against the corresponding calculated diffusion coefficients from Messina et al.[159].*

### 4.3.3 Correlation between vacancy-solute binding energies and solute size factors

Figure 4.5 is a graph of vacancy-solute binding vs. solute size factor in bcc iron ($E_b^{\square-X}$ vs. SF(X)). The horizontal dotted line at $E_b^{\square-X}=-0.8$ eV is a guide to eye separating data points below and above −0.8 eV. It is evident that the common alloying elements in steel have their vacancy-solute binding energies above −0.8 eV and size factors within −0.25 and 1. The relatively weak vacancy-solute binding energies of thesesolute atoms are likely due to their strong bonding with the Fe atoms. Because of this strong X-Fe bonding, it is unfavorable for a solute atom to be placed near a vacancy, since this will result in fewer X-Fe bonds. The data points with binding energies below about −0.8 eV include solutes O, F, Ne, Cl, Ar, K, Ca, Br, Kr, Rb, Sr, Y, I, and Xe. Several of these solutes also have large size factors.

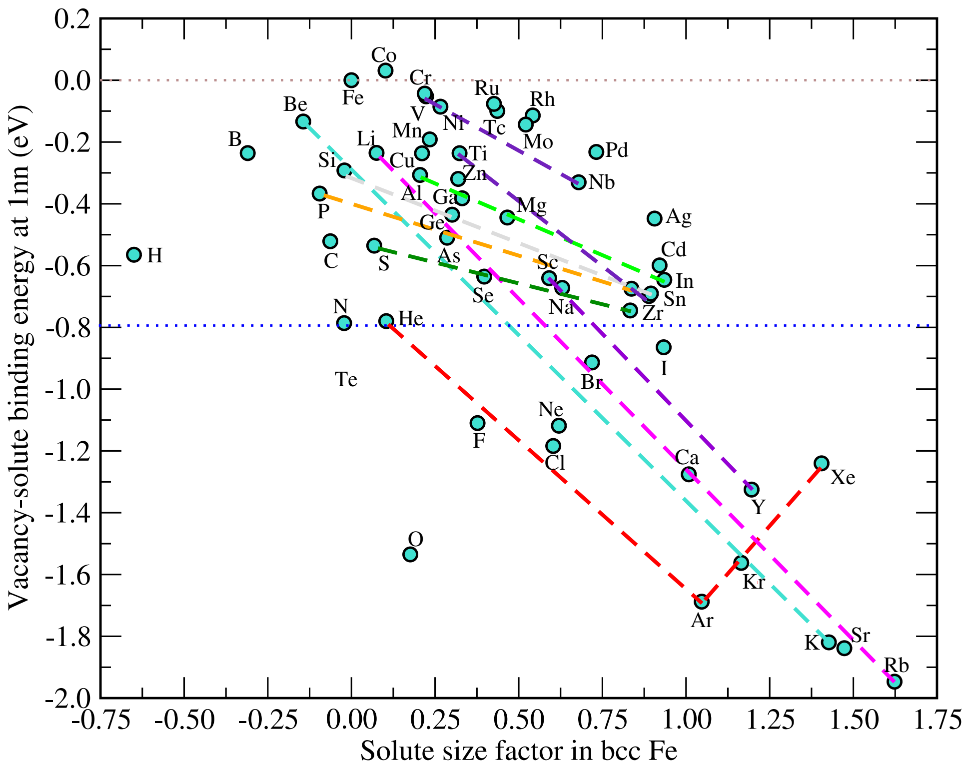

**Figure 4.5:** *Vacancy-solute binding energy vs solute size factor [$E_b^{\square-X}$ vs. SF(X)] in bcc Fe. The dashed lines indicate trends along the groups. Similar trends can be seen along the other groups also.*

The strong $E_b^{\square-X}$ with associated SF(X) seen for some of these solutes (Ar, Kr, Xe, K, Rb, Ca, Sr, Y), in an overall sense, may be understood by a simple physical argument: Placing large impurity atoms in the Fe matrix induces a significant strain on the surrounding Fe atoms. A vacancy next to this large impurity allows the impurity to relax towards the vacancy and hence away from the other neighboring Fe atoms. Thus, a vacancy in a 1nn position to a large impurity helps to relieve the strain, producing an energy lowering of the □-X pair, and hence a stronger binding energy. However, this mechanism is inadequate to explain the relatively small $E_b^{\square-X}$ of solutes with relatively large size factors such as Ag, Cd, In, Sn, Zr and Sb, and the large binding energies of O and F with relatively small size factors.

Figure 4.5 reveals other correlations as well. Isoelectronic sets of solutes (i.e., H/Li/Na/K/Rb, Be/Mg/Ca/Sr, Sc/Y, Ti/Zr, V/Nb, Cr/Mo, Mn/Tc, Fe/Ru, Co/Rh, Ni/Pd, Cu/Ag, Zn/Cd, B/Al/Ga/In, C/Si/Ge/Sn, N/P/As/Sb, O/S/Se/Te, F/Cl/Br/I, He/Ne/Ar/Kr/Xe) reveals a clear trend that the strength of vacancy-solute binding energies increases with increasing size factor down the columns, indicated by dashed lines. We see also that the rate of increase of vacancy-solute binding with size factor is less along V/Nb, Cr/Mo, Co/Rh and Ni/Pd groups. Solutes H, B, C, N, and O are exceptions. Mn/Tc, halogen and noble gas atoms (F, Cl, Br, I, He, Ne, Ar, Kr, Xe) also show deviations from this trend. For halogen and noble gas elements, $E_b^{\square-X}$ increases initially (from F to Cl, and from He to Ar) with the size factors and then decreases with further increase in the size factors (Cl to I, and Ar to Xe). This may be understood as follows: These atoms behave more like hard spheres in the iron matrix (unlike, for instance, alkali elements with a strong tendency to loose electrons). The size factors of F and Cl as well as He, Ne and Ar are relatively smaller that they can relieve their stresses by relaxing to the nearby vacancy site. But this is not effective for solutes with size factors beyond certain limit (Br and I as well as Kr and Xe) which manifests in the reduction of $\square - X$ binding. The deviation of Mn/Tc is likely due to the complex magnetic property of Mn which is missing from our DFT calculation. We will consider the vacancy-interstitial solutes interaction later.

### 4.3.4 Correlation between vacancy-solute binding energies and solute formation energies

Figure 4.6 is a graph of vacancy-solute binding energy versus solute formation energy ($E_b^{\square-X}$ versus $E_f^X$). The vertical and horizontal lines are guides to eye. It is apparent that $E_b^{\square-X}$ is correlated to $E_f^X$, similar to $E_b^{\square-X}$ vs. SF(X) (Fig. 4.5). It is further evident that most of the common alloying elements have their solute formation energies below 1 eV with vacancy-solute binding energies between 0.1 and $-0.8$ eV. Insoluble solute atoms with large formation energies such as He, Li, Ne, Na, Cl, Ar, K, Ca, Br, Kr, Rb, Sr, Y, Ag, Cd, In, I, and Xe have strong binding energy with vacancy. O and F are also insoluble in iron but their $E_f^X$ are moderate like those of common alloying elements. Nevertheless their binding energies with vacancy are strong like those of insoluble atoms. H, B, C, N, O, Mn/Tc, halogen and noble gas atoms are exceptions. We relate the deviations seen with the later elements to the same reasons discussed in the previous paragraph. The recurrent exceptions of interstitial solute atoms with respect to the several group-wise correlations considered above remains to be explained. On the other hand, experimental solution enthalpy and size factor of C in bcc Fe (solution enthalpy 0.60 to 0.78 eV and 1.10 eV as reported in Ref.[**106**, **120**] respectively, and size factor 0.781 as reported in Ref.[**168**]) leads to further deviation of C from the group-wise correlation (in Fig. 3.5). Comparison of experimental size factors of C, Si, Ge, Sn (0.781, -0.078, 0.165, 0.677)[**151**,**168**] also leads to similar conclusion. That is, the deviations of H, B, C, N and O from the group-wise trends is real. Thus our computed energetics of atomic defects in bcc Fe reveal several fundamental trends and will be useful for identifying solutes or combination of solutes with desired diffusion property that can be used to optimize the coarsening kinetics and creep strength of steels.

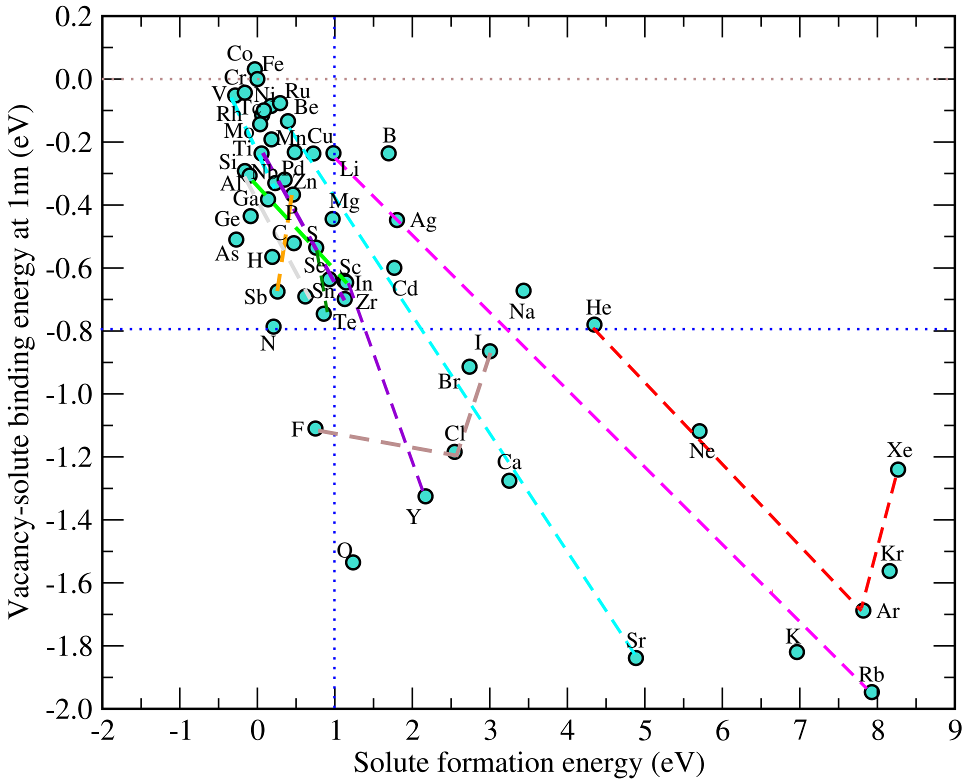

**Figure 4.6:** *Vacancy-solute binding energy versus solute formation energy ($E_b^{\square-X}$ vs. $E_f^X$) in bcc Fe. The dashed lines are drawn to indicate the correlations between $E_b^{\square-X}$ and $E_f^X$ along the groups.*

## 4.4 Conclusions

Our calculation of binding energies of atomic defects pairs (solute-solute and vacancy-solute pairs) in ferromagnetic bcc iron reveal the following trends. (1) The solute-solute and vacancy-solute binding energies vary with the atomic number of the solutes in a manner inverse to the formation energies and size factors. That is, strong binding energies occur for solute-solute or vacancy-solute pairs at the ends of the periods and weak binding energies for pairs from the middle of the periods. We also find that the 1nn solute-solute binding is repulsive for many solute pairs while vacancy-solute binding is always attractive. (2) The strength of the solute-solute and vacancy-solute binding energy increases with the size factors of solutes down the groups. (3) Comparison of our predicted vacancy-solute binding energies of 3d and 4d transition elements with their corresponding calculated diffusion coefficients from literature shows a significant correlation whereby solutes with strong binding energies possess higher diffusion coefficients and vice versa. This in turn indicates that our predicted vacancy-solute binding energies of other solutes are useful to estimate their diffusion coefficients.

# 5

# Stability of B1-type oxides in bcc iron

## 5.1 Introduction

Oxide Dispersion Strengthened advanced ferritic steels are studied for fuel clad and wrapper core components in fast spectrum reactors[24]. Oxide Dispersion Strengthened (ODS) ferritic steels have very good strength and resistance against irradiation damage, high temperature creep and corrosion. These steels are generally produced through mechanical alloying and subsequent extrusion or forging. The resistance of the ODS steels to degradation by high temperature and irradiation is attributed to the oxide nanoparticles dispersed in the steel matrix. These highly stable densely dispersed oxide nanoparticles obstruct the dislocation motion and grain boundary sliding leading to stable microstructure at elevated temperatures[9, 14–21]. Sustaining the superior performance of the steels in the severe reactor environment under long-term service is important for the efficient operation of the nuclear power plants[9].

Therefore, the characterization of these oxide nanoparticles in ODS steels have been an important research topic[19–21, 169–176]. A large number of transmission electron microscopy (TEM) studies have shown that most of these oxide nanoclusters in ODS steels with proper amounts of Y, Ti and O are near-stoichiometric $Y_2Ti_2O_7$ pyrochlore oxides[13]. Ribis *et al.* have studied the response of the nano-oxides in ODS steels to neutron and ion irradiation[174]. This work shows that irradiation cause an increase in size and a decrease in density of the $Y_2Ti_2O_7$ particles. Lu *et al.* have studied a 9Cr ODS steel using heavy ion irradiation and TEM to understand the relationship between its swelling resistance and the stability of the oxide dispersion. They have shown, in contrast, that the average size of the oxide particles decrease dramatically and their density increases sharply with irradiation damage. This work further shows that the oxide dispersion observed after irradiation has no distinct lattice structure and they are not $Y_2Ti_2O_7$, $Y_2TiO_5$, or $Y_2O_3$[175]. Thus, it is desirable to identify better dispersion capable of retaining/improving the strength and stability of the ODS steel. In view of this, Takahashi and Tanaka have studied the formation energy of 29 different $A_2B_2O_7$ pyrochlore-type oxides in bcc iron matrix and their influence on the bulk moduli of the iron matrix through first principles calculation and data mining[177]. They have predicted that $Y_2Zr_2O_7$ and $Y_2Ti_2O_7$ are good candidates as stable and suitable oxide dispersion for ODS steel.

On the other hand, Hirata *et al.* have shown that the oxide nanoclusters in ODS steel are defective TiO particles with NaCl (B1-type) structure[20]. The chemical composition and structure of the oxide dispersions have actually been a matter of debate[13]. Brandes *et al.* have reported that these fine oxide particles lack an identifiable crystal structure [169]. From atom probe tomography characterization of the chemistry of the nanoclusters in ODS steels, Boutard *et al.* have determined YO, TiO, and $O_2$ clusters with a mean composition of $YTiO_2$, unrelated to any stoichiometric compound[178]. These studies thus indicate that the B1-type TiO is also a potential candidate dispersion for ODS steel. This view is further supported by several studies on improving the properties of ODS steels where B1-type oxides (MgO, CaO, BaO, SrO) have been included in the investigation of their ability to trap He atoms in the iron matrix, influence on mechanical and micro-structural properties and resistance to irradiation[170–172]. Despite this, no study has directly investigated the stability of B1-type oxides in bcc iron.

Further, Siska *et al.* have studied the strengthening mechanisms of different oxide particles in 9Cr ODS steel at high temperatures[179]. Oono *et al.* have studied the precipitation of various oxides in ODS ferritic steels[180]. Dou *et al.* have studied the effects of Al, Zr, and Ti content on the crystal and metal-oxide interface structures of the oxide particles in several ODS steels by high resolution TEM for understanding the formation, transformation and irradiation tolerance of various kinds of oxide dispersions[176]. However, the list of oxides to be investigated as dispersion in ODS steels have not been well established.

In view of this, and in order to gain a comprehensive insight on the structure and stability of the B1-type oxide dispersions, we compute the formation energy of 31 different B1-type oxides in bcc iron and the bulk moduli of the oxide embedded iron matrix. We refer these B1-type oxides as MO oxides with M substituted by the 31 different elements. We show that oxides, such as TaO, MnO, AlO, SiO, ZrO, ScO, ZnO, MgO and SnO constitute stable oxides in the iron matrix, which tend to retain the bulk modulus of the iron matrix. Whereas, oxides, such as TiO, VO, CrO, FeO, CoO, NiO, MoO, RuO, RhO, HfO, WO, ReO, OsO, and IrO are chemically less stable in the iron matrix though the bulk modulus is retained. This chapter is organized as follows. After the introduction in Section 5.1, the computational scheme is outlined briefly in Section 5.2. In Section 5.3, we present the equilibrium structure of the embedded oxides, their formation energies, the bulk moduli of the oxide embedded bcc iron, and discuss the mechanism behind the exothermic or endothermic formation energies and the variation in the bulk moduli. Section 5.4 gives summary of the salient results.

## 5.2 Computational method

We model the B1-type oxides in iron by placing a $M_4O_4$ cluster in a 4×4×4 bcc Fe supercell with 128 sites. This $M_4O_4$ cluster is created by replacing 2 nearest neighbor Fe atoms with 2 M atoms each on two adjacent (110) planes and by placing an O atom at the nearest octahedral interstitial sites to each of the 4 M atoms. The pair of M atoms on the given (110) plane is rotated by 90° with respect to the other pair on the adjacent (110) plane. When these 4 M and 4 O atoms are linked, they form a simple tetragonal cell resembling the simple cubic cell with 4 Na and 4 Cl atoms placed alternatively at its corners constituting one eighth of the conventional B1-type NaCl unit cell. This is illustrated in Fig. 5.1. Thus the $M_4O_4$ unit is placed in the bcc Fe supercell such that the M's substitute Fe and O's occupy the associated octahedral interstitial sites in the same manner as all Cl atoms occupy the octahedral holes in the bcc Na to give the B1-type NaCl crystal structure. This work considers 31 different elements for M. Table 5.1

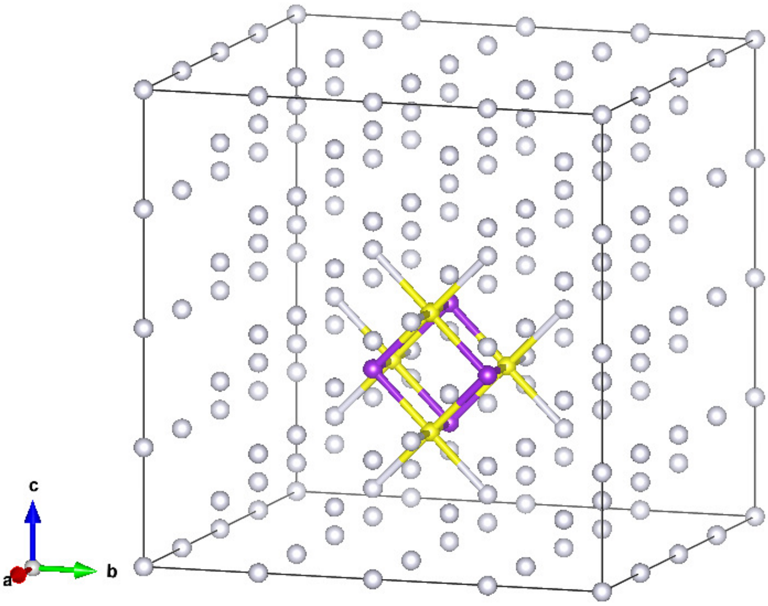

**Figure 5.1:** *Our supercell model of the B1-type MO oxide in bcc iron. It is created by placing a* $M_4O_4$ *oxide cluster in a 4×4×4 bcc Fe supercell. The* $M_4O_4$ *cluster is created by replacing 2 nearest neighbor Fe atoms with 2 M atoms each on 2 adjacent (110) planes and by placing an O atom at the nearest octahedral interstitial sites to each of the 4 M atoms. When these 4 M and 4 O atoms are linked, they form a simple tetragonal cell resembling the simple cubic cell with 4 Na and 4 Cl atoms placed alternatively at its corners constituting one eighth of the conventional NaCl (B1-type) unit cell. This work considers 31 different elements for M. M atoms are in blue and O atoms are in yellow colors.*

collects the crystallographic data of these MO oxides.

**Table 5.1:** *Crystallographic data of the MO oxides. For most oxides, the crystallographic information were taken from the online database SpringerMaterials[**124**]. The structural informations of ScO, YO, and ZrO were taken respectively from the ASM Alloy Phase Diagram Database, Kaminaga et al., and Nicholls et al.[**122, 181, 182**]. The angles $\alpha$, $\beta$, and $\gamma$ are given in degrees. In the last column, fu is abbreviation for formula units.*

| Oxide | Space group | a(Å) | b(Å) | c(Å) | $\alpha$ | $\beta$ | $\gamma$ | Volume(Å$^3$) |
|---|---|---|---|---|---|---|---|---|
| AlO | | | | | | | | |
| AuO | | | | | | | | |
| BaO | Fm-3m(225) | 5.52 | 5.52 | 5.52 | 90 | 90 | 90 | 168.5(4fu) |
| CaO | Fm-3m(225) | 4.81 | 4.81 | 4.81 | 90 | 90 | 90 | 111.2(4fu) |
| CdO | Fm-3m(225) | 4.69 | 4.69 | 4.69 | 90 | 90 | 90 | 103.5(4fu) |
| CoO | I4/mmm(139) | 3.01 | 3.01 | 4.25 | 90 | 90 | 90 | 38.6(2fu) |
| CrO | | | | | | | | |
| CuO | C1c1(9) | 4.69 | 3.43 | 5.14 | 90 | 99.54 | 90 | 81.5(4fu) |
| FeO | Fm-3m(225) | 4.30 | 4.30 | 4.30 | 90 | 90 | 90 | 79.5(4fu) |
| HeO | | | | | | | | |
| HfO | | | | | | | | |
| IrO | | | | | | | | |
| MgO | Fm-3m(225) | 4.21 | 4.21 | 4.21 | 90 | 90 | 90 | 74.8(4fu) |
| MnO | Fm-3m(225) | 4.44 | 4.44 | 4.44 | 90 | 90 | 90 | 87.8(4fu) |
| MoO | | | | | | | | |
| NbO | Pm-3m(221) | 4.21 | 4.21 | 4.21 | 90 | 90 | 90 | 74.6(3fu) |
| NiO | Fm-3m(225) | 4.18 | 4.18 | 4.18 | 90 | 90 | 90 | 73.1(4fu) |
| OsO | | | | | | | | |
| ReO | | | | | | | | |
| RhO | | | | | | | | |
| ScO | Fm-3m(225) | 4.45 | 4.45 | 4.45 | 90 | 90 | 90 | 88.1(4fu) |
| SiO | F-43m(216) | 5.45 | 5.45 | 5.45 | 90 | 90 | 90 | 161.9(4fu) |
| SnO | P4/nmm(129) | 3.80 | 3.80 | 4.84 | 90 | 90 | 90 | 69.9(2fu) |
| SrO | Fm-3m(225) | 5.14 | 5.14 | 5.14 | 90 | 90 | 90 | 135.8(4fu) |
| TaO | | | | | | | | |
| TiO | Fm-3m(225) | 4.18 | 4.18 | 4.18 | 90 | 90 | 90 | 73.3(4fu) |
| VO | Fm-3m(225) | 4.10 | 4.10 | 4.10 | 90 | 90 | 90 | 68.92(4fu) |
| WO | | | | | | | | |
| YO | Fm-3m(225) | 4.94 | 4.94 | 4.97 | 90 | 90 | 90 | 121.2(4fu) |
| ZnO | P63 mc(186) | 3.22 | 3.22 | 5.20 | 90 | 90 | 120 | 46.7(2fu) |
| ZrO | Fm-3m(225) | 4.62 | 4.62 | 4.62 | 90 | 90 | 90 | 98.6(4fu) |

The formation energy ($E_f$) of the $M_4O_4$ oxide in the bulk bcc iron is calculated from the following expression[177]:

$$E_f(M_4O_4) = E(Fe_{124}M_4O_4) - \frac{124}{128}E(Fe_{128}) - E(M_4O_4) \tag{5.1}$$

where E($Fe_{124}M_4O_4$) and E($Fe_{128}$) are respectively the total energies of the supercells containing the oxide cluster $M_4O_4$ and pure bcc Fe. E($M_4O_4$) is the total energy of the free $M_4O_4$ cluster. The formation energy in this work thus represents the energy related to dissolving $M_4O_4$ as a single entity in the bcc iron matrix. It is similar to the formation energy of elemental solutes in a crystal[183]. It does not represent dissolving $M_4O_4$ unit into elemental M's and O's in the iron matrix. Positive formation energy represents endothermic reaction of $M_4O_4$ with Fe matrix while negative formation energy represents exothermic reaction.

For the calculation of the total energies required in Eq. 5.1, we used the Vienna Ab initio Simulation Package[78, 80] which implements the density functional theory using pseudopotentials and plane waves. The Projected Augmented Wave (PAW) method was used for the electron-ion interaction[79, 86]. Perdew-Burke-Ernzerhof (PBE) approximation was used for the exchange and correlation interactions[71]. Spin polarized calculations were performed for all the systems considered in this work as bcc Fe is a ferromagnetic substance. Initial magnetic moments for M's were specified in accordance with their magnetic alignment in bcc Fe[183]. The Kohn-Sham orbitals were expanded in plane waves with cutoff energy of 450 eV. For all the bulk calculations, a $4\times4\times4$ special k-points mesh generated using the Monkhorst-Pack scheme was used to sample the Brillouin zone. All structural degrees of freedom, i.e., ionic coordinates, size and shape of the simulation cell, were allowed to relax in these calculations.

We note here that the convergence of the self consistent field (SCF) iteration have not been straightforward for several of the $Fe_{124}M_4O_4$ systems. For these cases, the total energy calculations were performed in several steps. First, with the given k-points mesh ($2 \times 2 \times 2$), plane wave kinetic energy cutoff (400 eV) and total energy convergence criterion $10^{-4}$ eV, the ionic positions were allowed to change with fixed cell shape and volume. Then, along with the ionic position, the cell shape was also allowed to change with the fixed cell volume. After this, all the structure degrees of freedom(ionic positions, cell shape and volume) were allowed to change, first at the cutoff of 400 eV then at 450 eV. Next, the total energy convergence criterion was increased gradually from $10^{-4}$ eV to $10^{-7}$ eV. Finally, the k-points mesh was increased from $2 \times 2 \times 2$ to

$3 \times 3 \times 3$ to $4 \times 4 \times 4$. We note further that, for some systems, the self consistent field iterations were unstable and did not converge when the cutoff was increased to 500 eV. Hence, the convergence with respect to cutoff was tested with systems where the SCF iteration were stable from 450 to 600 eV in steps of 50 eV. These calculations showed that the total energies were converged within 0.12 eV/$Fe_{124}M_4O_4$. Therefore, all the calculations have been performed with 450 eV cutoff energy.

The total energy of the free $M_4O_4$ clusters were calculated by placing them in a fixed 15 Å cubic box and solving their Kohn-Sham equations. For magnetic oxides, MnO, FeO, CoO, and NiO, spin polarized calculations were performed. These Γ k-point calculations allow relaxation of the positions of all the atoms. The free $M_4O_4$ clusters were initially made in the form of a cubic cell resembling the simple cubic cell with 4 M and 4 O atoms placed alternatively at its corners constituting one eighth of the conventional NaCl (B1) unit cell. Besides formation energies, we have also calculated the bulk modulus of the oxide embedded iron by fitting their E(V) data to the Vinet equation of state[184]. Both the oxide formation energies and bulk moduli of the oxide embedded iron are measures of the stability of ODS steel[177].

The bulk modulus,$B_0$, is defined as[185]

$$B_0 = -V_0 \left( \frac{\partial P}{\partial V} \right)_{(T, V_0)} \tag{5.2}$$

where V is the volume of the solid, P is an external pressure, $V_0$ is equilibrium volume at zero pressure, T is the temperature and the negative sign is used because the volume decreases when a positive external pressure is applied. The equilibrium volume at zero pressure $V_0$, bulk modulus $B_0$, and pressure derivative $B_0'$ of the bulk modulus $B_0$ were estimated by fitting our calculated E(V) data to the isothermal Vinet equation of state (EOS)[186]

$$P(V) = \frac{3B_0 x}{(1-x)^2} e^{\eta x} \tag{5.3}$$

where $x = 1 - \left(\frac{V}{V_0}\right)^{1/3}$ and $\eta = \frac{3}{2}(B_0' - 1)$. Integration with respect to volume, the Vinet

EOS yields an expression for the energy variation upon an isothermal volume change,

$$\Delta E(V) = -\int_{V_0}^{V} P(V)\, dV \tag{5.4}$$

$$E(V) = E(V_0) + \frac{9B_0V_0}{\eta^2}[1 + e^{\eta x}(\eta x - 1)] \tag{5.5}$$

## 5.3 Results and discussion

### 5.3.1 Structure of relaxed MO oxides in bcc iron matrix

Before analysing the structure of the $M_4O_4$ clusters placed in the iron matrix, we examined their relaxed structure without the iron matrix. It is found that most of the relaxed free $M_4O_4$ clusters remain intact as a single entity though distorted relative to the initial cubic form. The free $He_4O_4$ and $Os_4O_4$ clusters are not intact. The $He_4O_4$ cluster relaxes into two $O_2$ clusters and 4 isolated He atoms. The $Os_4O_4$ cluster relaxes to $Os_2O_4$ and two isolated Os atoms. Table 5.2 gives the calculated equilibrium bond lengths in each of the 31 $M_4O_4$ free clusters. First row gives the initial bond lengths which corresponds to the experimental values in B1-type TiO. We see that, in most cases, the calculated M-O, M-M, and O-O bond lengths are somewhat reduced relative to their respective experimental values wherever available. As noted above, the He-He relaxed bond length is significantly large compared to the initial M-M bond. For OsO, the listed bond lengths correspond to $Os_2O_4$ cluster.

In the initial cubic cluster, M-M and O-O bond lengths are same. Therefore, the difference between the M-M and O-O relaxed bond lengths are an indication of the distortion of the $M_4O_4$ clusters from the cubic form. Comparison of the differences between M-M and O-O bonds shows that majority of the O-O bonds are expanded relative to the M-M bonds.

Next we inspected the structure of all the $Fe_{124}M_4O_4$ systems. The positions of M, O and the surrounding Fe atoms and the associated bond lengths are found modified in the relaxed systems. Table 5.3 lists the relaxed bond lengths. For reference, initial bond lengths are listed in the first row of the table. The two bond lengths under the different category of bonds correspond to the first and second neighbor bonds. They are listed

**Table 5.2:** *Calculated equilibrium bond lengths in free* $M_4O_4$ *clusters. M-O, M-M and O-O bond lengths are listed. The last three columns give respective experimental bond lengths of oxides whose crystallographic data are given in Table 5.1. For reference, initial bond lengths in TiO are listed in the first row.*

| Oxide | M – O(Å) | M – M(Å) | O – O(Å) | M – O(Å) | M – M(Å) | O – O(Å) |
|---|---|---|---|---|---|---|
| MO | 2.09 | 2.96 | 2.96 | | | |
| AlO | 1.87 | 2.66 | 2.63 | | | |
| AuO | 2.24 | 3.01 | 3.33 | | | |
| BaO | 2.45 | 3.69 | 3.19 | 2.76 | 3.91 | 3.91 |
| CaO | 2.16 | 3.12 | 3.00 | 2.40 | 3.40 | 3.40 |
| CdO | 2.23 | 2.99 | 3.32 | 2.35 | 3.32 | 3.32 |
| CoO | 1.90 | 2.38 | 2.92 | 2.13 | 3.01 | 3.01 |
| CrO | 1.96 | 2.76 | 2.78 | | | |
| CuO | 1.96 | 2.56 | 2.96 | 1.95 | 2.88 | 2.62 |
| FeO | 1.95 | 2.35 | 2.95 | 2.15 | 3.04 | 3.04 |
| HeO | 2.75 | 5.34 | 1.23 | | | |
| HfO | 2.10 | 2.75 | 3.17 | | | |
| IrO | 2.04 | 2.87 | 2.91 | | | |
| MgO | 1.96 | 2.63 | 2.92 | 2.11 | 2.98 | 2.98 |
| MnO | 1.94 | 2.57 | 2.86 | 2.22 | 3.14 | 3.14 |
| MoO | 2.06 | 2.47 | 3.25 | | | |
| NbO | 2.09 | 2.63 | 3.22 | 2.11 | 2.98 | 2.98 |
| NiO | 1.93 | 2.49 | 2.77 | 2.09 | 2.96 | 2.96 |
| OsO | 1.72 | 2.29 | 2.43 | | | |
| ReO | 2.06 | 2.50 | 3.24 | | | |
| RhO | 2.03 | 2.80 | 2.93 | | | |
| ScO | 2.00 | 2.92 | 2.65 | 2.22 | 3.14 | 3.14 |
| SiO | 1.86 | 2.76 | 2.48 | 2.36 | 3.85 | 3.85 |
| SnO | 2.16 | 3.26 | 2.82 | 2.25 | 3.74 | 2.72 |
| SrO | 2.30 | 3.40 | 3.11 | 2.56 | 3.63 | 3.63 |
| TaO | 2.10 | 2.61 | 3.26 | | | |
| TiO | 1.98 | 2.39 | 2.98 | 2.09 | 2.96 | 2.96 |
| VO | 2.03 | 2.40 | 2.98 | 2.05 | 2.90 | 2.90 |
| WO | 2.08 | 2.50 | 3.29 | | | |
| YO | 2.18 | 3.25 | 2.77 | 2.47 | 3.49 | 3.49 |
| ZnO | 2.00 | 2.60 | 3.03 | 1.95 | 3.20 | 3.20 |
| ZrO | 2.00 | 2.63 | 3.00 | 2.31 | 3.26 | 3.26 |

together since the difference between them is small in bcc lattice. It is evident from columns 6 and 7 of the table that the relaxed supercells remain cubic for most systems with a small deviation within 3%. This deviation from cubic form is slightly higher than 3% for $Sr_4O_4$ and $Y_4O_4$ embedded supercells. Further, similar to the free clusters, the calculated M-O, M-M, and O-O bond lengths are generally comparable or reduced with reference to their respective experimental values. Some of the O-O bonds in CuO and MnO show appreciable increase and decrease respectively relative to experimental values. Compared to the initial M-O bond lengths, respective relaxed nearest and next nearest neighbor bond lengths for most of the systems are increased by up to 46% and 12% respectively. For Au-O, Ba-O and Sr-O, the increase in the first neighbor bond length

**Table 5.3:** *Structural parameters of the relaxed* $M_4O_4$ *embedded iron systems. M-O, M-M and O-O bond lengths, lattice parameter* $a$ *and* $c/a$ *ratio of the supercell are listed. The two bond lengths under M-O, Fe-O, M-M and O-O columns correspond to the first and second neighbor bonds. For reference, initial bond lengths are listed in the first row.*

| Oxide | $M-O$(Å) | $Fe-O$(Å) | $M-M$(Å) | $O-O$(Å) | $a$(Å) | $c/a$ |
|---|---|---|---|---|---|---|
| MO | 1.47, 2.08 | 1.47, 2.08 | 2.55, 2.94 | 2.55, 2.94 | 11.45 | 1.00 |
| AlO | 1.83, 2.02 | 1.88, 2.14 | 2.99, 3.02 | 2.39, 2.64 | 11.57 | 0.98 |
| AuO | 2.55 | 1.81, 2.02 | 2.82, 2.91 | 4.78, 6.11 | 11.58 | 1.00 |
| BaO | 2.42, 2.58 | 1.86, 2.00 | 3.42, 3.46 | 3.60, 3.87 | 12.00 | 0.97 |
| CaO | 2.11, 2.24 | 1.86, 2.03 | 3.08, 3.14 | 3.00, 3.23 | 11.81 | 0.97 |
| CdO | 2.14, 2.37 | 1.86, 1.98 | 3.27, 3.44 | 2.94, 3.36 | 11.77 | 0.98 |
| CoO | 1.90, 2.20 | 1.84, 1.98 | 3.14, 3.21 | 2.57, 2.97 | 11.62 | 0.98 |
| CrO | 1.90, 2.11 | 1.85, 2.08 | 3.14, 3.17 | 2.48, 2.70 | 11.66 | 0.97 |
| CuO | 1.93, 2.30 | 1.84, 1.93 | 3.12, 3.30 | 2.69, 3.23 | 11.57 | 0.99 |
| FeO | 1.92, 2.13 | 1.84, 2.01 | 3.02, 3.14 | 2.57, 2.92 | 11.62 | 0.98 |
| HeO | 1.95 | 1.80, 1.80 | 1.83, 2.26 | 3.11, 3.89 | 11.48 | 0.99 |
| HfO | 2.05, 2.15 | 1.88, 2.16 | 3.24, 3.24 | 2.66, 2.76 | 11.77 | 0.97 |
| IrO | 2.02, 2.44 | 1.88, 1.99 | 3.51, 3.60 | 2.65, 3.18 | 11.67 | 0.98 |
| MgO | 1.91, 2.06 | 1.85, 2.05 | 2.88, 2.96 | 2.64, 2.90 | 11.65 | 0.98 |
| MnO | 1.90, 2.21 | 1.86, 2.00 | 3.16, 3.22 | 2.55, 2.96 | 11.61 | 0.98 |
| MoO | 2.03, 2.19 | 1.85, 2.15 | 3.33, 3.43 | 2.54, 2.67 | 11.73 | 0.97 |
| NbO | 2.06, 2.19 | 1.86, 2.13 | 3.30, 3.35 | 2.63, 2.76 | 11.77 | 0.97 |
| NiO | 1.89, 2.31 | 1.84, 1.93 | 3.18, 3.29 | 2.64, 3.19 | 11.59 | 0.98 |
| OsO | 2.01, 2.31 | 1.87, 2.10 | 3.49, 3.55 | 2.50, 2.80 | 11.67 | 0.98 |
| ReO | 2.03, 2.20 | 1.84, 2.21 | 3.38, 3.55 | 2.44, 2.52 | 11.67 | 0.98 |
| RhO | 2.05, 2.38 | 1.85, 1.95 | 3.31, 3.44 | 2.79, 3.27 | 11.69 | 0.98 |
| ScO | 2.00, 2.12 | 1.87, 2.08 | 3.04, 3.09 | 2.72, 2.92 | 11.72 | 0.97 |
| SiO | 1.68, 2.56 | 1.95, 1.99 | 3.34, 3.52 | 2.49, 3.36 | 11.49 | 1.00 |
| SnO | 2.07, 2.32 | 1.90, 2.15 | 3.50, 3.53 | 2.59, 2.90 | 11.72 | 0.98 |
| SrO | 2.26, 2.39 | 1.87, 2.02 | 3.29, 3.31 | 3.26, 3.45 | 12.05 | 0.95 |
| TaO | 2.04, 2.15 | 1.87, 2.19 | 3.30, 3.37 | 2.55, 2.63 | 11.74 | 0.97 |
| TiO | 1.96, 2.08 | 1.85, 2.08 | 3.04, 3.10 | 2.59, 2.80 | 11.68 | 0.97 |
| VO | 1.92, 2.09 | 1.84, 2.09 | 3.13, 3.13 | 2.50, 2.70 | 11.68 | 0.97 |
| WO | 2.04, 2.17 | 1.85, 2.23 | 3.34, 3.48 | 2.47, 2.53 | 11.70 | 0.98 |
| YO | 2.15, 2.26 | 1.88, 2.10 | 3.28, 3.29 | 2.95, 3.10 | 11.90 | 0.96 |
| ZnO | 1.94, 2.27 | 1.85, 1.97 | 3.11, 3.29 | 2.65, 3.15 | 11.59 | 0.98 |
| ZrO | 2.09, 2.20 | 1.87, 2.12 | 3.26, 3.27 | 2.77, 2.92 | 11.81 | 0.97 |

reaches to 70%. Corresponding increase in second neighbor bond length is higher than 12%. First and second neighbor bonds of O with Fe atoms of the surrounding matrix, i.e., Fe-O bonds, are also expanded by up to 32% and 6% relative to the respective initial bond lengths. In some systems, the second neighbor Fe-O bonds are either comparable to the initial values or reduced slightly (MgO, NiO, TiO, VO). First and second neighbor M-M bond lengths (except He-He bond) are increased by up to 37% and 22% respectively. Generally, first and second neighbor O-O bond lengths are expanded by up to 28% and 14% respectively. The increase in the O-O bond lengths in $Au_4O_4$ is exceptionally large. Some of the second neighbor O-O bond lengths are reduced relative to the initial values (WO, AlO, MoO). Nevertheless majority of the (i) $M_4O_4$ units remain intact with M and O atoms bonded as in the beginning of the structural optimization, since the changes in bond lengths described above are towards their experimental values in the respective oxides as discussed in the previous paragraph.

In Table 5.3, we have two bond lengths for M-O, M-M and O-O bonds whereas they are single values in free $M_4O_4$ clusters in Table 5.2. This is because our $M_4O_4$ placed in the iron matrix is tetragonal while free $M_4O_4$ is cubic. That is, the two values for M-O, M-M and O-O bonds are measures of tetragonal distortions of the $M_4O_4$ clusters. If these two bond lengths for each of the M-O, M-M, and O-O bonds become same or comparable after relaxation, with the difference between M-M and O-O bonds are reduced, it is an indication that the embedded $M_4O_4$ units tend to transform from the tetragonal form to the cubic form. Comparison of these pairs of bond lengths shows that most of the oxides tend to transform to the cubic form from the initial tetragonal form but the difference between the average M-M and O-O bond lengths keep them deformed. We note here that the oxide nanoparticles in 14YWT ODS steel, as mentioned earlier, is reported to have NaCl (B1-type) structure[**20**]. The same authors subsequently reported that the oxide nanoparticles rather have TlI-like structure which can be regarded as a deformed NaCl structure[**187**]. In $Ca_4O_4$ and $Sr_4O_4$, the transformation from tetragonal to cubic form is almost complete. We also note that the M-M bonds are generally larger than the O-O bonds for most of the oxides. Whereas, in BaO, CaO, and SrO, the M-M bond lengths are less than or equal to the respective O-O bond lengths.

$He_4O_4$, $Au_4O_4$ and $Si_4O_4$ are exceptions. In the former two systems (ii and iii), He and Au atoms stay close to their respective substitutional positions. Whereas the O atoms detach from He and Au atoms and attach with neighboring Fe atoms. Correspondingly, the Fe-O bond lengths are relatively shorter in these systems. Further, while the O atoms from $He_4O_4$ are still located near their original octahedral interstitial sites after relaxation, the O atoms from $Au_4O_4$ are relaxed to the next tetrahedral interstitial sites. O atoms detaching from He and Au atoms and attaching with neighboring Fe atoms may be understood as follows: Noble elements He and Au with negligible reaction with O atoms allow them to leave them. Fe atoms react readily with O atoms to produce Fe-O oxides hence attachment with Fe atoms. $Si_4O_4$ (iv) relaxes to four SiO pairs, located approximately at their respective initial positions. This is because the difference between the first and second nearest neighbor Si-O and O-O bond lengths have become larger than the initial lengths. These 4 different patterns of relaxation (YO, HeO, AuO, SiO) are shown in Fig. 5.2. Thus, majority of the MO clusters including

MgO, AlO, TiO, MnO, NiO, YO, ZrO and HfO remain intact as $M_4O_4$ units in Fe matrix with some amount of distortion from the cubic form. Analysis of relaxed bond lengths further shows that the Fe matrix surrounding the $M_4O_4$ clusters is expanded.

We note here the Erhart has studied the energetics of helium atoms at the oxide-iron interfaces, considering various oxides $(Al_2O_3, TiO_2, Y_2O_3, YAlO_3, Y_3Al_5O_{12}, Y_4Al_2O_9, MgO, CaO, BaO, SrO)$ to identify better oxides to make swelling resistant ODS steels for application in the fusion environments[170]. Brodric *et al.* have studied the mechanism for irradiation damage resistance in $Y_2O_3$ dispersion strengthened steels through the energetics of 4 distinct $Y_2O_3$-Fe interfaces. They have shown that these interface act as strong traps for both interstitial and vacancy defects, facilitating recombination without altering interface structure. This catalytic elimination of defects is considered to be the mechanism behind the improved performance of ODS steels with respect to irradiation creep and swelling[188]. Our work shows that the degree of distortion of the $M_4O_4$ clusters embedded in the iron matrix span over range. Thus, it will be interesting to investigate the helium trapping capability of these oxide-iron interfaces.

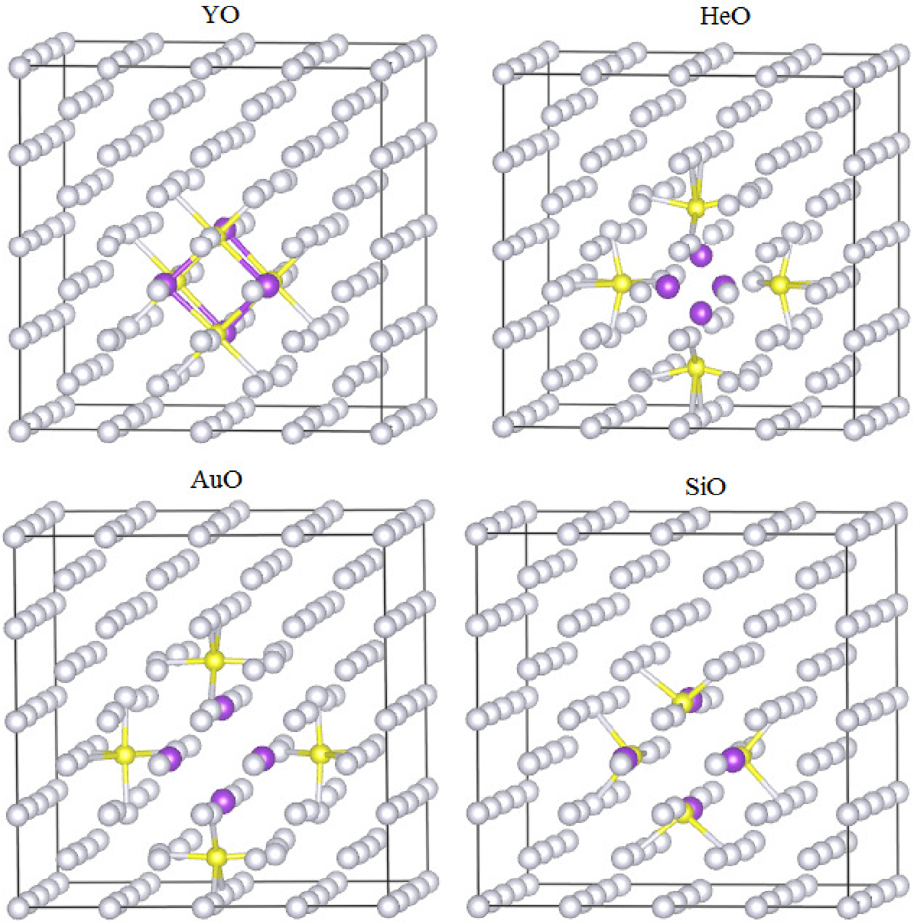

**Figure 5.2:** *Relaxed structure of Fe supercell with embedded* $M_4O_4$ *B1-type oxides depicting 4 different patterns of relaxations of the oxide clusters. Structure with label YO represents the relaxation pattern where the* $M_4O_4$ *unit remains intact. Majority of MO belong this category. Structure with label HeO represents the relaxation pattern where the displacement of O atoms toward neighboring Fe is significant though remain related to their respective original positions. He atoms relax toward each other inward. Structure labeled AuO represents relaxation where the displacement of O atoms away from Au is significant that they are rather close to the next tetrahedral interstitial positions. Structure labelled SiO represents relaxation pattern where the* $M_4O_4$ *unit relaxes to 4 separate MO units though remain close to their respective original positions.*

### 5.3.2 Formation energies of B1-type MO oxides in bcc iron matrix

The formation energies of MO oxides in bcc iron are collected in Table 5.4. Equilibrium volumes, bulk moduli and their pressure derivatives for all the $Fe_{124}M_4O_4$ systems are also collected in Table 5.4. Atomic radius of elements M from WebElements[189] are included in Table 5.4 for comparing the equilibrium volumes. Figure 5.3 shows the formation energies as a function of relaxed volume of each of the 31 MO embedded iron systems. The formation energy of the oxides are related to their ability to resist the motion of dislocations in the iron matrix.

Endothermic interaction between the oxide particles and the iron matrix is considered to keep the oxide particles undissolved in the iron matrix. Undissolved oxide particles are viewed to be more effective to pin dislocations[177]. We see from Fig. 5.3 that the oxides such as BaO, SrO, YO, CaO, SnO, CdO, ZrO, ScO, MgO, ZnO, SiO, AlO, MnO, and TaO with endothermic formation energies, are potential oxides to remain intact in the Fe matrix. Further, the formation energy of YO(10 eV), for instance, is higher than that of $Y_2Ti_2O_7$(4.33 eV)[177] suggesting that YO dispersions would be more stable against dissolution than the pyrochlore. We see further that the oxides such as IrO, HfO, WO, NbO, RhO, ReO, MoO, OsO, TiO, CoO, VO, CrO, NiO, CuO, and FeO, are less stable in the iron matrix since their exothermic formation energies are manifestation of reaction between MO and Fe where exchange of M for Fe or nucleation of M-Fe-O oxide is favourable. The endothermic formation energy of MgO and the exothermic formation energy of TiO are similar to their interface energy with iron matrix[190]. We also find that some of these exothermic oxides such as HfO, WO, MoO and ReO remain intact though they are not observed experimentally. This is likely because the iron matrix enhances the M-O bonding in these oxides. The other oxides such as NiO, NbO, TiO, VO, CoO, and CuO, which are observed experimentally, are calculated to have exothermic formation energies. This may be because the transition metals Ni, Nb, Ti, V, Co, Cu and Cr bond appreciably with the surrounding Fe as is evident from their intermetallic phases[122]. Elements such as Zr, Cd, Y, Sr and Ba have large endothermic formation energies in bcc iron[183] consequently their oxides (with endothermic formation energy) are highly stable in the iron matrix.

**Table 5.4:** *Thermophysical properties of MO embedded bcc Fe for 31 different MO oxides. Formation energy* $E_f$*, volume of relaxed supercells, volume/atom, atomic radius (r) of M, bulk modulus (B) of oxide embedded iron and its pressure derivative (*$B'$*) are listed. Experimental volume of 128 atoms supercell of bcc Fe, i.e.,* $V(Fe_{128})$*, is 1501.12 Å*$^3$*. The corresponding DFT volume is 1456.25 Å*$^3$*. DFT thus underestimates the volume of Fe by 3% and lattice constant by 1%.*

| Oxide | $E_f$(eV) | Volume(Å$^3$) | Volume/atom(Å$^3$) | r(Å) | B(GPa) | $B'$ |
|---|---|---|---|---|---|---|
| AlO | 1.90 | 1500.15 | 11.36 | 1.18 | 161 | 6.4 |
| AuO | -8.75 | 1542.65 | 11.68 | 1.74 | 156 | 4.1 |
| BaO | 27.43 | 1619.67 | 12.27 | 2.53 | 123 | 5.2 |
| CaO | 14.68 | 1551.98 | 11.75 | 1.94 | 140 | 5.8 |
| CdO | 5.57 | 1549.89 | 11.74 | 1.61 | 145 | 6.2 |
| CoO | -3.65 | 1500.49 | 11.37 | 1.52 | 161 | 5.9 |
| CrO | -2.08 | 1503.00 | 11.39 | 1.66 | 162 | 5.8 |
| CuO | -2.96 | 1503.48 | 11.39 | 1.45 | 154 | 6.3 |
| FeO | -2.05 | 1501.34 | 11.37 | 1.56 | 161 | 6.1 |
| HeO | 5.11 | 1490.32 | 11.29 | 0.31 | 137 | 6.0 |
| HfO | -1.65 | 1539.90 | 11.67 | 2.08 | 158 | 6.2 |
| IrO | -10.15 | 1531.07 | 11.60 | 1.80 | 158 | 5.6 |
| MgO | 5.07 | 1509.41 | 11.42 | 1.45 | 151 | 6.5 |
| MnO | 1.24 | 1502.02 | 11.38 | 1.61 | 161 | 6.5 |
| MoO | -2.96 | 1523.10 | 11.54 | 1.90 | 167 | 5.6 |
| NbO | -2.96 | 1531.85 | 11.60 | 1.98 | 164 | 5.7 |
| NiO | -3.15 | 1500.29 | 11.37 | 1.49 | 157 | 6.0 |
| OsO | -2.49 | 1524.35 | 11.54 | 1.85 | 164 | 5.7 |
| ReO | -8.08 | 1522.34 | 11.53 | 1.88 | 170 | 5.4 |
| RhO | -5.62 | 1526.86 | 11.57 | 1.73 | 157 | 5.7 |
| ScO | 3.89 | 1528.23 | 11.58 | 1.84 | 154 | 6.1 |
| SiO | 2.00 | 1499.77 | 11.35 | 1.11 | 160 | 6.3 |
| SnO | 12.41 | 1548.05 | 11.69 | 1.45 | 151 | 6.0 |
| SrO | 21.64 | 1586.54 | 11.57 | 2.19 | 133 | 5.0 |
| TaO | 0.42 | 1530.56 | 11.60 | 2.00 | 165 | 5.6 |
| TiO | -1.28 | 1511.53 | 11.45 | 1.76 | 163 | 6.1 |
| VO | -2.45 | 1504.23 | 11.40 | 1.71 | 166 | 6.1 |
| WO | -7.32 | 1528.22 | 11.58 | 1.93 | 172 | 5.0 |
| YO | 10.18 | 1568.30 | 11.88 | 2.12 | 124 | 3.4 |
| ZnO | 1.43 | 1508.26 | 11.42 | 1.42 | 154 | 6.4 |
| ZrO | 1.41 | 1545.98 | 11.71 | 2.06 | 155 | 5.5 |

It may be noted that, in Table 5.4, HeO is listed to be endothermic though He and O atoms do not stay together as a cluster in the iron matrix. Thus the formation energy of HeO do not correspond to a single $He_4O_4$ entity embedded in the iron matrix rather corresponds to separate He and O atoms dissolved in the iron matrix which is

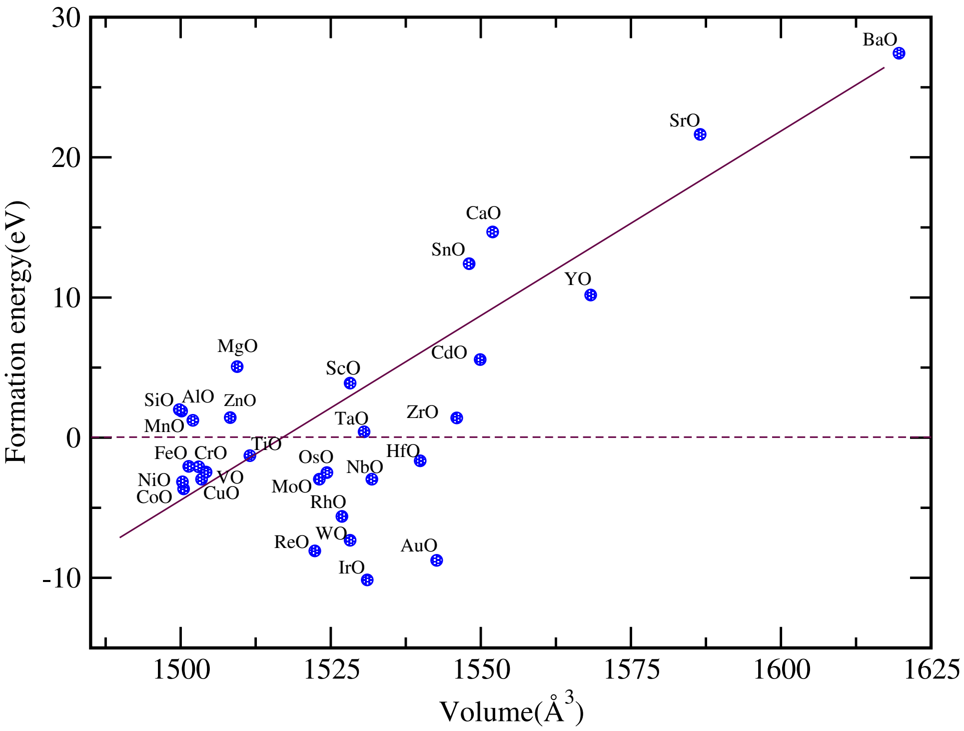

**Figure 5.3:** *Formation energy of B1-type oxides in bcc iron versus volume of the oxide embedded bcc iron. The lines are guides to eye.*

endothermic perhaps because He assume apparently large size (as evident from the He-He bond length in iron matrix) which cause tensile stress on the matrix leading to increase in the total energy of $Fe_{124}He_4O_4$. Thus the idea of endothermic formation energy(known as dissolution energy by Takahashi and Tanaka) for the stability of embedded oxide against dissolution[177] is valid only if the oxide cluster remains intact. For AuO also, the formation energy corresponds to Au and O atoms separately dissolved in the iron matrix rather than single $Au_4O_4$ units. Therefore, HeO and AuO are omitted from the subsequent discussions. But we would like to note that, in ODS steel under irradiation, O and He atoms are very likely to encounter each other. This work suggests that the tendency of O to trap He or vice versa is weak.

Another observation from Fig. 5.3 is that the formation energies exhibit a correlation with the radius of the M atoms (see Table 5.4) of the oxides when we consider BaO, SrO, YO, HfO, ZrO, TaO, CaO, NbO, WO, MoO, ScO, OsO, TiO, VO, and FeO. Oxides such as

MgO, SiO, MnO and IrO show appreciable deviation from this relation. We show later in Section 5.3.5 that the oxides that deviate from this correlation are those in which the hybridization between the valence orbitals of M and Fe are either weak or strong relative to those in other oxides.

### 5.3.3 Bulk modulus of B1-type MO oxide embedded bcc iron

The bulk modulus is a measure of the ability of a substance to withstand changes in its volume by compression. The bulk modulus is related inversely to the thermal expansion coefficient of solids[191]. Thus the bulk modulus of oxide embedded iron will be a useful indicator to identify the oxides for ODS steel that resist compression or expansion.

Moreover, DFT calculation of the bulk modulus of oxide embedded iron is rare though common for elemental and compound crystals[192, 193]. Therefore we computed the bulk modulus of all the 31 oxide embedded iron systems by fitting their E(V) data to the Vinet equation of state[184]. Table 5.4 lists the calculated equilibrium volumes, bulk moduli and their pressure derivatives for all the $Fe_{124}M_4O_4$ systems. Figure 5.4 shows the E(V) equation of state for all these systems. Smooth curves indicate that Vienna Ab initio Simulation Package gives E(V) for $Fe_{124}M_4O_4$ systems in the same manner as it gives for elemental and compound crystals. It is evident from Table 5.4 that the relaxed equilibrium volumes of all the systems, obtained by fitting the E(V) in Fig. 5.4, are increased with reference to pure Fe. This increase in volume is generally from 3 to 5% except for CaO, SrO, BaO, YO, ZrO, HfO, CdO, and SnO embedded systems for them the increase is between 5 to 11%. Estimates of volumes of $M_4O_4$ from their respective atom sizes show that the increase in the volumes of the supercells are generally more than that contributed by $M_4O_4$ units.

It is further evident from Table 5.4 that the bulk modulus of oxide embedded iron is generally reduced compared to the PAW-PBE bulk modulus of pure iron (185 GPa)[194].

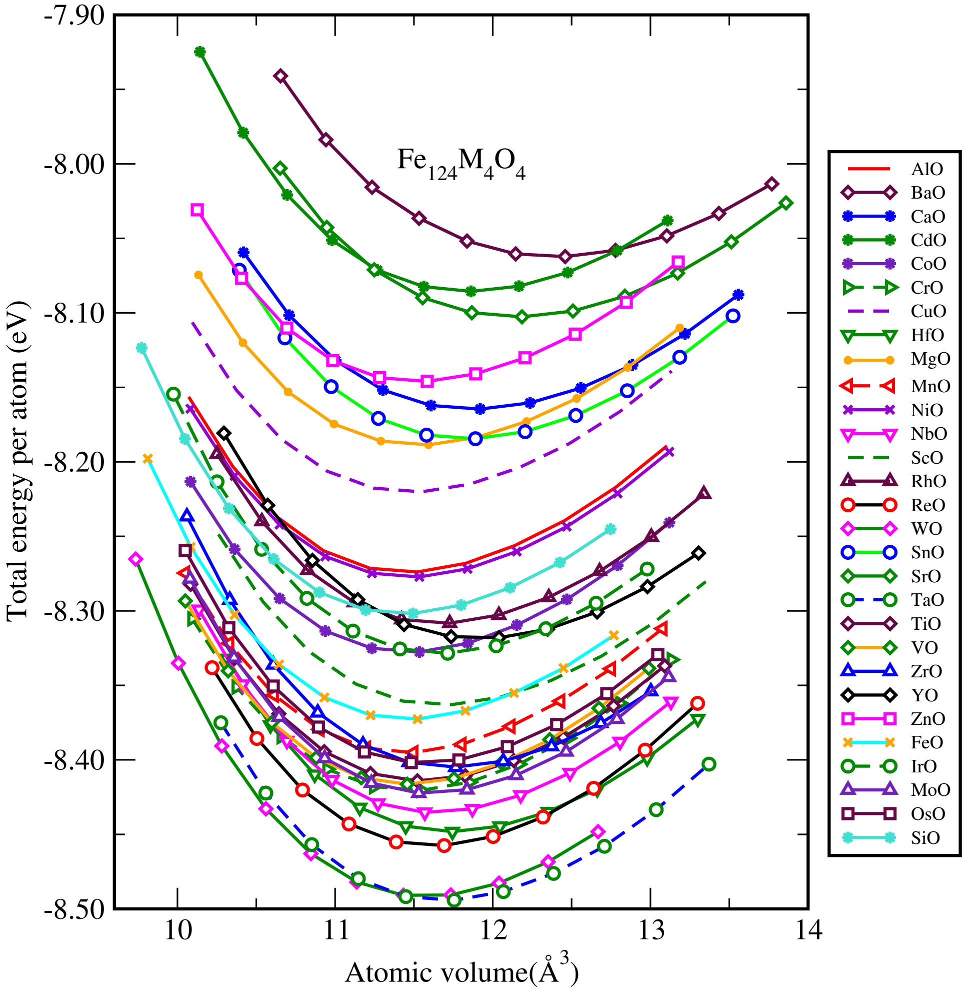

**Figure 5.4:** *E(V) equation of state for B1-type oxide embedded bcc iron supercells* $Fe_{124}M_4O_4$.

This reduction in bulk modulus correlates with the increase in the equilibrium volumes of the oxide embedded iron as can be seen from Table 5.4 and Fig. 5.5. The reduction in bulk modulus of bcc iron due to the oxide particles appears to be in agreement with the reduction in bulk modulus and increase in lattice parameters of bcc iron with alloying elements Al, Si, V, Cr, Mn, Co, Ni, and Rh[195] as well as with the reduction in bulk modulus of bcc iron with embedded $A_2B_2O_7$ oxide particles[177]. We also see from Fig. 5.5 that the oxides such as CaO, SrO and BaO, with relatively higher contribution to equilibrium volumes, have reduced the bulk modulus of bcc iron appreciably. The reduction in the bulk moduli of oxide embedded iron with the associated increase in the volumes compared to pure iron is further in accordance with the reduction in melting point and density of ODS steels compared to pure iron[189, 196]. Compared to ScO embedded iron, the bulk modulus of WO embedded iron is appreciably higher though their volumes are comparable. Correspondingly, it is found that the Fe-W bond lengths (2.32 Å) are shorter than Fe-Sc bond lengths (2.48 Å) indicating that the Fe-W bonding is relatively strong.

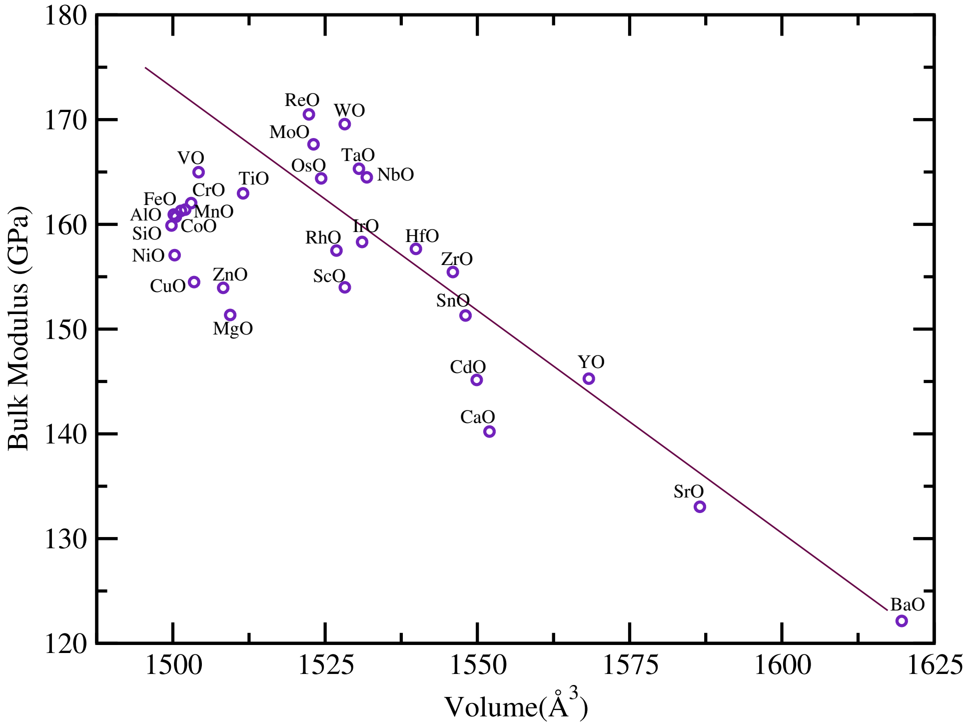

**Figure 5.5:** *Bulk modulus versus relaxed equilibrium volumes of oxide embedded bcc iron. The line is a guide to eye.*

### 5.3.4 Correlation between the formation energy and the bulk modulus of the oxide embedded bcc iron

Figure 5.6 plots the calculated formation energies of the oxides in bcc iron and the bulk moduli of the oxide embedded bcc iron. ODS steels with higher bulk moduli and endothermic formation energies for the oxide particles are considered to be able to resist thermal expansion and stop dislocation motion leading to stable microstructure at elevated temperatures[177]. In this connection, Fig. 5.6 indicates that ZrO, AlO, SiO,

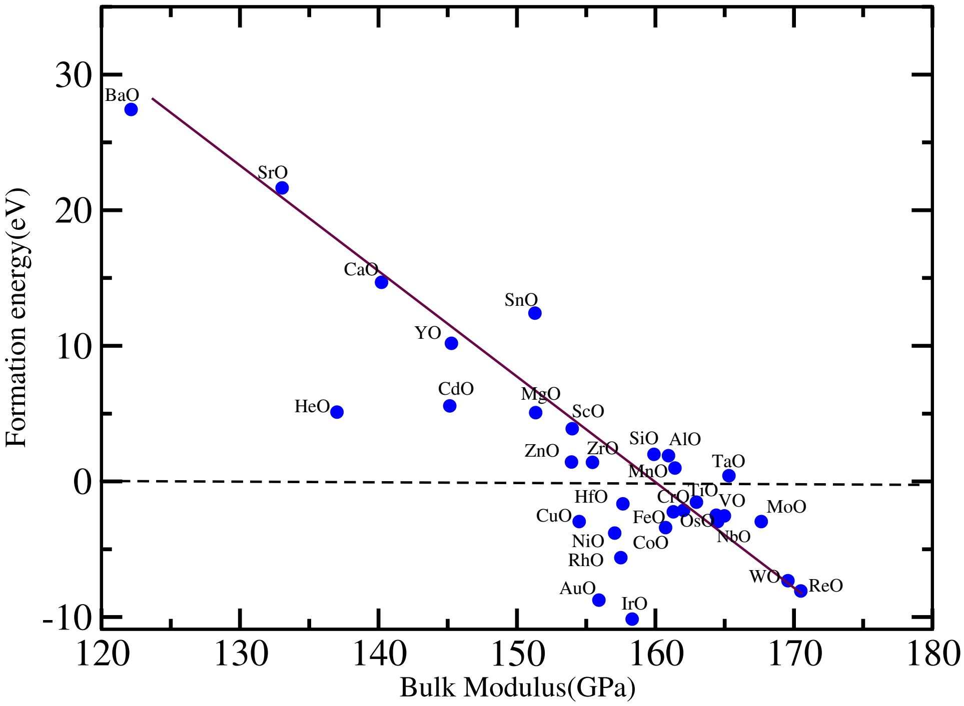

**Figure 5.6:** *Formation energy of B1-type oxides in bcc Fe versus bulk modulus of the oxide embedded bcc Fe. The lines are guides to eye.*

MnO, and TaO have endothermic formation energies with relatively higher bulk moduli for respective oxide embedded bcc iron, making them suitable candidates as dispersions in ODS iron alloys. It is also evident that oxides such as, YO, CdO, SnO, MgO, ZnO, and ScO constitute stable oxides in the iron matrix though they cause a reduction of the bulk modulus. The other oxides, such as, TiO, VO, CrO, FeO, CoO, NiO, MoO, RhO, HfO, WO, ReO, OsO, and IrO, retain or enhance the bulk modulus of the iron matrix, but their exothermic formation energies indicate that they are chemically less stable. This work thus show that TiO stays intact in the bcc iron matrix but it is not the most stable oxide. Figure 5.6 further shows that the formation energies of the oxide particles have a correlation with the bulk modulus of the respective oxide embedded iron. We also see that CaO, SrO, and BaO are quite stable against dissolution, but they cause considerable reduction of bulk modulus of the iron matrix.

It is evident that most of the oxides predicted to be stable in the iron matrix (except AlO and TaO) are observed experimentally (see Table 5.1). Whereas, many of the oxides, which are unstable in the iron matrix, are not observed experimentally (AuO, CrO, HfO, IrO, MoO, OsO, ReO, RhO, WO. It is noted here that Hf-O precipitates with Hf:O ratio close to 1 has been reported in Fe-14Cr-0.22Hf alloy fabricated by spark plasma sintering[197]). Inspection of Iron-binary phase diagram[122] show further that the majority of the M's of exothermic MO oxides (Ir, Rh, Ni, Co, Cr, V, Mo, Nb, and Re) form extended solid solution with Fe unlike M's of endothermic oxides (Ca, Sr, Ba, Y, Cd, Sn, Mg, Sc, Zr, Mn and Ta).

We have also seen that the oxides with endothermic formation energies, which tend to retain the bulk modulus of the iron matrix, are potential candidates for the development of improved ODS steels. Comparison of our bulk moduli of the MO embedded iron with those of the $A_2B_2O_7$ embedded iron by Takahashi and Tanaka[177] indictes that the MO oxides are better candidate to retain/improve the bulk modulus of the iron matrix. Thus the MO oxides, such as, SnO, MgO, YO, CdO, ScO, ZrO, AlO, SiO, MnO, TaO, and ZnO, are predicted to be suitable candidates to be investigated as dispersion in ferritic matrix. We note that, among these oxides, MgO has been already studied as an alternative dispersion in ODS steels[171, 172].

### 5.3.5 Electronic density of states of B1-type MO oxide embedded bcc iron

We have seen that the formation energies are endothermic for some oxides and exothermic for other oxides. Since the formation energies are manifestation of bonding between Fe, M and O atoms, we analyzed the projected electronic density of states of the oxide embedded iron to gain more insight into the origin of the exothermic and endothermic formation energies. Figure 5.7 shows the projected density of state of *s* or *d* electrons of M, *d* electrons of nearest Fe and the *p* electrons from O atoms. We see that the *p* density of states are placed almost over the same energy range with similar hybridization with the Fe and M density of states.

Whereas the *s* or *d* density of states from M's exhibit distinguishable degrees of overlap with the *d* density of states from nearest Fe. That is, the M's with exothermic formation energy for MO, such as NiO, RhO, and IrO exhibit strong overlap with the Fe *d* density of states while the M's with endothermic formation energy for MO, such as MgO,

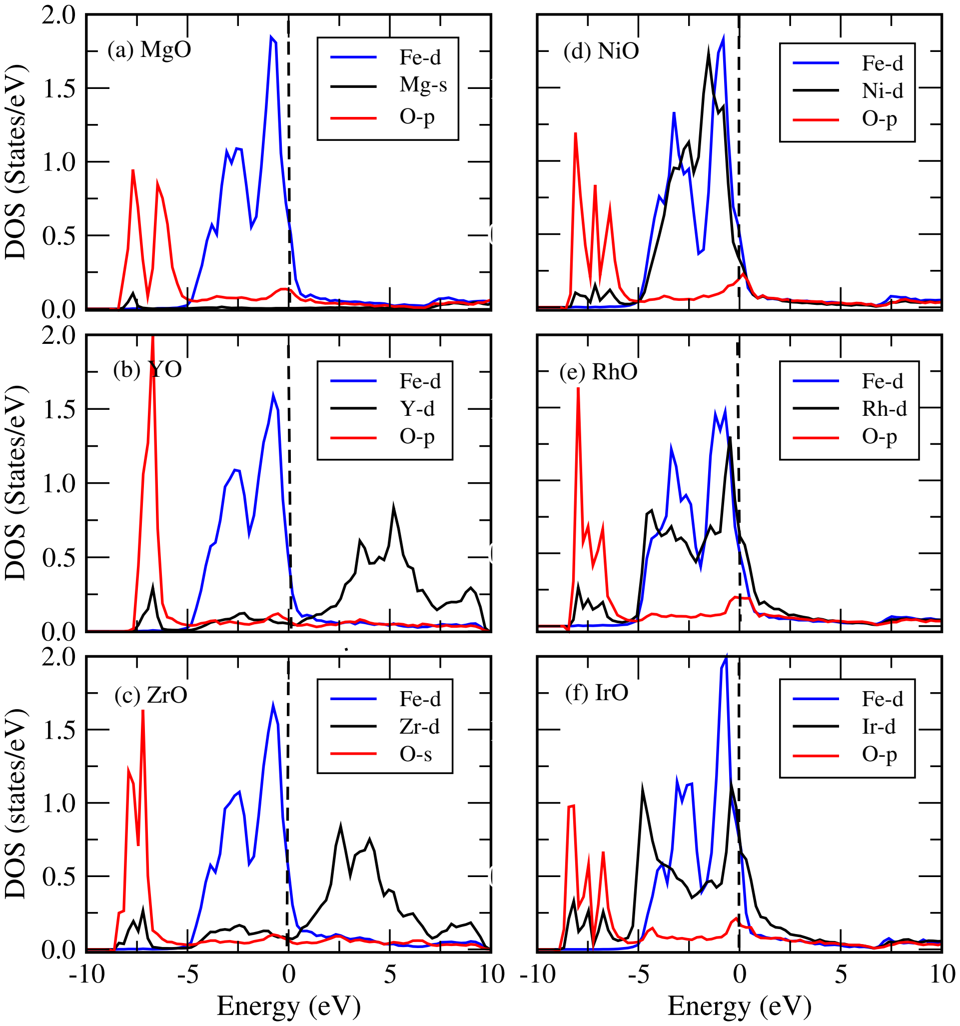

**Figure 5.7:** *Projected electronic density of states from (a) MgO, (b) YO, (c) ZrO, (d) NiO, (e) RhO and (f) IrO embedded bcc iron. Vertical lines at* 0 eV *are Fermi levels.*

YO and ZrO, exhibit weak overlap with the Fe density of states. We also see from (a),(b), and (c) panels of Fig. 5.7 that the hybridization between Mg-*s* and Fe-*d* is negligible compared to that between Y-*d* and Fe-*d*, and between Zr-*d* and Fe-*d* states. This leads to relatively large positive formation energy for MgO, which makes it to deviate from the correlation between the formation energy and volume in Fig. 5.3. Looking at the DOS in the (d), (e), and (f) panels of Fig. 5.7, we see that the hybridization between Ir-*d* and Fe-*d* over -6 to 0 eV is strong compared to that between Ni-*d* and Fe-*d*, and between Rh-*d* and Fe-*d*. (Ir-*d* band width and the area under Ir-*d* occupied DOS are more compared to those of Ni-*d* and Rh-*d* DOS). This strong hybridisation between Ir and Fe states leads to relatively large exothermic formation energy for IrO in the iron matrix, causing it deviation from the correlation in Fig. 5.3. We note further that most of the MO's derive their mechanism for the endothermic or exothermic formation energies from the degree of overlap between valence electronic density of states from M and Fe atoms.

## 5.4 Conclusions

Stability of the oxide dispersion against dissolution is important for the reliable long-term performance of the ODS steel core components. Therefore, the stability of the oxide dispersion and the associated properties of ODS steels have been studied actively. For the oxide nanoparticles, various compositions and structures have been discussed in the literature. B1-type TiO nanoparticles have been observed in certain ODS steel. The B1-type oxide is considered to have great chemical flexibility[20]. To improve our understanding on the structure and stability of the B1-type oxides as dispersions in ODS ferritic steel, we carried out calculations of formation energies of 31 different oxides in bcc iron matrix and their bulk moduli using DFT calculations. The calculations were performed with $Fe_{124}M_4O_4$ systems modeled on $4 \times 4 \times 4$ bcc supercells.

Analysis of the relaxed structures from our work show that many of the oxides embedded in the iron matrix remain structurally intact with some amount of distortion from the cubic form. Formation energies of these oxides show a correlation with the equilibrium volumes of the oxide embedded iron. Bulk moduli of the oxide embedded iron show an inverse correlation with their equilibrium volumes. Further, the formation energies of the oxides in the iron matrix exhibit an inverse correlation with the bulk moduli of the oxide embedded iron. The degree of hybridization between the valence states of M and the surrounding Fe atoms is found to be the mechanism for the endothermic or exothermic formation energies of the oxides in the iron matrix. That is, the M's with exothermic formation energy for MO, such as NiO, RhO and IrO, exhibit strong hybridization of their d density of states with the Fe d density of states while the M's with endothermic formation energy for MO, such as MgO, YO and ZrO, exhibit weak overlap with the Fe density of states.

Endothermic formation energy is related to the resistance of the oxide particle against dissolution into constituent atoms. Oxide embedded iron with relatively higher bulk moduli are considered to resist dislocation motion and thermal expansion better. Our work predicts that oxides, namely YO, CdO, SnO, MgO, ScO, ZrO, SiO, AlO, MnO, TaO and ZnO, with endothermic formation energy in the iron matrix combined with better bulk moduli, have the potential to improve the properties of ODS steels. This work also indicates that B1-type MO oxides retain/improve the bulk modulus of iron matrix better compared to $A_2B_2O_7$ pyrochlore-type oxides. MgO has been already studied as an alternative dispersion in ODS steels. AlO, CrO, MoO, TaO, WO and ReO dispersions are predicted to enhance the bulk moduli of the iron matrix and remain structurally intact though they are not observed experimentally. This indicates that the iron matrix confine these oxides to remain intact.

# 6

# Summary and future scope of the work

## 6.1 Summary

In order to understand the atomic level properties of steels, we have performed an extensive set of first principles electronic structure calculations of the formation and binding energies of atomic defects (vacancy, solute atoms, solute-solute, and vacancy-solute pairs) in ferromagnetic bcc iron. An extended set of solute elements with atomic numbers from 1 to 54 have been considered. Our calculations reveal the trends in the solute formation energy and solute size factor. It is found that the formation energies of solutes from fourth and fifth periods vary with their atomic numbers such that they reach maximum near the ends of the periods and minimum in between, with local hump near Cu and Ag (like a quasi parabolic valley). Solutes from the second and third periods show similar trends like the elements near the ends of the fourth and fifth periods. The common solute addition to Fe ($3d$, $4d$, and $sp$ elements) are found to possess moderate formation energies. Large endothermic formation energies are obtained for solutes that lack solubility in Fe (alkali, halogen, noble gas, alkaline earth, Se, Ag, and Cd atoms).

Like formation energies, the size factors of the solute elements also vary with their atomic numbers such that they reach maximum near the ends of the periods and minimum in the middle. The majority of solute atoms have positive size factor, i.e., their effective size in the iron matrix are higher than that of iron atoms. Immiscible solute atoms generally possess relatively large size factors. Solubilities estimated from our formation energies are found to be in reasonable agreement with those from the phase diagram database.

The solute-solute and vacancy-solute binding energies vary with the atomic number of the solutes in a manner inverse to the formation energies and size factors. That is, strong binding energies occur for solute-solute or vacancy-solute pairs at the ends of the periods and weak binding energies for pairs from the middle of the periods. We also find that the 1nn solute-solute binding is repulsive for many solutes, while the vacancy-solute binding is always attractive. The size factors of isoelectronic sets of elements increase down the groups with an associated increase of the formation energies. The strength of the solute-solute and vacancy-solute binding energy increases with the size factors of solutes down the group. Comparison of our predicted vacancy-solute binding energies of 3d and 4d transition elements with their corresponding calculated diffusion coefficient from the literature show a significant correlation whereby solutes with strong binding energies possess higher diffusion coefficient and vice versa. This, in turn, indicates that our predicted vacancy-solute binding energies of other solutes are useful to estimate their diffusion coefficients.

In addition to atomic defects, the stability of oxide particles embedded in the iron matrix have been studied. The stability of the oxide dispersion against dissolution is important for the reliable long-term performance of the ODS steel core components. Therefore, the stability of the oxide dispersion and the associated properties of ODS steels have been studied actively. The improved properties of ODS ferritic steels are related to the densely dispersed fine oxide nanoparticles in the iron matrix. B1-type TiO nanoparticles have been observed in certain ODS steel. The B1-type oxide is considered to have great chemical flexibility. To improve our understanding on the structure and stability of the B1-type oxides as dispersions in ODS ferritic steel, we carried out calculations of formation energies of 31 different oxides in bcc iron matrix and their bulk moduli using DFT calculations. The calculations were performed with $Fe_{124}M_4O_4$ systems modeled on $4 \times 4 \times 4$ bcc supercells.

Analysis of the relaxed structures from our work show that many of the oxides embedded in the iron matrix remain structurally intact with some amount of distortion from the cubic form. Formation energies of these oxides show a correlation with the equilibrium volumes of the oxide embedded iron. Bulk moduli of the oxide embedded iron show an inverse correlation with their equilibrium volumes. Further, the formation energies of the oxides in the iron matrix exhibit an inverse correlation with the bulk moduli of the oxide embedded iron. The degree of hybridization between the valence states of M and the surrounding Fe atoms is found to be the mechanism for the endothermic or exothermic formation energies of the oxides in the iron matrix. That is, the M's with exothermic formation energy for MO, such as NiO, RhO and IrO, exhibit strong hybridization of their d density of states with the Fe d density of states while the M's with endothermic formation energy for MO, such as MgO, YO and ZrO, exhibit weak overlap with the Fe density of states.

Endothermic formation energy is related to the resistance of the oxide particle against dissolution into constituent atoms. Oxide embedded iron with relatively higher bulk moduli are considered to resist dislocation motion and thermal expansion better. Our work predicts that oxides, namely YO, CdO, SnO, MgO, ScO, ZrO, SiO, AlO, MnO, TaO and ZnO, with endothermic formation energy in the iron matrix combined with better bulk moduli, have the potential to improve the properties of ODS steels. This work also indicates that B1-type MO oxides retain/improve the bulk modulus of iron matrix better compared to $A_2B_2O_7$ pyrochlore-type oxides. MgO has been already studied as an alternative dispersion in ODS steels. AlO, CrO, MoO, TaO, WO and ReO dispersions are predicted to enhance the bulk moduli of the iron matrix and remain structurally intact though they are not observed experimentally. This indicates that the iron matrix confine these oxides to remain intact.

## 6.2 Future scope of the work

- Study of defect formation and binding energies in Fe-Cr alloys.
- Investigate experimentally the predicted oxides (SnO, MgO, YO, CdO, ScO, ZrO, AlO, SiO, MnO, TaO, and ZnO) are suitable candidates as dispersion in ferritic matrix.
- Modelling the yield strength of the steel.

# References

[1] C. Azevedo, “Selection of fuel cladding material for nuclear fission reactors,” *Eng. Fail. Anal.*, vol. 18, pp. 1943 – 1962, 2011.

[2] A. T. Motta, A. Yilmazbayhan, M. J. G. da Silva, R. J. Comstock, G. S. Was, J. T. Busby, E. Gartner, Q. Peng, Y. H. Jeong, and J. Y. Park, “Zirconium alloys for supercritical water reactor applications: Challenges and possibilities,” *J. Nucl. Mater.*, vol. 371, pp. 61 – 75, 2007.

[3] P.Hosemanna, D.Frazera, M.Fratonia, A.Bolinda, and M.F.Ashbyb, “Materials selection for nuclear applications: Challenges and opportunities,” *Scripta Mater.*, vol. 143, pp. 181–187, 2018.

[4] J. Robertson, “Zirconium— an international nuclear material,” *J. Nucl. Mater.*, vol. 100, pp. 108 – 118, 1981.

[5] D. O. Northwood, “The development and applications of zirconium alloys,” *Materials & Design*, vol. 6, pp. 58 – 70, 1985.

[6] J. Gravenor and J. Douglas, “Elevated temperature tensile properties of irradiated 20/25/Nb stainless steel fuel pin cladding at low and high strain rates,” *J. Nucl. Mater.*, vol. 158, pp. 87 – 95, 1988.

[7] S. Walker, A. Yu, and R. Fenner, “Pellet-clad mechanical interaction: pellet-clad bond failure and strain relief,” *Nucl. Eng. Des.*, vol. 138, pp. 403 – 408, 1992.

[8] K. Murty and I. Charit, “Structural materials for gen-iv nuclear reactors: Challenges and opportunities,” *J. Nucl. Mater.*, vol. 383, pp. 189 – 195, 2008.

[9] S. J. Zinkle and J. T. Busby, “Structural materials for fission & fusion energy,” *Materials Today*, vol. 12, pp. 12 – 19, 2009.

[10] W. Johnston, J. Rosolowski, A. Turkalo, and T. Lauritzen, “Nickel-ion bombardment of annealed and cold-worked type 316 stainless steel,” *J. Nucl. Mater.*, vol. 48, pp. 330 – 338, 1973.

[11] H. Kurishita, T. Muroga, H. Watanabe, N. Yoshida, H. Kayano, and M. Hamilton, “Effect of FFTF irradiation on tensile properties of P— and Ti— modified model austenitic alloys with small amounts of boron,” *J. Nucl. Mater.*, vol. 212, pp. 519 – 524, 1994.

[12] V. Sagaradze, S. Lapin, M. Kirk, and B. Goshchitskii, “Influence of high-dose Kr+ irradiation on structural evolution and swelling of 16Cr–15Ni–3Mo–1Ti aging steel,” *J. Nucl. Mater.*, vol. 274, pp. 287 – 298, 1999.

[13] G. R. Odette, N. J. Cunningham, T. Stan, M. E. Alam, and Y. De Carlan, "Chapter 12 - nano-oxide dispersion-strengthened steels," in *Structural Alloys for Nuclear Energy Applications* (G. R. Odette and S. J. Zinkle, eds.), pp. 529 – 583, Boston: Elsevier, 2019.

[14] S. Ukai, T. Nishida, H. Okada, T. Okuda, M. Fujiwara, and K. Asabe, "Development of oxide dispersion strengthened ferritic steels for FBR core application (i)," *J. Nucl. Sci. Technol.*, vol. 34, pp. 256–263, 1997.

[15] R. L. Klueh, J. P. Shingledecker, R. W. Swindeman, and D. T. Hoelzer, "Oxide dispersion strengthened steels: A comparison of some commercial and experimental alloys," *J. Nucl. Mater.*, vol. 341, pp. 103–114, 2005.

[16] S. Ukai and S. Ohtsuka, "Nano-mesoscopic structure control in $9Cr-ODS$ ferritic steels," *Energy Mater.*, vol. 2, pp. 26–36, 2007.

[17] G. R. Odette, M. Alinger, and B.D.Wirth, "Recent developments in irradiation resistant steels," *Annu. Rev. Mater. Res.*, vol. 38, pp. 471–503, 2008.

[18] Y. Jiang, J. R. Smith, and G. R. Odette, "Formation of $Y-Ti-O$ nanoclusters in nanostructured ferritic alloys: A first-principles study," *Phys. Rev. B*, vol. 79, p. 064103, 2009.

[19] L. L. Hsiung, M. J. Fluss, S. J. Turney, B. W. Choi, Y. Serruys, F. Willaime, and A. Kimura, "Formation mechanisms and the role of nanoparticles in $Fe-Cr$ ODS steels developed for radiation tolerance," *Phys. Rev. B*, vol. 82, p. 184103, 2010.

[20] A. Hirata, T. Fujita, Y. Wen, J. Schneibel, C. T. Liu, and M.Chen, "Atomic structure of nanoclusters in oxide dispersion strengthened steels," *Nat. Mater.*, vol. 10, pp. 922–926, 2011.

[21] X. Zhou, Z. Ma, L. Yu, Y. Huang, H. Li, and Y. Liu, "Formation mechanisms of $Y-Al-O$ complex oxides in $9Cr-ODS$ steels with Al addition," *J. Mater. Sci.*, vol. 54, pp. 7893–7907, 2019.

[22] M. S. El-Genk and J.-M. Tournier, "A review of refractory metal alloys and mechanically alloyed-oxide dispersion strengthened steels for space nuclear power systems," *J. Nucl. Mater.*, vol. 340, pp. 93 – 112, 2005.

[23] S. Ukai and M. Fujiwara, "Perspective of ODS alloys application in nuclear environments," *J. Nucl. Mater.*, vol. 307-311, pp. 749 – 757, 2002.

[24] B. Raj, M. Vijayalakshmi, P. V. Rao, and K. Rao, "Challenges in materials research for sustainable nuclear energy," *MRS Bull.*, vol. 33, pp. 327–337, 2008.

[25] R.Balasubramaniam, "Callister's materials science and engineering," *John Wiley & Sons*, 2009.

[26] T. He, Y. Jiang, R. Zhou, and J. Feng, "Point defect interactions in iron lattice: a first-principles study," *RSC Adv.*, vol. 6, pp. 45250–45258, 2016.

[27] G. E. Totten, *Steel heat treatment: metallurgy and technologies*. CRC press, 2006.

[28] R. Huseby, "Atomized steel powder having improved hardenability," 1973. US Patent 3,725,142.

[29] S. Huang, B. Wu, Z. Wang, Y. Yu, C. Wang, L. Yan, X. Li, C. Shang, and R. Misra, "EBSD study on the significance of carbon content on hardenability," *Materials Letters*, vol. 254, pp. 412–414, 2019.

[30] C. R. Funk and R. M. Barnhart, "Method of adding lead to steel," 1958. US Patent 2,854,716.

[31] M. Calcagnotto, D. Ponge, and D. Raabe, "On the effect of manganese on grain size stability and hardenability in ultrafine-grained ferrite/martensite dual-phase steels," *Metall. Mater. Trans. A*, vol. 43, pp. 37–46, 2012.

[32] J. Redmond, P. Grobner, and V. Bišs, "Effect of molybdenum on creep properties of a ferritic $18\mathrm{Cr}-\mathrm{Nb}-\mathrm{Ti}$ steel for catalytic converters," *J. Min. Met. Mat. S.*, vol. 33, pp. 19–24, 1981.

[33] G. Zalazinskii, L. Leont'ev, and T. Shchennikova, "Effect of copper and molybdenum additions on the microstructure and mechanical properties of steel shot," *Russian Metallurgy (Metally)*, vol. 2007, pp. 282–286, 2007.

[34] D. Liu, R. Liu, and Y. Wei, "Influence of tungsten on microstructure and wear resistance of iron base hardfacing alloy," *Mater. Sci. Technol.*, vol. 30, pp. 316–322, 2014.

[35] T. Pochapsky, "Heat capacity and resistance measurements for aluminum and lead wires," *Acta Metallurgica*, vol. 1, pp. 747 – 751, 1953.

[36] W. Triftshäuser, "Positron trapping in solid and liquid metals," *Phys. Rev. B*, vol. 12, pp. 4634–4639, 1975.

[37] L. Kornblit, "Single vacancy formation energies in BCC metals," *Physica B+ C*, vol. 106, pp. 351–355, 1981.

[38] U. Krause, J. Kuska, and R. Wedell, "Monovacancy formation energies in cubic crystals," *Phys. Status Solidi (b)*, vol. 151, pp. 479–494, 1989.

[39] A. Ghorai, "Calculation-of some defect parameters in FCC metals," *Phys. Status Solidi (b)*, vol. 167, pp. 551–560, 1991.

[40] J. Harder and D. Bacon, "Point-defect and stacking-fault properties in body-centred-cubic metals with n-body interatomic potentials," *Philos. Mag. A*, vol. 54, pp. 651–661, 1986.

[41] G. Ackland, G. Tichy, V. Vitek, and M. Finnis, "Simple n-body potentials for the noble metals and nickel," *Philos. Mag. A*, vol. 56, pp. 735–756, 1987.

[42] V. Rosato, M. Guillope, and B. Legrand, "Thermodynamical and structural properties of fcc transition metals using a simple tight-binding model," *Philos. Mag. A*, vol. 59, pp. 321–336, 1989.

[43] T. Beuerle, R. Pawellek, C. Elsasser, and M. Fahnle, “The influence of the atomic-sphere approximation on the calculation of the vacancy formation energy of Li,” *J. Phys. Condens. Matter*, vol. 3, pp. 1957–1959, 1991.

[44] M. Mehl and B. Klein, “All-electron first-principles supercell total-energy calculation of the vacancy formation energy in aluminium,” *Physica B Condens. Matter*, vol. 172, pp. 211–215, 1991.

[45] R. Benedek, L. Yang, C. Woodward, and B. Min, “Formation energy and lattice relaxation for point defects in Li and Al,” *Phys. Rev. B*, vol. 45, p. 2607, 1992.

[46] P. A. Korzhavyi, I. A. Abrikosov, B. Johansson, A. V. Ruban, and H. L. Skriver, “First-principles calculations of the vacancy formation energy in transition and noble metals,” *Phys. Rev. B*, vol. 59, pp. 11693–11703, 1999.

[47] R. Nazarov, T. Hickel, and J. Neugebauer, “Vacancy formation energies in fcc metals: Influence of exchange-correlation functionals and correction schemes,” *Phys. Rev. B*, vol. 85, p. 144118, 2012.

[48] J. Spitaler and S. K. Estreicher, “Perspectives on the theory of defects,” *Frontiers in Materials*, vol. 5, p. 70, 2018.

[49] G. Grimvall, *Thermophysical Properties of Materials*. Elsevier Science, 1999.

[50] C. Wolverton, “Solute–vacancy binding in aluminum,” *Acta Mater.*, vol. 55, pp. 5867 – 5872, 2007.

[51] C. Domain, “Ab initio modelling of defect properties with substitutional and interstitials elements in steels and Zr alloys,” *J. Nucl. Mater.*, vol. 351, pp. 1 – 19, 2006.

[52] T. Ohnuma, N. Soneda, and M. Iwasawa, “First-principles calculations of vacancy–solute element interactions in body-centered cubic iron,” *Acta Mater.*, vol. 57, pp. 5947 – 5955, 2009.

[53] P. Olsson, T. P. C. Klaver, and C. Domain, “Ab initio study of solute transition-metal interactions with point defects in bcc Fe,” *Phys. Rev. B*, vol. 81, p. 054102, 2010.

[54] O. Gorbatov, P. Korzhavyi, A. Ruban, B. Johansson, and Y. Gornostyrev, “Vacancy–solute interactions in ferromagnetic and paramagnetic bcc iron: Ab initio calculations,” *J. Nucl. Mater.*, vol. 419, pp. 248 – 255, 2011.

[55] X.-S. Kong, X. Wu, Y.-W. You, C. Liu, Q. Fang, J.-L. Chen, G.-N. Luo, and Z. Wang, “First-principles calculations of transition metal–solute interactions with point defects in tungsten,” *Acta Mater.*, vol. 66, pp. 172 – 183, 2014.

[56] D. Shin and C. Wolverton, “First-principles study of solute–vacancy binding in magnesium,” *Acta Mater.*, vol. 58, pp. 531–540, 2010.

[57] D. Shin and C. Wolverton, “First-principles density functional calculations for Mg alloys: A tool to aid in alloy development,” *Scripta Mater.*, vol. 63, pp. 680–685, 2010.

[58] J. E. Saal and C. Wolverton, “Solute-vacancy binding of the rare earths in magnesium from first principles,” *Acta Mater.*, vol. 60, pp. 5151–5159, 2012.

[59] Q. Hu, D. Xu, and D. Li, “First-principles investigations of the solute-vacancy interaction energy and its effect on the creep properties of $\alpha$-titanium,” *Philos. Mag. A*, vol. 81, pp. 2809–2821, 2001.

[60] S. S. Naghavi, V. I. Hegde, A. Saboo, and C. Wolverton, “Energetics of cobalt alloys and compounds and solute–vacancy binding in fcc cobalt: A first-principles database,” *Acta Mater.*, vol. 124, pp. 1 – 8, 2017.

[61] J. D. Tucker, “Solute-vacancy interactions in nickel,” *MRS Online Proceedings Library Archive*, vol. 1645, pp. 1–6, 2014.

[62] J. Thijssen, *Computational Physics*. Cambridge University Press, 2 ed., 2007.

[63] C. K. Ande, *First-principles calculations on the stabilization of iron carbides (*$Fe_3C$*,* $Fe_5C_2$ *and* $\eta - Fe_2C$*) in steels*. PhD thesis, Dept. of Materials Science and Engineering, Delft University of Technology, Delft, The Netherlands, 2013.

[64] L. H. Thomas, “The calculation of atomic fields,” *Proc. Cambridge Phil. Roy. Soc.*, vol. 23, p. 542, 1927.

[65] E. Fermi, “un metdo statistic per la determinazione di alcune priorieta dell’ atome,” *Rend. Accad. Naz. Lincei*, vol. 6, p. 602, 1927.

[66] E. Teller, “On the stability of molecules in the thomas-fermi theory,” *Rev. Mod. Phys.*, vol. 34, pp. 627–631, 1962.

[67] P. Hohenberg and W. Kohn, “Inhomogeneous electron gas,” *Phys. Rev.*, vol. 136, pp. B864–B871, 1964.

[68] A. J. Cohen and N. C. Handy, “Assessment of exchange correlation functionals,” *Chemical Physics Letters*, vol. 316, pp. 160 – 166, 2000.

[69] S. F. Sousa, P. A. Fernandes, and M. J. Ramos, “General performance of density functionals,” *The Journal of Physical Chemistry A*, vol. 111, pp. 10439–10452, 2007.

[70] J. Hafner, “Ab-initio simulations of materials using VASP: Density-functional theory and beyond,” *J. Comput. Chem.*, vol. 29, p. 2044, 2008.

[71] J. P. Perdew, K. Burke, and M. Ernzerhof, “Generalized gradient approximation made simple,” *Phys. Rev. Lett.*, vol. 77, pp. 3865–3868, 1996.

[72] C. S. Wang, B. M. Klein, and H. Krakauer, “Theory of magnetic and structural ordering in iron,” *Phys. Rev. Lett.*, vol. 54, pp. 1852–1855, 1985.

[73] T. Asada and K. Terakura, “Cohesive properties of iron obtained by use of the generalized gradient approximation,” *Phys. Rev. B*, vol. 46, pp. 13599–13602, 1992.

[74] T. Asada and K. Terakura, “Erratum: Cohesive properties of iron obtained by use of the generalized gradient approximation,” *Phys. Rev. B*, vol. 48, pp. 17649–17650, 1993.

[75] D. J. Singh, W. E. Pickett, and H. Krakauer, “Gradient-corrected density functionals: Full-potential calculations for iron,” *Phys. Rev. B*, vol. 43, pp. 11628–11634, 1991.

[76] R. Hafner, D. Spišák, R. Lorenz, and J. Hafner, “Magnetic ground state of Cr in density-functional theory,” *Phys. Rev. B*, vol. 65, p. 184432, 2002.

[77] W. Gös, *Hole trapping and the negative bias temperature instability*. PhD thesis, Institute for microelectronics, Vienna university of Technology, 2011.

[78] G. Kresse and J. Furthmüller, “Efficient iterative schemes for ab initio total-energy calculations using a plane-wave basis set,” *Phys. Rev. B*, vol. 54, pp. 11169–11186, 1996.

[79] G. Kresse and D. Joubert, “From ultrasoft pseudopotentials to the projector augmented-wave method,” *Phys. Rev. B*, vol. 59, pp. 1758–1775, 1999.

[80] G. Kresse and J. Hafner, “Ab initio molecular dynamics for liquid metals,” *Phys. Rev. B*, vol. 47, p. 558, 1993.

[81] M. C. Payne, M. P. Teter, D. C. Allan, T. A. Arias, and J. D. Joannopoulos, “Iterative minimization techniques for ab initio total-energy calculations: molecular dynamics and conjugate gradients,” *Rev. Mod. Phys.*, vol. 64, pp. 1045–1097, 1992.

[82] H. J. Monkhorst and J. D. Pack, “Special points for brillouin-zone integrations,” *Phys. Rev. B*, vol. 13, pp. 5188–5192, 1976.

[83] K. W. Böer and U. W. Pohl, *Quantum Mechanics of Electrons in Crystals. In: Semiconductor Physics.*, pp. 1–31. Cham: Springer International Publishing, 2014.

[84] D. R. Hamann, M. Schlüter, and C. Chiang, “Norm-conserving pseudopotentials,” *Phys. Rev. Lett.*, vol. 43, pp. 1494–1497, 1979.

[85] D. Vanderbilt, “Soft self-consistent pseudopotentials in a generalized eigenvalue formalism,” *Phys. Rev. B*, vol. 41, pp. 7892–7895, 1990.

[86] P. E. Blöchl, “Projector augmented-wave method,” *Phys. Rev. B*, vol. 50, pp. 17953–17979, 1994.

[87] J. G. Lee, “Computational materials science: an introduction,” *CRC Press*, 2017.

[88] M. Methfessel and A. T. Paxton, “High-precision sampling for brillouin-zone integration in metals,” *Phys. Rev. B*, vol. 40, pp. 3616–3621, 1989.

[89] I.-S. Kim, J. Hunn, N. Hashimoto, D. Larson, P. Maziasz, K. Miyahara, and E. Lee, “Defect and void evolution in oxide dispersion strengthened ferritic steels under 3.2 MeV Fe+ ion irradiation with simultaneous helium injection,” *J. Nucl. Mater.*, vol. 280, pp. 264 – 274, 2000.

[90] T. Schuler, M. Nastar, and F. Soisson, “Vacancy-induced dissolution of precipitates in out-of-equilibrium systems: A test case of FeX ($x = \mathrm{C}, \mathrm{N}, \mathrm{O}$) alloys,” *Phys. Rev. B*, vol. 95, p. 014113, 2017.

[91] S. Huang, D. L. Worthington, M. Asta, V. Ozolins, G. Ghosh, and P. K. Liaw, "Calculation of impurity diffusivities in $\alpha$-Fe using first-principles methods," *Acta Mater.*, vol. 58, pp. 1982 – 1993, 2010.

[92] O. Gorbatov, A. H. Delandar, Y. N. Gornostyrev, A. Ruban, and P. Korzhavyi, "First-principles study of interactions between substitutional solutes in bcc iron," *J. Nucl. Mater.*, vol. 475, pp. 140 – 148, 2016.

[93] M. Zandbergen, Q. Xu, A. Cerezo, and G. Smith, "Study of precipitation in Al–Mg–Si alloys by atom probe tomography i. microstructural changes as a function of ageing temperature," *Acta Mater.*, vol. 101, pp. 136 – 148, 2015.

[94] W. W. Xu, S. L. Shang, B. C. Zhou, Y. Wang, L. J. Chen, C. P. Wang, X. J. Liu, and Z. K. Liu, "A first-principles study of the diffusion coefficients of alloying elements in dilute $\alpha$-Ti alloys," *Phys. Chem. Chem. Phys.*, vol. 18, pp. 16870–16881, 2016.

[95] M. Werinos, H. Antrekowitsch, T. Ebner, R. Prillhofer, P. Uggowitzer, and S. Pogatscher, "Hardening of Al–Mg–Si alloys: Effect of trace elements and prolonged natural aging," *Materials & Design*, vol. 107, pp. 257 – 268, 2016.

[96] D. J. Hepburn, E. MacLeod, and G. J. Ackland, "Transition metal solute interactions with point defects in fcc iron from first principles," *Phys. Rev. B*, vol. 92, p. 014110, 2015.

[97] C. L. Fu, M. Krčmar, G. S. Painter, and X.-Q. Chen, "Vacancy mechanism of high oxygen solubility and nucleation of stable oxygen-enriched clusters in Fe," *Phys. Rev. Lett.*, vol. 99, p. 225502, 2007.

[98] D. Terentyev, L. Malerba, and A. V. Barashev, "On the correlation between self-interstitial cluster diffusivity and irradiation-induced swelling in Fe–Cr alloys," *Philos. Mag. Lett.*, vol. 85, pp. 587–594, 2005.

[99] E. Vincent, C. Becquart, and C. Domain, "Solute interaction with point defects in $\alpha$-Fe during thermal ageing: A combined ab initio and atomic kinetic monte carlo approach," *J. Nucl. Mater.*, vol. 351, pp. 88 – 99, 2006.

[100] D. Nguyen-Manh, A. P. Horsfield, and S. L. Dudarev, "Self-interstitial atom defects in bcc transition metals: Group-specific trends," *Phys. Rev. B*, vol. 73, p. 020101, 2006.

[101] A. Calder, D. Bacon, A. Barashev, and Y. Osetsky, "On the origin of large interstitial clusters in displacement cascades," *Philos. Mag.*, vol. 90, pp. 863–884, 2010.

[102] C. Becquart and C. Domain, "Modeling microstructure and irradiation effects.," *Metall. Mater. Trans. A*, vol. 42, pp. 852–870, 2011.

[103] L. Dudarev, "Density functional theory models for radiation damage," *Annu. Rev. Mater. Res.*, vol. 43, p. 35, 2013.

[104] Y.-W. You, X.-S. Kong, X.-B. Wu, W. Liu, C. S. Liu, Q. F. Fang, J. L. Chen, G.-N. Luo, and Z. Wang, "Interactions of solute (3p, 4p, 5pand 6p) with solute, vacancy and divacancy in bcc Fe," *J. Nucl. Mater.*, vol. 455, p. 68, 2014.

[105] T. R. Mattsson and A. E. Mattsson, "Calculating the vacancy formation energy in metals: Pt, Pd, and Mo," *Phys. Rev. B*, vol. 66, p. 214110, 2002.

[106] D. E. Jiang and E. A. Carter, "Carbon dissolution and diffusion in ferrite and austenite from first principles," *Phys. Rev. B*, vol. 67, p. 214103, 2003.

[107] G. Rahman, I. G. Kim, H. K. D. H. Bhadeshia, and A. J. Freeman, "First-principles investigation of magnetism and electronic structures of substitutional 3d transition-metal impurities in bcc Fe," *Phys. Rev. B*, vol. 81, p. 184423, 2010.

[108] W. Xie, W. Xiong, C. A. Marianetti, and D. Morgan, "Correlation and relativistic effects in U metal and U − Zr alloy: Validation of ab initio approaches," *Phys. Rev. B*, vol. 88, p. 235128, 2013.

[109] D. R. Olander, "Fundamental aspects of nuclear reactor fuel elements: solutions to problems," tech. rep., California Univ., Berkeley (USA). Dept. of Nuclear Engineering, 1976.

[110] K. Hack, *The SGTE casebook: thermodynamics at work*. Elsevier, 2008.

[111] M. Neubauer, K. P. Lieb, P. Schaaf, and M. Uhrmacher, "Ion-beam mixing of Ag/Fe and In/Fe layers studied by hyperfine techniques," *Phys. Rev. B*, vol. 53, pp. 10237–10243, 1996.

[112] S. Amirthapandian, B. K. Panigrahi, S. Rajagopalan, A. Gupta, K. G. M. Nair, A. K. Tyagi, and A. Narayanasamy, "Evidence for complete ion-beam mixing in thermally immiscible Fe/Ag multilayers from conversion electron mössbauer spectroscopy," *Phys. Rev. B*, vol. 69, p. 165411, 2004.

[113] B. Rauschenbach, A. Kolitsch, and K. Hohmuth, "Iron nitride phases formed by nitrogen ion implantation and thermal treatment," *physica status solidi (a)*, vol. 80, pp. 471–482, 1983.

[114] A. Kehrel†, J. Keinonen, P. Haussalo, K. P. Lieb, and M. Uhrmacher, "Hydrogen trapping at radiation defects in sodium-implanted iron, nickel and molybdenum," *Radiat. Eff. Defect S*, vol. 118, pp. 297–307, 1991.

[115] W. Counts, C. Wolverton, and R. Gibala, "First-principles energetics of hydrogen traps in $\alpha$-Fe: Point defects," *Acta Mater.*, vol. 58, pp. 4730 – 4741, 2010.

[116] D. H. R. Fors and G. Wahnström, "Nature of boron solution and diffusion in $\alpha$-iron," *Phys. Rev. B*, vol. 77, p. 132102, 2008.

[117] C. Domain, C. S. Becquart, and J. Foct, "Ab initio study of foreign interstitial atom (C, N) interactions with intrinsic point defects in $\alpha$-Fe," *Phys. Rev. B*, vol. 69, p. 144112, 2004.

[118] A. F. Bialon, T. Hammerschmidt, and R. Drautz, "Ab initio study of boron in $\alpha$-iron: Migration barriers and interaction with point defects," *Phys. Rev. B*, vol. 87, p. 104109, 2013.

[119] C. Barouh, T. Schuler, C.-C. Fu, and M. Nastar, "Interaction between vacancies and interstitial solutes (C, N, and O) in $\alpha-$Fe: From electronic structure to thermodynamics," *Phys. Rev. B*, vol. 90, p. 054112, 2014.

[120] M. Souissi, Y. Chen, M. H. Sluiter, and H. Numakura, “Ab initio characterization of $B, C, N, and O$ in bcc iron: Solution and migration energies and elastic strain fields,” *Comp. Mater. Sci.*, vol. 124, pp. 249 – 258, 2016.

[121] C. Ravi, C. Wolverton, and V. Ozoliņš, “Predicting metastable phase boundaries in Al-Cu alloys from first-principles calculations of free energies: The role of atomic vibrations,” *Europhysics Letters (EPL)*, vol. 73, pp. 719–725, 2006.

[122] P. Villars, H. Okamoto, and K. Cenzual, “Asm alloy phase diagrams database,” *http://www.asminternational.org*, (ASM International, Materi- als Park, OH, 2016).

[123] P. Villars and L. D. Calvert *Pearson’s Hand of Crys- tallographic Data for Intermetallic Phases*, 2nd ed. (ASM International, Materials Park, OH, 1991).

[124] P. Villars, “Inorganic solid phases, SpringerMaterials (online database),” 2016.

[125] J. Sánchez, J. Fullea, C. Andrade, and P. De Andres, “Hydrogen in $\alpha$-iron: Stress and diffusion,” *Phys. Rev. B*, vol. 78, p. 014113, 2008.

[126] D. Murali, M. Posselt, and M. Schiwarth, “First-principles calculation of defect free energies: General aspects illustrated in the case of bcc Fe,” *Phys. Rev. B*, vol. 92, p. 064103, 2015.

[127] C. Kittel, P. McEuen, and P. McEuen, *Introduction to solid state physics*. Wiley New York, 1996.

[128] P. Söderlind, L. H. Yang, J. A. Moriarty, and J. M. Wills, “First-principles formation energies of monovacancies in bcc transition metals,” *Phys. Rev. B*, vol. 61, pp. 2579–2586, 2000.

[129] L. De Schepper, D. Segers, L. Dorikens-Vanpraet, M. Dorikens, G. Knuyt, L. M. Stals, and P. Moser, “Positron annihilation on pure and carbon-doped $\alpha$-iron in thermal equilibrium,” *Phys. Rev. B*, vol. 27, pp. 5257–5269, 1983.

[130] S. Grindy, B. Meredig, S. Kirklin, J. E. Saal, and C. Wolverton, “Approaching chemical accuracy with density functional calculations: Diatomic energy corrections,” *Phys. Rev. B*, vol. 87, p. 075150, 2013.

[131] W. L. Roth, “Magnetic structures of $MnO, FeO, CoO, and NiO$,” *Phys. Rev.*, vol. 110, pp. 1333–1341, 1958.

[132] D. S. Parker, “Strong 3D and 1D magnetism in hexagonal fe-chalcogenides FeS and FeSe vs. weak magnetism in hexagonal FeTe,” *Sci. Rep.*, vol. 7, pp. 1–6, 2017.

[133] P. J. Brown, J. Deportes, and B. Ouladdiaf, “Magnetic structure of the laves phase compound $TiFe_2$,” *J. Phys. Condens. Matter*, vol. 4, pp. 10015–10024, 1992.

[134] H. Katsuraki and K. Suzuki, “Magnetic structure of $Fe_2As$,” *J. Appl. Phys.*, vol. 36, pp. 1094–1095, 1965.

[135] A. Subedi and D. J. Singh, “Band structure and itinerant magnetism in quantum critical $NbFe_2$,” *Phys. Rev. B*, vol. 81, p. 024422, 2010.

[136] L. Häggström, T. Ericsson, R. Wäppling, and K. Chandra, "Studies of the magnetic structure of FeSn using the mössbauer effect," *Phys. Scr.*, vol. 11, pp. 47–54, 1975.

[137] T. Yashiro, Y. Yamaguchi, S. Tomiyoshi, N. Kazama, and H. Watanabe, "Magnetic structure of Fe1+ $\delta$ Sb," *J. Phys. Soc. Jpn.*, vol. 34, pp. 58–62, 1973.

[138] D. Cherian, S. Rößler, C. Koz, A. Tsirlin, U. Schwarz, S. Wirth, and S. Elizabeth, "Structural and thermodynamic properties of $\mathrm{Fe}_{1.12}\mathrm{Te}$ with multiple phase transitions," *J. Appl. Phys.*, vol. 115, p. 123912, 2014.

[139] P. Bödeker, A. Schreyer, Zabel, and H., "Spin-density waves and reorientation effects in thin epitaxial Cr films covered with ferromagnetic and paramagnetic layers," *Phys. Rev. B*, vol. 59, pp. 9408–9431, 1999.

[140] M. A. McGuire, "Crystal and magnetic structures in layered, transition metal dihalides and trihalides," *Crystals*, vol. 7, p. 121, 2017.

[141] E. Hayward and C.-C. Fu, "Interplay between hydrogen and vacancies in $\alpha$-fe," *Phys. Rev. B*, vol. 87, p. 174103, 2013.

[142] C.-C. Fu and F. Willaime, "Ab initio study of helium in $\alpha$—Fe: Dissolution, migration, and clustering with vacancies," *Phys. Rev. B*, vol. 72, p. 064117, 2005.

[143] Y. You, M. Yan, and H. Chen, "Interactions of carbon–nitrogen and carbon–nitrogen–vacancy in $\alpha$-fe from first-principles calculations," *Comp. Mater. Sci.*, vol. 67, pp. 222 – 228, 2013.

[144] P. Zhang, J. Ding, D. Sun, and J. Zhao, "First-principles study of noble gas atoms in bcc fe," *J. Nucl. Mater.*, vol. 492, pp. 134 – 141, 2017.

[145] R. A. Pérez and M. Weissmann, "Ab initio study of magnetic effects on diffusion in $\alpha$-fe," *J. Phys. Condens. Matter*, vol. 16, pp. 7033–7043, 2004.

[146] X. Gai, R. Smith, and S. Kenny, "Inert gas bubbles in bcc fe," *J. Nucl. Mater.*, vol. 470, pp. 84 – 89, 2016.

[147] J. P. Hirth, "Effects of hydrogen on the properties of iron and steel," *Metall. Trans. A*, vol. 11, pp. 861–890, 1980.

[148] L. Ventelon, B. Wirth, and C. Domain, "Helium–self-interstitial atom interaction in $\alpha$-iron," *J. Nucl. Mater.*, vol. 351, pp. 119 – 132, 2006.

[149] A. Jacob, E. Povoden-Karadeniz, and E. Kozeschnik, "Revised thermodynamic description of the Fe-Cr system based on an improved sublattice model of the $\sigma$ phase," *Calphad*, vol. 60, pp. 16 – 28, 2018.

[150] O. Kubaschewski, "Iron-binary phase diagrams," *(Springer-Verlag, Berlin, Heidelberg, 1982)*, 1982.

[151] H. W. King, "Quantitative size-factors for metallic solid solutions," *J. Mater. Sci.*, vol. 1, p. 79, 1966.

[152] B. Drittler, N. Stefanou, S. Blügel, R. Zeller, and P. H. Dederichs, "Electronic structure and magnetic properties of dilute fe alloys with transition-metal impurities," *Phys. Rev. B*, vol. 40, pp. 8203–8212, 1989.

[153] C. Liu, M. Asato, N. Fujima, and T. Hoshino, “Full-potential kkr calculations for point defect energies in Fe-based dilute alloys, based on the generalized-gradient approximation,” *Mater. Trans.*, vol. 54, pp. 1667–1672, 2013.

[154] W. Counts, C. Wolverton, and R. Gibala, “Binding of multiple H atoms to solute atoms in bcc fe using first principles,” *Acta Mater.*, vol. 59, pp. 5812 – 5820, 2011.

[155] H. K. D. H. Bhadeshia, “Carbon–carbon interactions in iron,” *J. Mater. Sci.*, vol. 39, p. 3949, 2004.

[156] C. W. Sinclair, M. Perez, R. G. A. Veiga, and A. Weck, “Molecular dynamics study of the ordering of carbon in highly supersaturated $\alpha$-Fe,” *Phys. Rev. B*, vol. 81, p. 224204, 2010.

[157] X. Gai, T. Lazauskas, R. Smith, and S. D. Kenny, “Helium bubbles in bcc Fe and their interactions with irradiation,” *J. Nucl. Mater.*, vol. 462, pp. 382 – 390, 2015.

[158] L. Messina, M. Nastar, T. Garnier, C. Domain, and P. Olsson, “Exact ab initio transport coefficients in bcc $Fe - x$ ($x =$ Cr, Cu, Mn, Ni, p, Si) dilute alloys,” *Phys. Rev. B*, vol. 90, p. 104203, 2014.

[159] L. Messina, M. Nastar, N. Sandberg, and P. Olsson, “Systematic electronic-structure investigation of substitutional impurity diffusion and flux coupling in bcc iron,” *Phys. Rev. B*, vol. 93, p. 184302, 2016.

[160] G. E. Murch, “Phase transformations in materials,” *edited by G. Kostorz*, (Wiley-VCH Verlag GmbH, Weinheim, 2001).

[161] S. Shang, H. Fang, J. Wang, C. Guo, Y. Wang, P. Jablonski, Y. Du, and Z. Liu, “Vacancy mechanism of oxygen diffusivity in bcc Fe: A first-principles study,” *Corros. Sci.*, vol. 83, pp. 94 – 102, 2014.

[162] G. Odette, B. Wirth, D. Bacon, and N. Ghoniem, “Multiscale-multiphysics modeling of radiation-damaged materials: Embrittlement of pressure-vessel steels,” *MRS Bulletin*, vol. 26, p. 176–181, 2001.

[163] R. Arndt and A. Damask, “Kinetics of carbon precipitation in irradiated iron—iii. calorimetry,” *Acta Metallurgica*, vol. 12, pp. 341 – 345, 1964.

[164] A. Möslang, E. Albert, E. Recknagel, A. Weidinger, and P. Moser, “Interaction of vacancies with impurities in iron,” *Hyperfine Interact.*, vol. 15, pp. 409–412, 1983.

[165] M. Doyama, “Study of metallic properties by positive muons,” *Bull. Jpn. Inst. Met.*, vol. 25, p. 808, 1986.

[166] R. Idczak, R.and Konieczny and J. Chojcan, “A study of defects in iron-based binary alloys by the mössbauer and positron annihilation spectroscopies,” *J. Appl. Phys.*, vol. 115, p. 103513, 2014.

[167] J.-L. Bocquet, C. Barouh, and C.-C. Fu, “Migration mechanism for oversized solutes in cubic lattices: The case of yttrium in iron,” *Phys. Rev. B*, vol. 95, p. 214108, 2017.

[168] H. King, “Quantitative size-factors for interstitial solid solutions,” *J. Mater. Sci.*, vol. 6, pp. 1157–1167, 1971.

[169] M. C. Brandes, L. Kovarik, M. K. Miller, and M. Mills, “Morphology, structure, and chemistry of nanoclusters in a mechanically alloyed nanostructured ferritic steel,” *J. Mater. Sci.*, vol. 47, p. 103513, 2012.

[170] P. Erhart, “A first-principles study of helium storage in oxides and at oxide–iron interfaces,” *J. Appl. Phys.*, vol. 111, p. 113502, 2012.

[171] I. Monnet, T. Van den Berghe, and P. Dubuisson, “A comparison between different oxide dispersion strengthened ferritic steel ongoing in situ oxide dissolution in high voltage electron microscope,” *J. Nucl. Mater.*, vol. 424, pp. 204 – 209, 2012.

[172] J. Hoffmann, M. Rieth, R. Lindau, M. Klimenkov, A. Möslang, and H. R. Z. Sandim, “Investigation on different oxides as candidates for nano-sized ODS particles in reduced-activation ferritic (RAF) steels,” *J. Nucl. Mater.*, vol. 442, pp. 444 – 448, 2013.

[173] C. Ravi, “Thermodynamic stability of oxide phases of $Fe-Cr$ based ODS steels via quantum mechanical calculations,” *Calphad*, vol. 45, pp. 188 – 193, 2014.

[174] J. Ribis, E. Bordas, P. Trocellier, Y. Serruys, Y. de Carlan, and A. Legris, “Comparison of the neutron and ion irradiation response of nano-oxides in oxide dispersion strengthened materials,” *J. Mater. Res.*, vol. 30, p. 2210–2221, 2015.

[175] C. Lu, Z. Lu, X. Wang, R. Xie, Z. Li, M. Higgins, C. Liu, F. Gao, and L. Wang, “Enhanced radiation-tolerant oxide dispersion strengthened steel and its microstructure evolution under helium-implantation and heavy-ion irradiation,” *Sci. Rep.*, vol. 7, p. 40343, 2017.

[176] P. Dou, S. Jiang, L. Qiu, and A. Kimura, “Effects of contents of Al, Zr and Ti on oxide particles in Fe–15Cr–2W–0.35$Y_2O_3$ODS steels,” *J. Nucl. Mater.*, vol. 531, p. 152025, 2020.

[177] K. Takahashi and Y. Tanaka, “Role of descriptors in predicting the dissolution energy of embedded oxides and the bulk modulus of oxide-embedded iron,” *Phys. Rev. B*, vol. 95, p. 014101, 2017.

[178] J.-L. Boutard, V. Badjeck, L. Barguet, C. Barouh, A. Bhattacharya, Y. Colignon, C. Hatzoglou, M. Loyer-Prost, A. Rouffié, N. Sallez, H. Salmon-Legagneur, and T. Schuler, “Oxide dispersion strengthened ferritic steels: a basic research joint program in france,” *J. Nucl. Mater.*, vol. 455, pp. 605 – 611, 2014.

[179] F. Siska, L. Stratil, H. Hadraba, S. Fintova, I. Kubena, V. Hornik, R. Husak, D. Bartkova, and T. Zalezak, “Strengthening mechanisms of different oxide particles in 9Cr ODS steel at high temperatures,” *Mater. Sci. Eng. A*, vol. 732, pp. 112 – 119, 2018.

[180] N. H. Oono, S. Ukai, K. Tominaga, N. Ebisawa, and K. Tomura, “Precipitation of various oxides in ODS ferritic steels,” *J. Mater. Sci.*, vol. 54, p. 8786–8799, 2019.

[181] K. Kaminaga, R. Sei, K. Hayashi, N. Happo, H. Tajiri, D. Oka, T. Fukumura, and T. Hasegawa, "A divalent rare earth oxide semiconductor: Yttrium monoxide," *Appl. Phys. Lett.*, vol. 108, pp. 122102–122104, 2016.

[182] R. J. Nicholls, N. Ni, A. London, D. W. McComb, P. D. Nellist, C. R. M. Grovenor, C. J. Pickard, and J. R. Yates, "Crystal structure of the ZrO phase at Zirconium/Zirconium oxide interfaces," *Adv. Eng. Mater.*, vol. 17, p. 211, 2015.

[183] E. Akshaya Devi, C. Ravi, and C. S. Sundar, "First-principles study of interaction energies of atomic defects in bcc ferromagnetic iron," *Phys. Rev. B*, vol. 98, p. 144104, 2018.

[184] P. Vinet, J. H. Rose, J. Ferrante, and J. R. Smith, "Universal features of the equation of state of solids," *J. Phys. Condens. Matter*, vol. 1, pp. 1941–1963, 1989.

[185] P. Janthon, S. A. Luo, S. M. Kozlov, F. Viñes, J. Limtrakul, D. G. Truhlar, and F. Illas, "Bulk properties of transition metals: A challenge for the design of universal density functionals," *J. Chem. Theory Comput.*, vol. 10, pp. 3832–3839, 2014.

[186] G. L. Rech, J. E. Zorzi, and C. A. Perottoni, "Equation of state of hexagonal-close-packed rhenium in the terapascal regime," *Phys. Rev. B*, vol. 100, p. 174107, 2019.

[187] A. Hirata, T. Fujita, C. Liu, and M. Chen, "Characterization of oxide nanoprecipitates in an oxide dispersion strengthened 14YWT steel using aberration-corrected STEM," *Acta Mater.*, vol. 60, pp. 5686 – 5696, 2012.

[188] J. Brodrick, D. Hepburn, and G. Ackland, "Mechanism for radiation damage resistance in yttrium oxide dispersion strengthened steels," *J. Nucl. Mater.*, vol. 445, pp. 291 – 297, 2014.

[189] M.J.Winter, "Webelements database. http://www.webelement.com/. The atomic radius given here are calculated values using methods outlined in E.Clementi, D.I.Raimondi, W.P.Reinhardt," *J. Chem. Phys.*, vol. 38, p. 2686, 1963.

[190] T. Koseki, H. Kato, M. Tsutsumi, K. Kasai, and I. J, "Ferrite transformation from oxide–steel interface in HAZ-simulated C–Mn steel," *Int. J. Mater. Res.*, vol. 99, pp. 347–351, 2008.

[191] N. W. Ashcroft and N. D. Mermin, "*Solid State Physics*," CENGAGE *learning Indian edition*, 2003.

[192] A. Furmanchuk, A. Agrawal, and A. Choudhary, "Predictive analytics for crystalline materials: bulk modulus," *RSC Adv.*, vol. 6, pp. 95246–95251, 2016.

[193] K. Kunc and K. Syassen, "P(V) equations of state of solids: Density functional theory calculations and LDA versus GGA scaling," *Phys. Rev. B*, vol. 81, p. 134102, 2010.

[194] H. L. Zhang, S. Lu, M. P. J. Punkkinen, Q.-M. Hu, B. Johansson, and L. Vitos, "Static equation of state of bcc iron," *Phys. Rev. B*, vol. 82, p. 132409, 2010.

[195] H. Zhang, M. P. J. Punkkinen, B. Johansson, S. Hertzman, and L. Vitos, "Single-crystal elastic constants of ferromagnetic bcc Fe-based random alloys from first-principles theory," *Phys. Rev. B*, vol. 81, p. 184105, 2010.

[196] M. S. El-Genk and J.-M. Tournier, "A review of refractory metal alloys and mechanically alloyed-oxide dispersion strengthened steels for space nuclear power systems," *J. Nucl. Mater.*, vol. 340, pp. 93 – 112, 2005.

[197] M. Auger, Y. Huang, H. Zhang, C. Jones, Z. Hong, M. Moody, S. Roberts, and P. Grant, "Microstructural and mechanical characterisation of $\mathrm{Fe}-14\mathrm{Cr}-0.22\mathrm{Hf}$ alloy fabricated by spark plasma sintering," *J. Alloy. Compd.*, vol. 762, pp. 678 – 687, 2018.